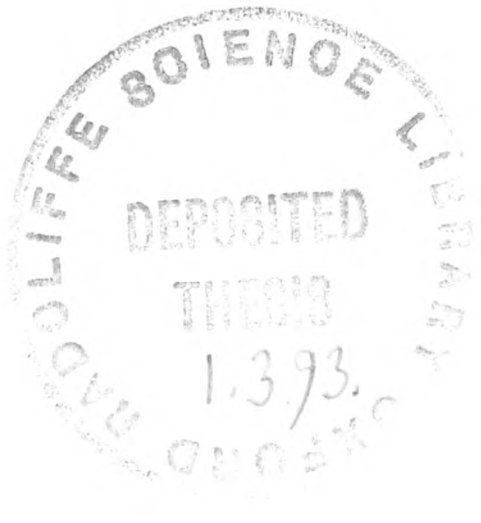
A comparison of the 1S–2S and 2S–4P frequencies in atomic hydrogen.

Carol Denise Thompson

University College

Submitted for the Degree of Doctor of Philosophy
Trinity Term 1992



Abstract

A comparison of the 1S–2S and 2S–4P frequencies in atomic hydrogen.

Carol Denise Thompson
University College

Submitted for the Degree of Doctor of Philosophy
Trinity Term 1992

An experiment has been carried out to compare directly the frequencies of the $1S_{1/2}$-$2S_{1/2}$ and $2S_{1/2}$-$4P_{1/2}$ transitions in atomic hydrogen and hence obtain a value for the $1S_{1/2}$ Lamb shift. It is the first of a new generation of $1S_{1/2}$ Lamb shift experiments which are much less dependent on external frequency standards than earlier work [1, 2] because no absolute measurement of the $1S_{1/2}$-$2S_{1/2}$ frequency is required. This pilot experiment gave a result of 8167(10) MHz for the $1S_{1/2}$ Lamb shift.

The $1S_{1/2}$-$2S_{1/2}$ transition was excited by two-photon Doppler-free spectroscopy. The necessary radiation at 243 nm was generated by intra-cavity frequency doubling with a crystal of β-barium borate (BBO) placed inside a ring dye laser operating at 486 nm. For the first time, the $1S_{1/2}$-$2S_{1/2}$ transition was excited in an atomic beam, thereby removing the uncertainties inherent in cell experiments and generating an optically-excited beam of metastable ($2S_{1/2}$) hydrogen atoms.

The single-photon $2S_{1/2}$-$4P_{1/2}$ transition was excited by radiation at 486 nm from a second ring dye laser, incident transversely on the optically excited metastable beam. The small frequency difference ($\sim$ 4.7 GHz) between the fundamental output of the doubled laser and that of the second laser when both were on resonance was directly measured using a stabilised optical cavity.

From this measured frequency interval, the value quoted above for the $1S_{1/2}$ Lamb shift was obtained. The result is in agreement with theory and is considerably more precise than that obtained from earlier direct comparisons of $1S_{1/2}$-$2S_{1/2}$ and Balmer-β [3]. The error on the result was largely due to the limited amount of data available. However, the aim of the experiment was to demonstrate the feasibility of the method. This has been achieved and considerable improvements in precision should be possible in the future.

Acknowledgements

First of all, I would like to thank my supervisor, Dr. D.N. Stacey, for the excellent supervision and encouragement which I have received during my time on this project. The experience has been most rewarding—but I will not go so far as to say that I would like to do it *all* over again! Dr. C.J. Foot has also played a very important role in the experiment, and has provided me with much help and advice for which I am grateful. My thanks also go to the following: Dr. G.K. Woodgate for much advice, encouragement and useful little nuggets of information, Dr. P.E.G. Baird for first introducing me to atomic physics and Prof. P.G.H. Sandars for his interest in the progress of the work.

Deserving of very special mention is Dr. P. Hannaford (from CSIRO in Melbourne), who spent two periods working with us in the basement. His contribution to the experiment was (and still is) greatly appreciated—especially by those of us who were on the receiving end of the slave-driving! I must emphasise though that he led by example, and was even known to help with a dye change—a thing normally unheard of in a Big Cheese.

Of the somewhat lesser cheeses, first and foremost is Mr. G.H. Woodman—my fellow slave on the experiment. I would like to say how much I appreciated his good humour and enthusiasm. I could not have asked for a better lab-mate (even allowing for the 'phone calls).

It is a pleasure to acknowledge the excellent technical support staff of the Clarendon Laboratory. I will start with Mr. C.W. Goodwin, who supplied expert technical support to the basement during the early stages of the experiment and many excellent optical coatings throughout its duration. The role of basement technician was taken on later by Mr. G.R.K. Quelch, to whom very special thanks are due for all kinds of things, including precision machining jobs, countless bits of technical wizardry, introducing a coffee maker into the basement and taking the photographs included in this thesis (and I should point out that the original slides were *perfectly* sharp). Many thanks also to Mr. G. Matthews of the Research Workshop for guiding me through the rudiments of machine-shop work and generally "being George", Mr. S. Giles for supplying us with discharge tubes, Mr. T. Hastings for repairing the Heathkit, Mr. T. Holliday and the staff of the Clarendon Main Workshop for many important machining jobs and building maintenance for moving our furniture around from time to time. I would also like to acknowledge the help of the Cryogenic Facilities Group–Mr. J. Cosier for designing the cryopump and teaching us about the mysteries of liquid helium, Mr. R. Thomson for dealing with our dewar and Mr. R. Silvester for saving the experiment from certain doom during the incident with the bladder. Before leaving the subject of technical support, mention should be made of the very important

part played by T.P. Marvin in this experiment.

Now for the rest of "the group", which in recent years really has got too big for me to be able to mention everyone by name. However, I hope that anyone I've ever talked to at coffee-time will consider themselves duly thanked for something or other. I must single out a few for special mention however. Because of our acquaintance which stretches back into the mists of time, I will start by thanking Dr. K.P. Zetie for putting up with *me* for so long (and for teaching me LaTeX). Thanks also to Mr. R.B. Warrington for filling in the gaps in my LaTeX "knowledge" and helping me out of numerous computer-related pickles, Mr. E. Stephens for arranging two excellent days out during the writing of this thesis, Dr. M.J.D. Macpherson for advice on all kinds of experimental things and Dr. T.D. Wolfenden for giving me my earliest introduction to the dark art of dye laser tweeking. Special mention must go to Miss J.E.M. James for many "useful discussions" on physics (and physicists), as well as knitting and other feminine topics.

My thanks go to Professor Cowley for allowing me to use the facilities of the Clarendon Laboratory and all the rest of the staff (Stores, Accounts, secretarial staff and tea-ladies) for their various contributions. I was supported during my research by a postgraduate award from the Department of Education in Northern Ireland. I have spent six years as a member of University College and I thank everyone there for making it such an enjoyable experience. I would also like to express my gratitude to the Principal and Fellows of Somerville College for appointing me to the Mary Somerville Research Fellowship and for their kind interest in the progress of this thesis.

I take great pleasure in acknowledging the support of my ex-housemates—Shelagh, Simon and Mark—who kept me well fed and the bath clean and were always ready to listen to my tales of woe. I take this opportunity of assuring them that the experiment eventually did go "foom".

Very special thanks are due to Nigel, who has always been (apparently) genuinely interested in all my doings, and who has been a great source of support during my research. He has also become official cartoonist to the basement and has brightened up many a talk and conference presentation.

I will finish with the most important people of all–my family. They have always been behind me in everything I have done, now as much as ever. Their love and support has made all of this worthwhile.

Contents

1 Introduction **1**
- 1.1 Background . . . 1
- 1.2 The 1S Lamb shift . . . 2
- 1.3 The 1S–2S transition . . . 2
- 1.4 Previous work on the 1S–2S transition . . . 3
  - 1.4.1 Pulsed experiments . . . 3
  - 1.4.2 Continuous-wave experiments . . . 4
- 1.5 The present experiment . . . 6
- 1.6 The layout of this thesis . . . 7

2 Theory of hydrogenic atoms **8**
- 2.1 Introduction . . . 8
- 2.2 The energy levels of hydrogenic atoms . . . 8
  - 2.2.1 Non-QED contributions . . . 8
  - 2.2.2 QED corrections . . . 9
  - 2.2.3 Finite nuclear size correction . . . 11
- 2.3 Uncertainties in the 1S Lamb shift . . . 11
- 2.4 Hyperfine structure . . . 13
- 2.5 Calculation of frequency intervals . . . 13

3 Feasibility study for the 1S–2S excitation **17**
- 3.1 The two-photon excitation rate . . . 17
- 3.2 Finite transit time . . . 19
- 3.3 The effect of collisions . . . 20
- 3.4 Selection rules . . . 20
- 3.5 The geometry of the experiment . . . 21
- 3.6 The expected size of the two-photon signal . . . 23
- 3.7 The experimental conditions . . . 26
  - 3.7.1 Laser power and enhancement cavity. . . . 26
  - 3.7.2 The hydrogen source. . . . 27
  - 3.7.3 The detection region. . . . 28
  - 3.7.4 The beam chamber. . . . 28
  - 3.7.5 The expected signal rate . . . 29

4 The UV enhancement cavity **32**
4.1 Introduction 32
4.2 Enhancement factor and mirror reflectivities 33
4.3 Mode structure and cavity geometry 36
4.4 Mode-matching the UV beam 37
4.5 Reduction of the UV background 38
4.6 Mirror holders 38
4.7 The servo system 38
4.8 The 30 cm brass cavity 42
4.9 The 40 cm Dural cavity 48
4.10 Summary 55

5 The hydrogen beam and 1S–2S excitation **57**
5.1 Introduction 57
5.2 The vacuum system 58
5.3 The atomic hydrogen source 60
5.3.1 Dissociation of molecular hydrogen 63
5.3.2 Transport of atomic hydrogen 64
5.3.3 Running conditions 69
5.4 The 1S–2S interaction region 69
5.5 The detection system 70
5.6 The frequency doubled laser 73
5.7 The wavemeter 75
5.8 The locking and scanning system 77
5.9 Locating and scanning the 1S–2S resonance 79
5.10 The metastable beam 81

6 The Balmer-β excitation **83**
6.1 Introduction 83
6.2 Residual Doppler width and collimation 83
6.3 Estimate of the 2S–4P signal 84
6.3.1 The transition probability 84
6.3.2 Application to this experiment 87
6.4 The Balmer-β laser 89
6.5 The light path to the metastable beam 90
6.6 The wavemeter readings for the Balmer-β excitation 92
6.7 The 1 metre reference cavity 93
6.8 Determination of the frequency difference δ 95
6.9 The control program 95
6.10 Summary 98

7 Results and analysis **100**
7.1 Introduction 100
7.2 2S–4P and reference fringes 101
7.2.1 Linearisation of the frequency scale 105
7.2.2 Fitting the 2S–4P data 108
7.3 1S–2S and reference fringe 113
7.4 Cavity drift 117
7.5 The frequency interval δ 120
7.6 Calculation of the 1S Lamb shift 120
7.7 Systematic effects 121
7.7.1 Second order Doppler shift 121
7.7.2 The Zeeman effect 121
7.7.3 The DC Stark effect 122
7.7.4 The AC Stark effect 123
7.7.5 The retro-reflected 486 nm beam 123

8 Conclusions **125**
8.1 Summary of this work 125
8.2 The optically excited metastable beam 125
8.3 Future prospects for the 1S Lamb shift 126

List of Figures

2.1 Hyperfine splittings. 14

3.1 The transitions involved in this experiment. 22
3.2 The hydrogen nozzle and 1S–2S interaction region. 24
3.3 Plan view of the atomic beam chamber. 25

4.1 Enhancement factor as a function of input mirror transmission. . . . 35
4.2 Mirror holder used with the ASM20 piezo controlled mirror mount. . 39
4.3 Mirror holder with brass tilt screws. 40
4.4 The servo electronics. 41
4.5 The 30 cm brass cavity. 43
4.6 Predicted mode structure of the 30 cm cavity. 44
4.7 Mode matching layout for the 30 cm cavity. 45
4.8 The mode structure of the 30 cm cavity. 46
4.9 Enhancement degradation as a function of time. 47
4.10 The 40 cm Dural cavity. 50
4.11 The undamaged section of the Acton 30 cm medium reflector. 51
4.12 The predicted mode structure of the 40 cm cavity. 51
4.13 The mode matching layout for the 40 cm cavity. 52
4.14 Mode matching layout for the 40 cm cavity with modified UV beam. 52
4.15 Tubular baffle. 54

5.1 The 1S–2S excitation—schematic. 58
5.2 The vacuum system. 59
5.3 The cryopump. 61
5.4 The atomic hydrogen source. 62
5.5 The constriction in the Pyrex discharge tube. 64
5.6 The PTFE tube entering the vacuum can. 68
5.7 The photomultiplier housing and extension. 71
5.8 The quench wires. 72
5.9 The new BBO crystal mount (schematic). 74
5.10 The wavemeter. 76
5.11 The stabilisation scheme for the reference HeNe. 76
5.12 The Hänsch-Couillaud locking and AOM scanning system. 78

5.13 The method of scanning the laser using the AOM. 80
5.14 The optically excited metastable beam. 81

6.1 The relevant hydrogen energy levels for the Balmer-β excitation. . . . 84
6.2 The illuminated region of the metastable beam. 88
6.3 The output of the Balmer-β laser. 89
6.4 The use of the gunsight. 90
6.5 The optical layout for the reference cavity and wavemeter. 94
6.6 The experimental determination of δ. 96

7.1 Summary of the analysis of the quench data. 102
7.2 Summary of the analysis of the 1S–2S signal and reference fringe data. 103
7.3 The raw quench data from the file *july2f1*.qch. 106
7.4 The "e" quench data, fitted using TWOFIT. 110
7.5 The "f" quench data, fitted using TWOFIT. 111
7.6 The 1S–2S signal data *july2f1*.sig, fitted using SIGFIT. 116
7.7 Reference fringe data *july2f1*.ref, fitted using REFRINGE. 118

List of Tables

2.1 The published values of $G_{SE}(Z\alpha)$. 10
2.2 The contributions to the hydrogen 1S Lamb shift. 12
2.3 The uncertainty in the calculated 1S Lamb shift. 12
2.4 Hyperfine splittings. 13
2.5 Energies of the $1S_{1/2}$, $2S_{1/2}$ and $4S_{1/2}$ levels. 15
2.6 Calculation of δ for the comparison transition $2S_{1/2}$–$4P_{1/2}$. 16
2.7 Calculation of δ for the comparison transition $2S_{1/2}$–$4P_{3/2}$. 16

3.1 Experimental conditions used in the 1S–2S signal estimate. 30
3.2 Estimated signal rate S for various beam conditions. 31

5.1 Hydrogen transport efficiency. 66

6.1 Transition probability for the hyperfine components of 2S–4P. 87
6.2 Wavemeter readings for the two components of 2S–4P. 93

7.1 The format of the raw data file *july2f1*.qch. 104
7.2 Fringe heights and positions used in the program FRINGEFIT. . . . 108
7.3 Results of fitting the "f" quench data with two Lorentzians. 109
7.4 Results of fitting the "f" quench data with a single Lorentzians. . . . 112
7.5 Values of b—uncorrected for cavity drift. 112
7.6 The format of the raw data file *july2f1*.sig. 113
7.7 The format of the raw data file *july2f1*.ref. 114
7.8 Results of fitting the 1S–2S data *july2f1*.sig using SIGFIT. 115
7.9 Results of fitting the 1S–2S and reference fringe data. 117
7.10 Values of a corrected for cavity drift. 119
7.11 Values of b corrected for cavity drift. 119
7.12 The calculation of δ from the data. 120

List of Plates

I The 40 cm Dural cavity. 56
II The gunsight. 91
III An overview of the experimental apparatus. 99

"...but to be at so much trouble in filling great volumes, which, as I used to think, nobody would willingly ever look into,.....always struck me as a hard fate; and though I know it is all very right and necessary, I have often wondered at the person's courage that could sit down on purpose to do it."

Jane Austen

To my parents

Chapter 1

Introduction

1.1 Background

The hydrogen atom is the simplest stable atomic system and has therefore always played an important role in the history of atomic physics. From Balmer's empirical formula for the lines of the hydrogen spectrum in 1885 and Rydberg's work on wavenumbers and term values in 1889 to Bohr's theory of the atom (1913), the new quantum theory of Schrödinger and Heisenberg (1925/6) and Dirac's relativistic quantum theory of 1928, many developments in fundamental physics are somehow connected to studies of the hydrogen spectrum. (An account of the history of the spectroscopy of atomic hydrogen can be found in references [4] and [5]).

One such development arose from the famous radio-frequency measurements of Lamb and Retherford in 1947 [6]. This work was done to resolve a question raised by experiments on the hydrogen spectrum in the optical regime, particularly on the fine structure of Balmer-α ($n = 2 \rightarrow 3$). At that time, such experiments were hindered by the problem of Doppler broadening. In the 1930's a great deal of effort was put in to trying to reduce the Doppler broadening by various techniques such as the cooling of discharges or the use of deuterium instead of hydrogen. This work suggested that the $2S_{1/2}$ and $2P_{1/2}$ levels were not in fact degenerate as predicted by Dirac theory [7, 8].

The experiment of Lamb and Retherford was pioneering in that it involved radio-frequency spectroscopy of the $2S_{1/2}$-$2P_{1/2}$ interval. The problem of Doppler broadening was completely bypassed. The $2S_{1/2}$ and $2P_{1/2}$ levels were shown to be separated by about 1 GHz—an interval which became known as the "Lamb shift". This work appeared to mark the end of the era of optical spectroscopy as a means of studying small effects in hydrogen,but it is interesting to note that Series and Kuhn were able in 1950 to resolve the Lamb shift in deuterium optically, using a discharge cooled with liquid hydrogen [9].

Lamb and Retherford's demonstration of the inadequacy of Dirac theory stimulated theoretical work on the problem of the interaction of charged particles with the electromagnetic field. This led quickly to the development of quantum electrodynam-

ics (QED), which is currently the most successful theory in physics. It has become the prototype for theories of the other fundamental interactions (e.g. QCD), so it is important to test its predictions as accurately as possible.

To-date, the most precise tests of QED in atoms (so-called "bound state QED") have been based on radio-frequency spectroscopy of the $2S_{1/2}$-$2P_{1/2}$ interval (following the example of Lamb and Retherford). Currently the precision of both theory [10, 11] and experiment [12, 13] are at the level of 1 part in 10^5. Unfortunately, the precision of this measurement is ultimately limited by the 100 MHz natural width of the $2P_{1/2}$ level. The centre of the resonance is already being located to 1 part in 10^4 of this width. It seems unlikely that there will be further substantial improvement in precision. A different approach is needed in order to push the test of QED further.

1.2 The 1S Lamb shift

Attention has turned in recent years to alternative tests of bound state QED. One such is based on the predicted shift of the $1S_{1/2}$ level in hydrogen from its Dirac position—the so-called "1S Lamb shift". As there is no nearby P level, the 1S Lamb shift is defined here as being the difference between the true energy of the level and the Dirac energy including the correction to the Dirac energy arising from the finite nuclear mass. It therefore comprises the sum of all QED corrections, plus a correction for the finite nuclear size (§2.2). It is about 8 times larger than the $2S_{1/2}$ Lamb shift because of the $1/n^3$ scaling of the main QED effects.

Because of the lack of a nearby P level, radio-frequency spectroscopy is not suitable for a measurement of the 1S Lamb shift. An optical experiment is necessary, but not straightforward. Firstly, the nearest level to $1S_{1/2}$ is $2P_{1/2}$ which lies about 10eV away, corresponding to a wavelength of 121.5 nm in the vacuum ultra-violet. Such an experiment would have to be Doppler-free, but this wavelength is inaccessible to currently available tunable laser systems. Secondly, any experiment based on the 1S–2P transition would be subject to a limitation in precision in the same way as the $2S_{1/2}$ Lamb shift measurements described above. In addition, despite the fact that the 1S Lamb shift is the largest in hydrogen—the presently accepted theoretical value is 8173.05 MHz (Table 2.2)—it is still only about 1 part in 10^5 of the total 1S–2P interval of about 2.5×10^{15} Hz. The large interval would have to be measured extremely precisely in order to extract the small quantity of interest.

1.3 The 1S–2S transition

The $1S_{1/2}$-$2S_{1/2}$ transition on the other hand has several advantages over $1S_{1/2}$-$2P_{1/2}$. Its use in a high-resolution laser spectroscopy experiment was first suggested by Cagnac et al [14] in 1973 and Baklanov and Chebotaev [15] in 1974. The $2S_{1/2}$ level is metastable with a lifetime of one eighth of a second. Consequently the 1S–2S

transition has a natural linewidth of only 1.3 Hz and offers the prospect of an extremely precise experiment. Also, because it is a two-photon transition, two-photon Doppler-free spectroscopy may be used in order to take advantage of the extreme narrowness of the line. The wavelength required for the two-photon excitation is 243 nm which is not in the vacuum ultra-violet, and while still outside the range of tunable lasers, it may be generated by frequency doubling the radiation from a dye laser operating in the blue at 486 nm.

However, the problem still remains that the 1S Lamb shift is only a tiny fraction of the 1S–2S interval. The obvious solution is to measure this large interval by calibrating the fundamental output of the doubled laser against a frequency standard. In order to extract the 1S Lamb shift it is then necessary to subtract off the Dirac contribution, which requires the use of a measured value of the Rydberg constant. It is interesting to note that this experiment can be interpreted differently; it can be treated as a measurement of the Rydberg if one assumes that the theoretical value of the 1S Lamb shift is correct.

A more elegant approach was first used by Hänsch and his colleagues at Stanford University in the seventies (the first work was reported by Lee et al. [16]: a complete set of references can be found in [3]). The well-known $1/n^2$ scaling of the hydrogen gross structure means that the $n = 2 \rightarrow 4$ interval is almost exactly equal to one quarter of the $n = 1 \rightarrow 2$ interval. Therefore, a laser operating at 486 nm, frequency-doubled and tuned to resonance with the two-photon 1S-2S transition would have almost exactly the same frequency as a laser tuned to a component of $n = 2 \rightarrow 4$ (Balmer-β). The frequency of the Balmer-β laser will differ from that of the 1S–2S laser by a quantity δ where

$$\delta = \nu(\text{Balmer-}\beta) - \frac{1}{4}\nu(\text{1S–2S}). \tag{1.1}$$

The exact value of δ depends on the particular fine and hyperfine component of Balmer-β and hyperfine component of 1S–2S which are being compared (§2.5). In practice it turns out to be a few gigahertz and is predominantly due to the 1S Lamb shift. The other contributions are known much more accurately. So if δ can be measured directly (for instance by heterodyning the outputs of the two lasers), the 1S Lamb shift can be determined without the problem of extracting a small quantity from a large one to the required accuracy.

We now turn to a review of the work which has already been done.

1.4 Previous work on the 1S–2S transition

1.4.1 Pulsed experiments

As indicated above, the first laser spectroscopy experiments on the hydrogen 1S–2S transition were done in Stanford by Wieman, Hänsch and co-workers between

1975 [16] and 1979 [3], and were based on a direct comparison of 1S–2S and a component of Balmer-β. Since both second harmonic generation (frequency doubling) and two-photon absorption are non-linear processes, the early experiments used pulsed laser sources in order to take advantage of the high peak power. In the earlier work, the 1S–2S transition was excited using a 486 nm pulsed dye laser, frequency-doubled in lithium formate monohydrate (LFM) and Balmer-β was studied using saturated absorption spectroscopy with the same laser. In the later work, the same continuous-wave dye laser was used for each transition. Before being doubled (also in LFM), the blue light was amplified in a pulsed dye amplifier. Polarisation spectroscopy was used for the 2S–4P comparison transition. This experiment yielded a value of 8151(30) MHz for the hydrogen 1S Lamb shift and 8177(30) MHz for the same quantity in deuterium. The large error arose mainly from the large linewidth ($\sim$100 MHz) of the pulsed source and frequency chirping effects in the pulsed dye amplifiers.

In 1986 Barr et al in Southampton obtained the value of 8182(25) MHz for the hydrogen 1S Lamb shift [17]. Once again the two-photon transition was excited with pulsed radiation but this time its frequency was measured by interferometrically comparing the fundamental output of the doubled laser to a previously calibrated line in molecular tellurium ($^{130}Te_2$). The pulsed radiation was spectrally filtered using a confocal interferometer to reduce the laser linewidth to 30 MHz. Hildum et al. [18] used a similar technique to measure the 1S Lamb shift with a precision of 5.4 MHz.

1.4.2 Continuous-wave experiments

The precision of all the aforementioned experiments was fundamentally limited by the use of pulsed radiation to excite the 1S–2S transition. It was therefore clear that continuous-wave (cw) experiments would be necessary to exploit the potential resolution available with 1S–2S. However, the production of an adequate quantity of cw 243 nm radiation was not straightforward. Problems existed with all the non-linear crystals used for second-harmonic generation up to 1986. LFM suffered badly from surface damage caused by the generated UV radiation and was therefore unusable. Urea was slightly better in that it had a higher conversion efficiency than LFM and was less susceptible to damage. However, its main disadvantage was that it was very soft (making polishing of the crystal surfaces difficult) and sensitive to moisture.

The Stanford group chose to bypass the difficulties associated with continuous-wave frequency doubling and instead pursued a different route to a cw experiment. A few milliwatts of cw 243 nm radiation were produced by sum-frequency mixing the outputs from a 790 nm dye laser and a 351 nm argon ion laser in a crystal of potassium dihydrogen phosphate (KDP). The frequency calibration was provided by the tellurium standard mentioned above in §1.4.1. A 486 nm dye laser was locked to the tellurium line and a small amount of its second harmonic (generated in a single pass through a crystal of urea) was heterodyned with the 243 nm radiation exciting the 1S-2S transition. In this way, the Stanford group were able to make the first continuous-wave measurement of the 1S Lamb shift [19, 2]. The value obtained was

8173.3(1.7) MHz—a factor of 15 improvement on the precision of the previous best result.

Meanwhile the group at Oxford continued working towards frequency-doubling of continuous-wave 486 nm light. The lack of a suitable non-linear crystal hindered progress for several years until in 1987 a new material, β-barium borate (BBO), became available from China. BBO has a good conversion efficiency at 486 nm and suffers very little from UV induced surface damage. Boshier and co-workers in Oxford had had some success with urea as a doubling material (the 1S–2S transition had been excited in this way) and were therefore in a position to take immediate advantage of this new crystal. Two or three milliwatts of continuous-wave 243 nm radiation were generated by placing a Brewster-cut crystal of BBO inside the cavity of a 486 nm ring dye laser. The frequency calibration of the 1S–2S transition was once again provided by the tellurium standard. One 486 nm laser was locked to the tellurium line and heterodyned with the fundamental of the doubled laser. The experiment yielded the results of 8172.6(7) MHz and 8183.7(6) MHz for the 1S Lamb shifts in hydrogen and deuterium respectively [20, 1, 21].

The main source of error in the above experiment was the tellurium standard. The relevant line had been calibrated by the National Physical Laboratory (NPL) against a standard HeNe, which in turn had been compared to a National Bureau of Standards (NBS) HeNe. The latter had been used in a measurement of the Rydberg constant by Zhao et al [22], based on spectroscopy of Balmer-β. A considerable improvement in precision would result from bypassing the intermediate steps and performing a direct comparison of 1S–2S and Balmer-β (as outlined in §1.3) in a continuous-wave experiment. It should also be noted that it was found during the course of the Oxford work that nominally identical tellurium cells in fact differed quite appreciably in their characteristics. In addition, there was some question about the correct operating temperature. This was important because the frequencies of the tellurium lines depend on the vapour pressure in the cell, which in turn is temperature dependent. The reproducibility of tellurium cells has recently been comprehensively studied by Barwood et al. from the NPL [23]. They found that different cells obtained from the same manufacturer contained varying amounts of tellurium. The working temperature of the cells has generally been characterised by the absorption on a given line. Some of the cells contained insufficient tellurium to achieve this absorption. They also found that temperature and vapour pressure measurements could be made more reliably using a redesigned cell and oven. The original cell (used for the frequency calibration in [1]) was compared to a number of these new cells and no difference was found in the frequencies of the tellurium lines. Therefore, the results obtained using that cell are not affected by the recent findings. While the investigations of Barwood et al. have shown that, with careful use, the cell to cell reproducibility of tellurium standards is not as bad as once feared, it is clearly preferable for future Lamb shift experiments to be less dependent on these for frequency calibration.

In all the above continuous-wave experiments, the 1S–2S transition was excited

in a gas cell of hydrogen atoms. Collisional effects (pressure broadening and shifts) were very significant and had to be corrected for. It would be preferable to do away with these effects by exciting the 1S–2S transition in a collision-free environment, i.e. in an atomic beam.

1.5 The present experiment

The measurement of the 1S Lamb shift made by Boshier et al. gave a precision of 1 in 10^4. The theoretical number for the same quantity is at the level of 1 in 10^5. (A more detailed discussion of the theoretical calculation and associated uncertainties will be given in Chapter 2.) An improvement of an order of magnitude in precision will be necessary before the experimental work on the 1S Lamb shift becomes comparable with theory or indeed begins to rival the $n = 2$ Lamb shift as the most precise test available of bound state QED.

The experiment described in this thesis was intended as a first step towards achieving the required improvement in precision. It had two major objectives. The first was to do away with the uncertainties associated with cell excitation by exciting the 1S–2S transition in an atomic beam environment. Secondly, the tellurium calibration has been replaced by a direct comparison with Balmer-β using continuous-wave lasers. The purpose of the work was to demonstrate the feasibility of a direct cw comparison of 1S–2S and Balmer-β as a step towards an eventual high precision measurement of the 1S Lamb shift. The earlier experiments of Hänsch and co-workers which made use of this comparison involved pulsed radiation which leads to a large uncertainty as mentioned earlier (§1.4.1). Even the present prototype experiment has given considerably better precision.

The principle of the experiment is as follows. The 1S–2S transition is excited in a ground state atomic hydrogen beam using continuous-wave 243 nm radiation produced by frequency doubling in BBO the output from a 486 nm ring dye laser. This process creates a beam of metastable (2S) hydrogen atoms which can be used for the Doppler-free excitation of a component of Balmer-β by a second 486 nm ring dye laser. The frequency difference δ introduced in §1.3 is then directly measured.

The final precision of this experiment depends primarily on the precision achieved on the calibration transition. The choice of Balmer-β component is therefore very important. Two possibilities present themselves— $2S_{1/2}$-$4S_{1/2}$ and $2S_{1/2}$-$4P_{1/2}$ (or $4P_{3/2}$).

The natural width of the 2S–4S transition is 700 kHz compared to 13 MHz for the 2S–4P. Therefore a more precise measurement of the frequency interval δ and hence the 1S Lamb shift would be possible if 2S–4S were used. However, the 2S–4S transition is more difficult experimentally. Selection rules forbid the single photon transition, so one is forced to look at other options such as two-photon Doppler-free spectroscopy at 972 nm, an optical photon at 486 nm plus a radio-frequency photon or a Stark-assisted single photon excitation at 486 nm. In contrast, either of the

2S–4P transitions can be simply excited using a single photon at 486 nm, but do not offer the prospect of such a precise measurement.

With these factors in mind, it was decided to use the 2S–4P transition as the calibration for the initial experiments, sacrificing some precision in the first instance. This is acceptable in a pilot experiment. We note that subsequent to the work described in this thesis, the Münich group have reported an experiment based on a direct comparison of 1S–2S and 2S–4S which gave a result for the 1S Lamb shift with a precision of 1.3 parts in 10^5 [24].

1.6 The layout of this thesis

In this thesis, Chapter 2 contains a brief overview of the theory of hydrogenic atoms, including the QED corrections to the energy levels. The theory is used to obtain values for the hydrogen 1S Lamb shift, the energies of the various levels of interest in this work and the frequency interval δ (introduced in §1.3 above) for the appropriate components of Balmer-β. In Chapter 3, the theoretical background to the Doppler-free two-photon excitation of 1S–2S is considered and the dependence of the 1S–2S signal rate on various experimental parameters is considered. The next two chapters describe the experimental apparatus required for the 1S–2S excitation. Chapter 4 contains an account of the development of the 243 nm enhancement cavity which formed the 1S–2S interaction region. Details of the rest of the apparatus are covered in Chapter 5. In Chapter 6, attention is turned to the second part of the experiment—the excitation of the chosen component of Balmer-β and the determination of the frequency interval δ. The chapter opens with a calculation of the expected signal rate before going on to the apparatus required for this part of the experiment. The analysis of the data leading to a measured value of the 1S Lamb shift is covered in Chapter 7. Finally, in Chapter 8, this work is set in context with other tests of bound state QED in hydrogenic systems and the implications for future work on the 1S Lamb shift in hydrogen itself are considered.

Chapter 2

Theory of hydrogenic atoms

2.1 Introduction

In this chapter, a brief outline will be given of the theoretical basis for the calculation of hydrogenic energy levels. This will include the contribution from the solutions of the Dirac equation (plus corrections for the finite nuclear mass), the correction for the finite size of the nucleus and the various QED corrections. A theoretical value for the 1S Lamb shift and the total energies of several hydrogen energy levels will be given. These values will be used to calculate the frequency interval δ (referred to in §1.3) for the $2S_{1/2}$–$4P_{1/2}$ and $2S_{1/2}$–$4P_{3/2}$ transitions.

2.2 The energy levels of hydrogenic atoms

2.2.1 Non-QED contributions

The starting point for a calculation of the energy levels of a hydrogenic atom is the Dirac equation for an electron of mass m and charge $-e$ in the Coulomb field of a stationary point nucleus of charge $+Ze$. The solutions to this equation have the form [25]

$$E_D = -\frac{2hcR_\infty}{\alpha^2}\left\{1-\left[1+\left(\frac{Z\alpha}{n-\epsilon}\right)^2\right]^{-1/2}\right\} \tag{2.1}$$

where

$$\epsilon = (j+1/2)-\left[(j+1/2)^2-(Z\alpha)^2\right]^{1/2},$$

n is the principal quantum number, j is the total angular momentum quantum number, α is the fine structure constant and R_∞ is the Rydberg constant for infinite nuclear mass:

$$R_\infty = \frac{1}{hc}\frac{1}{(4\pi\epsilon_0)^2}\left[\frac{me^4}{2\hbar^2}\right]. \tag{2.2}$$

We now take into account the fact that the atomic nucleus has a finite mass M. In a non-relativistic treatment, all energies are multiplied by the reduced mass factor μ/m, where

$$\mu = \frac{mM}{m+M}. \tag{2.3}$$

This result does not hold exactly in the relativistic treatment, however. As a result, an extra correction is required with the leading term [11]

$$\delta E_{RN} = -\frac{\mu}{m+M}\frac{\alpha^2}{4}\frac{Z^4}{n^4}\frac{\mu}{m}hcR_\infty. \tag{2.4}$$

This term will be referred to here as the "relativistic two-body correction".

All but one of the remaining corrections to the energy levels are due to QED effects. The term "Lamb shift" will be used to mean the difference between the true energy of a level and the Dirac energy including the corrections given above. It therefore consists of all the QED corrections plus a correction for the finite nuclear size (see below). This differs from the usual use of the term "Lamb shift" to mean the differential shift between, for example, the $2S_{1/2}$ and $2P_{1/2}$ levels.

2.2.2 QED corrections

The QED shifts arise from the perturbing effects of interactions with virtual particles. Nearly all the QED terms are proportional to the value of the electronic wavefunction at the nucleus, so the main effect is a shift of the S-states. The shifts of the corresponding P-states are very small in comparison.

The QED corrections are calculated by performing a perturbation expansion on Dirac basis states. This results in a series

$$\delta E_{QED} = -Z^2 hcR_\infty \left\{ \left(\frac{\alpha}{\pi}\right)\epsilon_2 + \left(\frac{\alpha}{\pi}\right)^2 \epsilon_4 + \cdots \right\}. \tag{2.5}$$

In this expansion, ϵ_i is the QED radiative correction of order i. For low Z, each of the terms in the above can be further expanded in a dimensionless series as a function of $Z\alpha$.

The second order radiative shift ϵ_2 comprises the sum of the contributions from all processes involving two interactions with virtual particles. The largest contribution to this term is the second order self energy δE_{SE}, which makes up 98% of the Lamb shift of S-states. It may be written [26]

$$\delta E_{SE} = \frac{\alpha}{\pi}\frac{(Z\alpha)^4}{n^3}F_{SE}(Z\alpha)mc^2. \tag{2.6}$$

where $F_{SE}(Z\alpha)$ is a slowly varying function of $Z\alpha$. It is useful to express $F_{SE}(Z\alpha)$ in terms of its explicit contributions [26]:

Table 2.1: The published values of $G_{SE}(Z\alpha)$.

Author	$G_{SE}(Z\alpha)$	Contribution to self energy
Erickson [11]	-19.12	-1.11(3) MHz
Mohr [10]	-23.25	-1.34(7) MHz
Sapirstein [27]	-24.9	-1.44(5) MHz

$$\begin{aligned} F_{SE}(Z\alpha) \;=\; & \frac{4}{3}\left\{\left[\ln(Z\alpha)^{-2}+\frac{11}{24}\right]\delta_{l0}+L_{nl}\right. \\ & +\frac{3}{8}\frac{C_{jl}}{(2l+1)}+Z\alpha C_5 \\ & \left.+(Z\alpha)^2\left[C_{62}\ln^2(Z\alpha)^{-2}+C_{61}\ln(Z\alpha)^{-2}\right]+(Z\alpha)^2 G_{SE}(Z\alpha)\right\}. \end{aligned} \tag{2.7}$$

The first three terms in the above have been calculated analytically. The quantity L_{nl} is the Bethe logarithm for a level with principal quantum number n and orbital angular momentum quantum number l (values of which are tabulated in [11]). The next term in equation 2.7 is the contribution from the anomalous magnetic moment of the electron. The coefficient C_{jl} has the value $1/(l+1)$ when $j = l+1/2$ and $-1/l$ when $j = l-1/2$. This term is the largest contribution to P-state Lamb shifts.

The remaining terms in equation 2.7 comprise the so-called "binding correction" to the second order self energy. The coefficients C_5, C_{61} and C_{62} have known analytical values [26], but the higher order remainder $G_{SE}(Z\alpha)$ must be calculated numerically. Several authors have published results for $G_{SE}(Z\alpha)$, but there is some discrepancy between them (see Table 2.1). The values of Mohr and Sapirstein are similar; that of Mohr has been used to obtain the results used here for the 1S Lamb shift. It does in fact give values of Lamb shifts closer to experimental results than that of Erickson.

The coefficients of the series $F_{SE}(Z\alpha)$ can also be expanded in terms of the small quantities m/M and Zm/M, giving rise to relativistic reduced mass and relativistic recoil corrections to the self energy. These are corrections arising from the effects of a finite nuclear mass.

The next largest contribution to the Lamb shift of S-states is the vacuum polarisation correction (also second order). This results from the polarisation of the vacuum near the nucleus by virtual electron-positron pairs, which modifies the Coulomb potential. The vacuum polarisation correction can be expanded as a dimensionless series $H(Z\alpha)$ in a similar way to the self energy [28]. The effect of the lowest order term is a downward shift of the S-states given by adding $-1/5$ to the $11/24$ in equation 2.7. The expansion of the vacuum polarisation also contains binding corrections, relativistic reduced mass and relativistic recoil corrections.

The QED corrections which remain come from the higher order (fourth order and above) terms in the QED expansion of equation 2.5. These "higher order" corrections arise from interactions with more than one virtual photon and are smaller than the second order terms by at least a factor of α.

2.2.3 Finite nuclear size correction

The one remaining correction to the hydrogenic energy levels which must be considered here is the effect of the finite size of the nucleus. This is not a QED effect but is it is convenient to include it in the Lamb shift because it has the same $1/n^3$ dependence as most of the QED terms. A first order perturbation treatment of the modification of the Coulomb potential near the nucleus is adequate for the accuracy required here. The correction turns out to be proportional to the mean square nuclear charge radius $< r^2 >$.

Table 2.2 shows the various contributions to the 1S Lamb shift in atomic hydrogen. These are based on the calculations of Boshier [21], which were carried out using the results of Johnson and Soff [26] with some extra reduced mass corrections. Because all the QED terms (and the Dirac energies plus corrections) are proportional to the Rydberg R_∞, it is possible to scale all the results to the current best value of R_∞:

$$R_\infty = 109\ 737.315\ 709(18)\ \text{cm}^{-1}\ [29].$$

This introduces a correction to Boshier's results of only 2 parts in 10^{11}, which makes no difference to the quantities in Table 2.2 but does slightly affect the total energies of the levels (see below). The other constants used in the calculation were:

$$\begin{aligned} c &= 299\ 792\ 458\ \text{ms}^{-1}\ [30] \\ \alpha &= 1/137.0359895(61)\ [31] \\ m_e/M_p &= 1836.152701(37)\ [32] \\ < r^2 >^{1/2} &= 0.86(2)\ \text{fm}\ [33] \end{aligned}$$

2.3 Uncertainties in the 1S Lamb shift

The various sources of uncertainty in the calculated value of the 1S Lamb shift are shown in Table 2.3. The uncertainty in the higher order binding term comes directly from the quoted uncertainty in the value of $G_{SE}(Z\alpha)$ used in the calculation (see Table 2.1). The third entry in Table 2.3 is an estimate by Erickson [11] of the uncertainty arising from uncalculated higher order radiative shifts. The uncertainty in the fine structure constant is at the level of 1 part in 10^7.

Table 2.2: The contributions to the hydrogen 1S Lamb shift.

Total self energy	8383.29 MHz
Total vacuum polarisation	-214.82 MHz
Total higher order QED	1.02 MHz
Relativistic recoil corrections	2.39 MHz
Finite nuclear size correction	1.16 MHz
Total 1S Lamb shift	8173.05 MHz

Table 2.3: Contributions to the uncertainty in the calculated 1S Lamb shift.

Higher order binding	73 kHz
Proton charge radius	55 kHz
Higher order QED	45 kHz
Fine structure constant	1 kHz
Total (added in quadrature)	102 kHz

Table 2.4: Hyperfine splittings of the levels considered in this chapter.

Level	HF splitting (MHz)
$1S_{1/2}$	1420.406
$2S_{1/2}$	177.557
$4S_{1/2}$	22.190
$4P_{1/2}$	7.398
$4P_{3/2}$	2.959

There is some difficulty over the value of the root mean square proton charge radius $< r^2 >^{1/2}$. Early measurements (from electron scattering experiments) yielded the value 0.80(2) fm, whereas more recent experiments [34] have given 0.862(12) fm. The value used to calculate the results given here was 0.86(2) fm, obtained from a re-analysis of all the data by Sick [33].

The uncertainty in the current best value of the Rydberg constant is 2 parts in 10^{10}, which contributes only about 1 Hz to the uncertainty in the 1S Lamb shift, but approximately 0.6 MHz to the uncertainty in the absolute energy of the $1S_{1/2}$ level.

2.4 Hyperfine structure

For our purposes, relativistic and QED corrections to the hyperfine structure are negligible, so it is adequate to use the formula [35]

$$\Delta E_{HFS} = \frac{Z^3}{n^3}\alpha^2 g_I \frac{m}{M} hcR_\infty \frac{F(F+1) - I(I+1) - j(j+1)}{j(j+1)(2l+1)}, \tag{2.8}$$

where g_I is the nuclear g-factor, I is the nuclear spin (1/2 for hydrogen) and F is the total angular momentum quantum number. The hyperfine splittings of the levels to be considered in this chapter are shown in Fig. 2.1 and also presented in Table 2.4.

2.5 Calculation of frequency intervals

It had been decided (§1.5) that in this experiment, the frequency of 1S–2S would be compared to that of 2S–4P. In this section, the interval between the transition frequency of each component of 2S–4P and one quarter of the 1S–2S frequency will be

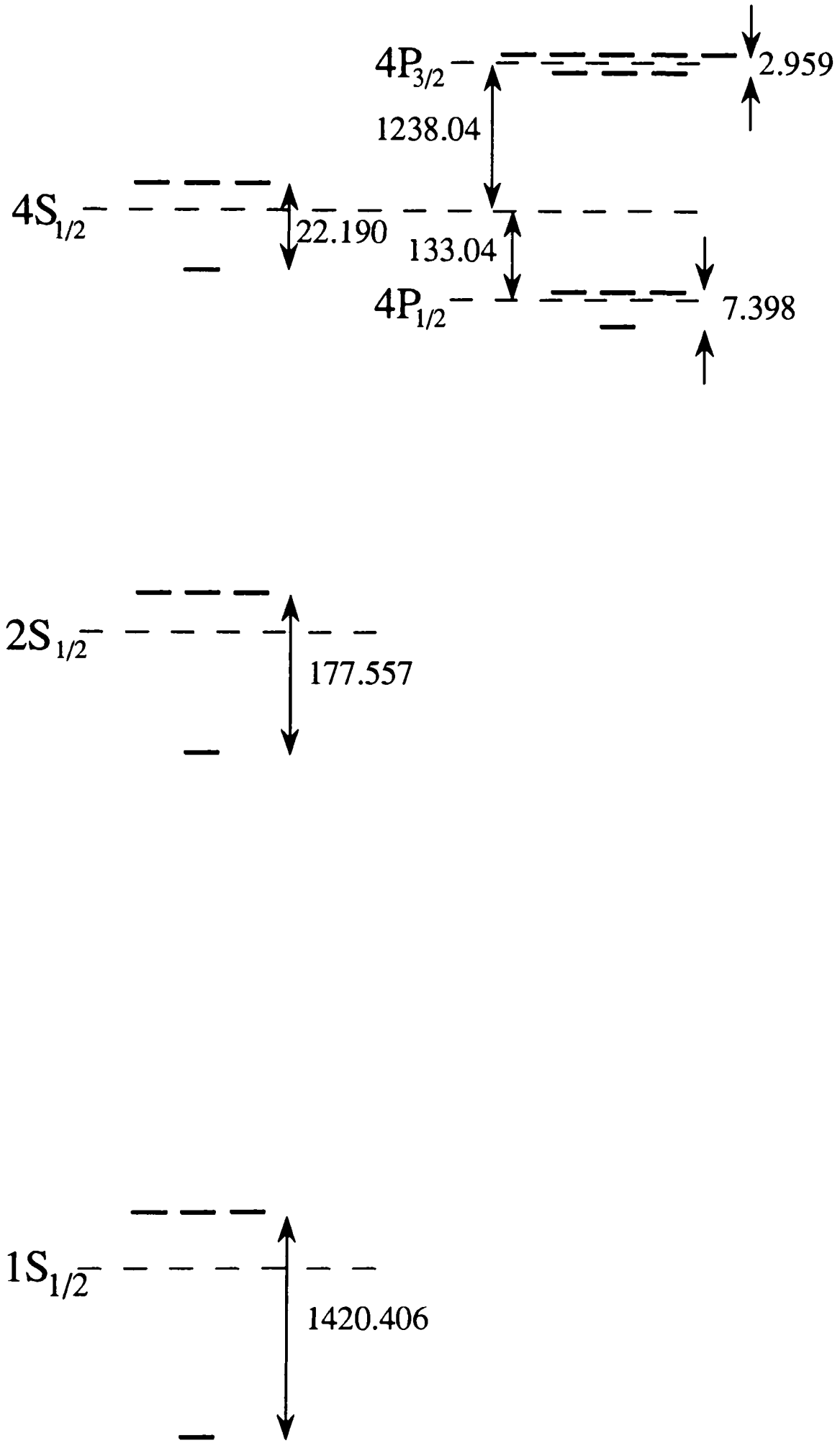


Figure 2.1: The hyperfine splittings of the $1S_{1/2}$, $2S_{1/2}$, $4S_{1/2}$, $4P_{1/2}$ and $4P_{3/2}$ levels in hydrogen (not to scale). All intervals are in MHz.

Table 2.5: The energies of the $1S_{1/2}$, $2S_{1/2}$ and $4S_{1/2}$ levels in hydrogen plus the 1S–2S and 2S–4S transition frequencies.

$1S_{1/2}$ total energy	-3 288 086 858.23 MHz
$2S_{1/2}$ total energy	-822 025 444.24 MHz
$4S_{1/2}$ total energy	-205 505 293.39 MHz
$\nu(1S_{1/2}$–$2S_{1/2})$ centroid–centroid	2 466 061 413.99 MHz
$\nu(1S_{1/2}$–$2S_{1/2})F = 1 \rightarrow F' = 1$	2 466 061 103.27 MHz
$\frac{1}{4}\nu(1S_{1/2}$–$2S_{1/2})F = 1 \rightarrow F' = 1$	616 515 275.82 MHz
$\nu(2S_{1/2}$–$4S_{1/2})$ centroid–centroid	616 520 150.85 MHz

calculated. We must now be specific about the definition of the quantity δ introduced in §1.3. Throughout the experiment, only the stronger hyperfine component of 1S–2S ($F = 1 \rightarrow F' = 1$) was excited (§3.4). The hyperfine components of 2S–4P were not resolved by the Balmer-β excitation. Because only the $F = 1$ level was populated in the metastable beam, the intensities of the hyperfine components were in the ratios 2:1 for $2S_{1/2}$–$4P_{1/2}$ and 5:1 for $2S_{1/2}$–$4P_{3/2}$(see §6.3.1). The centre of gravity of the hyperfine components must be calculated accordingly. The quantity δ which is given directly from this experiment is the difference between the experimental centre frequency of the 2S–4P resonance and one quarter of the frequency of the $F = 1 \rightarrow F' = 1$ component of 1S–2S.

The calculations for $2S_{1/2}$–$4P_{1/2}$ and $2S_{1/2}$–$4P_{3/2}$ are presented in Tables 2.6 and 2.7. The $2S_{1/2}$–$4S_{1/2}$ and $1S_{1/2}$–$2S_{1/2}$ transition frequencies have been obtained from the total energies of the levels calculated by Boshier [21], updated to the new Rydberg (Table 2.5). The small intervals between $4S_{1/2}$ and $4P_{1/2}$ or $4P_{3/2}$ have been obtained from the calculations of Erickson [11]. Updating the Rydberg constant from that used by Erickson to the current best value would introduce a correction to all quantities of 2 parts in 10^8. While this would be approximately 12 MHz in the total 4P energy, it is only ~ 3 Hz in the 4S–4P difference–well beyond the precision of this experiment. Erickson's results are therefore used directly with no correction for the Rydberg. The 2S–4P centroid to centroid frequency is calculated and the appropriate hyperfine corrections added to give the frequencies of the two hyperfine components. The intervals δ_L and δ_U (corresponding to the lower and upper hyperfine components respectively) are obtained from these by subtracting off a quarter of the 1S–2S frequency. The appropriate centre of gravity is determined and δ calculated.

Table 2.6: Calculation of δ for the comparison transition $2S_{1/2}$–$4P_{1/2}$.

$\nu(2S_{1/2}$–$4S_{1/2})$ centroid–centroid	616 520 150.85 MHz
$\nu(4S_{1/2}$–$4P_{1/2})$ centroid–centroid	133.08 MHz
$\nu(2S_{1/2}$–$4P_{1/2})$ centroid–centroid	616 520 017.77 MHz
$\nu(2S_{1/2}$–$4P_{1/2})$ $F = 1 \rightarrow F' = 0$	616 519 967.83 MHz
$\nu(2S_{1/2}$–$4P_{1/2})$ $F = 1 \rightarrow F' = 1$	616 519 975.23 MHz
$\frac{1}{4}\nu(1S_{1/2}$–$2S_{1/2})$ $F = 1 \rightarrow F' = 1$	616 515 275.82 MHz
δ_L	4 692.01 MHz
δ_U	4 699.41 MHz
δ	4 696.94 MHz

Table 2.7: Calculation of δ for the comparison transition $2S_{1/2}$–$4P_{3/2}$.

$\nu(2S_{1/2}$–$4S_{1/2})$ centroid–centroid	616 520 150.85 MHz
$\nu(4S_{1/2}$–$4P_{3/2})$ centroid–centroid	1 238.04 MHz
$\nu(2S_{1/2}$–$4P_{3/2})$ centroid–centroid	616 521 388.89 MHz
$\nu(2S_{1/2}$–$4P_{3/2})$ $F = 1 \rightarrow F' = 1$	616 521 342.65 MHz
$\nu(2S_{1/2}$–$4P_{3/2})$ $F = 1 \rightarrow F' = 2$	616 521 345.61 MHz
$\frac{1}{4}\nu(1S_{1/2}$–$2S_{1/2})$ $F = 1 \rightarrow F' = 1$	616 515 275.82 MHz
δ_L	6 066.83 MHz
δ_U	6 069.79 MHz
δ	6 069.30 MHz

Chapter 3

Feasibility study for the 1S–2S excitation

In this chapter, estimates are made of various quantities relevant to the choice of conditions for the observation of the two-photon signal. Firstly, second order time-dependent perturbation theory is used to obtain an expression for the two-photon absorption rate. Some general remarks about the nature of two-photon spectroscopy follow. Next, the expression is applied to the specific case of the 1S–2S transition in hydrogen and the geometry of our experiment, taking into account various loss mechanisms and the detection efficiency. From the resulting expression, values for the expected signal rate under various experimental conditions are obtained.

3.1 The two-photon excitation rate

The two-photon excitation rate is calculated using second order time-dependent perturbation theory. This has been done by various authors [36, 37]: only an outline will be given here.

Consider an atom with unperturbed Hamiltonian H_0 and levels $|j>$ such that

$$H_0|j>= E_j|j> . \tag{3.1}$$

The atom has ground state $|g>$ and excited state $|e>$. It is moving with velocity $\mathbf{v}$ and interacts with two laser beams, each of angular frequency ω (in the lab frame) where $2\omega \approx \omega_{eg}$ and $w_{eg} = (E_e - E_g)/\hbar$. It is assumed that all other states $|i>$ are far detuned from resonance, ie.

$$|\omega_{ig} - \omega| \gg \Gamma_i \tag{3.2}$$

where Γ_i is the relaxation rate of the state $|i>$. We suppose that $|g>$ and $|e>$ have the same parity, and that the two-photon process is allowed (the single photon electric dipole transition $|g> \rightarrow |e>$ of course is not).

The two laser beams (initially assumed monochromatic) with which the atom is interacting are written

$$\mathbf{E_1} = \boldsymbol{\epsilon}_1 \frac{\mathcal{E}_1}{2} \{\exp[i(\omega t - \mathbf{k_1}.\mathbf{r}')] + \exp[-i(\omega t - \mathbf{k_1}.\mathbf{r}')]\} \tag{3.3}$$

$$\mathbf{E_2} = \boldsymbol{\epsilon}_2 \frac{\mathcal{E}_2}{2} \{\exp[i(\omega t - \mathbf{k_2}.\mathbf{r}')] + \exp[-i(\omega t - \mathbf{k_2}.\mathbf{r}')]\} \tag{3.4}$$

In the above expressions, the amplitudes, polarisation vectors and wavevectors of the two laser beams are $\mathcal{E}_1$,$\mathcal{E}_2$, $\boldsymbol{\epsilon}_1$, $\boldsymbol{\epsilon}_2$ and $\mathbf{k_1}$,$\mathbf{k_2}$. The position vector of the atom at time t is $\mathbf{r}'$. In the atom's frame, the frequencies of the laser beams are

$$\omega_1 = \omega - \mathbf{k_1}.\mathbf{v} \tag{3.5}$$

$$\omega_2 = \omega - \mathbf{k_2}.\mathbf{v} \tag{3.6}$$

where $\mathbf{v}$ is the atomic velocity. The total field acting on the atom is $\mathbf{E} = \mathbf{E_1} + \mathbf{E_2}$. The time-dependent perturbation due to the laser beams is

$$V(t) = e\mathbf{r}.\mathbf{E} \tag{3.7}$$

the matrix elements $V_{nj}(t)$ of which can be written in the rotating-wave and electric dipole approximations as

$$V_{nj}(t) = < n|e\mathbf{r}.\boldsymbol{\epsilon}_1|j > \frac{\mathcal{E}_1}{2} e^{-i\omega t} + < n|e\mathbf{r}.\boldsymbol{\epsilon}_2|j > \frac{\mathcal{E}_2}{2} e^{-i\omega t} \tag{3.8}$$

where $\mathbf{r}$ is the position vector of the electron at time t.

Second-order time-dependent perturbation theory is then used to calculate the two-photon transition amplitude, assuming counterpropagating beams ($\mathbf{k_1} = -\mathbf{k_2} = \mathbf{k}$) and, in addition to the condition expressed in equation 3.2, that the detuning of the intermediate states is much larger than the Doppler width:

$$|\omega_{jg} - \omega| \gg |\mathbf{k}.\mathbf{v}| \tag{3.9}$$

The transition amplitude has three terms. Two of these describe absorption of two photons from the same laser beam and therefore contain the atomic velocity $\mathbf{v}$. The third term describes absorption of one photon from each laser beam. In this case the first order Doppler shifts cancel and the term is independent of the atomic velocity.

After averaging over the atomic velocity distribution, the velocity-dependent terms give rise to a broad Gaussian background with the Doppler width of the transition. The velocity-independent term gives a narrow Lorentzian lineshape of width $\Gamma_e/2$ (measured at the laser frequency). The area under the Gaussian is half that of the Lorentzian while the width is much larger. In this experiment the ratio would be $\sim 10^9$ were it not for laser bandwidth and transit time broadening (see below) which

reduce it to $\sim 10^3$. The Gaussian background is therefore extremely small and is neglected in the following. The two-photon rate r is then

$$r = \frac{\mathcal{E}_1^2\mathcal{E}_2^2}{16\hbar^4}\left|\sum_j \frac{< g|e\mathbf{r}.\boldsymbol{\epsilon}_1|j >< j|e\mathbf{r}.\boldsymbol{\epsilon}_2|e > + < g|e\mathbf{r}.\boldsymbol{\epsilon}_2|j >< j|e\mathbf{r}.\boldsymbol{\epsilon}_1|e >}{\omega_{jg} - \omega}\right|^2 \times \frac{\Gamma_e}{(\omega_{eg} - 2\omega)^2 + (\Gamma_e/2)^2}. \quad (3.10)$$

In our experiment, the light was linearly polarised, $\boldsymbol{\epsilon}_1 = \boldsymbol{\epsilon}_2 = \boldsymbol{\epsilon}$ and both beams had the same intensity ($\mathcal{E}_1 = \mathcal{E}_2 = \mathcal{E}$). Equation 3.11 then reduces to

$$r = \frac{\mathcal{E}^4}{4\hbar^4}\left|\sum_j \frac{< g|e\mathbf{r}.\boldsymbol{\epsilon}|j >< j|e\mathbf{r}.\boldsymbol{\epsilon}|e >}{\omega_{jg} - \omega}\right|^2 \frac{\Gamma_e}{(\omega_{eg} - 2\omega)^2 + (\Gamma_e/2)^2}. \quad (3.11)$$

The Doppler-free two-photon rate can be seen to depend on $\mathcal{E}^4$, ie. on the *square* of the laser beam intensity.

The treatment as presented so far is only valid if the laser linewidth ($\Delta\omega_L$) is much narrower than the natural width of the transition (Γ_e). This is clearly not the case in this experiment, since the natural width of the 1S–2S transition is of order 1 Hz, while the laser width is a few MHz. However, Grynberg and Cagnac point out in [36] that if $\Delta\omega_L$ is greater than Γ_e, the two-photon transition probability is decreased by a factor of order $\Gamma_e/\Delta\omega_L$; its exact value depends on the phase relation between the monochromatic components of the light. The effect of this is to increase the width of the two-photon signal to a value of order $\Delta\omega_L$ while keeping the area under the lineshape function practically constant. For the purposes of estimating the 1S–2S transition probability in this experiment, we accordingly write the two-photon transition rate as

$$r = \frac{\mathcal{E}^4}{4\hbar^4}\left|\sum_j \frac{< g|e\mathbf{r}.\boldsymbol{\epsilon}|j >< j|e\mathbf{r}.\boldsymbol{\epsilon}|e >}{\omega_{jg} - \omega}\right|^2 \frac{\Delta\omega_L}{(\omega_{eg} - 2\omega)^2 + (\Delta\omega_L/2)^2}. \quad (3.12)$$

3.2 Finite transit time

In our experiment, as in many two-photon Dopper-free experiments, the excitation takes place at the waist of a focussed laser beam. It is therefore necessary to consider the effect on the lineshape of the time taken by the atoms to pass through the beam. Biraben et al. [37] have dealt with the problem of a thermal distribution of atomic velocities and a interaction region at the waist (w_0) of an optical cavity. They find that in this situation, the Lorentzian lineshape factor in equation 3.12 is replaced by the convolution of a Lorentzian and a double exponential:

$$\int_{-\infty}^{\infty} \frac{\Delta\omega_L}{(\omega_{eg} - \Omega)^2 + (\Delta\omega_L/2)^2} \exp\left[-|\Omega - 2\omega|/\delta\right] d\Omega. \quad (3.13)$$

Here $\delta = u/w_0$ where u is the root mean square speed $\sqrt{4KT/M}$ at temperature T. The width of the double exponential (Γ_{TT}) is $2\delta \ln 2$ at the atomic frequency (twice the laser frequency). In the experiment described here, the transit time width was of the same order as the laser linewidth, so the total width was approximately $\Gamma_{TT} + \Delta\omega_L$. Note that the above function is not a convolution of a Lorentzian and a Gaussian, so the lineshape is not a Voigt profile. In fact, it has a sharp point due to the slower atoms, which contribute much to the absorption (owing to being in the laser beam for a longer time) but little to the broadening.

3.3 The effect of collisions

It can be shown [37] that the two-photon lineshape is insensitive to collisions which modify the atomic velocity but not to phase-changing collisions which do give rise to a shift and broadening of the line. Biraben et al. go on to say in [37] that this is true provided that the time taken for the two-photon process to occur (which, by the Uncertainty Principle, is the inverse of the detuning of the other states) must be short compared to the time between collisions τ_c. In the case of the 1S–2S transition, the next nearest state is $\sim 10^{15}$ Hz away so this implies that the time between the absorption of the two photons is $\sim 2 \times 10^{-16}$ s. Presumably this "correlation time" is not to be identified with the ordinary lifetime of the upper level, given the 1.3 Hz natural width of the transition. In any case, the effect is absent in this experiment because the excitation takes place in a collision-free environment.

3.4 Selection rules

Grynberg and Cagnac [36] have defined the two-photon tensor operator

$$Q^s_{\epsilon_1\epsilon_2} = e\mathbf{r}.\boldsymbol{\epsilon}_1 \left[\hbar\omega + E_g - H_0\right]^{-1} e\mathbf{r}.\boldsymbol{\epsilon}_2 + e\mathbf{r}.\boldsymbol{\epsilon}_2 \left[\hbar\omega + E_g - H_0\right]^{-1} e\mathbf{r}.\boldsymbol{\epsilon}_1, \qquad (3.14)$$

which is symmetric provided that the counterpropagating beams have the same frequency. If this is so, $Q^s_{\epsilon_1\epsilon_2}$ is a superposition of a scalar and a quadrupolar operator and has no component of rank 1.

Grynberg and Cagnac show that the standard irreducible components of this symmetric operator can have a definite rank (either 0 or 2) for certain values of initial and final angular momentum. For example, if the initial and final J's are equal and have the value 0 or 1/2, the standard irreducible component of $Q^s_{\epsilon_1\epsilon_2}$ is purely scalar. This is the case appropriate to the $1S_{1/2}$-$2S_{1/2}$ transition. By using the Wigner-Eckart theorem, the following selection rules for the total angular momentum F are obtained:

$$\begin{aligned} \Delta F &= 0 \\ \Delta M_F &= 0 \end{aligned} \qquad (3.15)$$

The 1S–2S transition therefore has two hyperfine components: $F = 1 \rightarrow F' = 1$ and $F = 0 \rightarrow F' = 0$, separated by 1243 MHz at the atomic frequency. Grynberg and Cagnac go on to show that the intensity of a given hyperfine component in the "scalar" case is proportional to the level degeneracy $(2F + 1)$. The intensities of the two hyperfine components are therefore in the ratio 3:1, the $F = 1 \rightarrow F' = 1$ component being the stronger.

3.5 The geometry of the experiment

An outline of the geometry of the experiment is given here for the purposes of estimating the expected 1S–2S signal rate. More complete experimental details of the 1S–2S excitation are given in Chapter 5.

Atomic hydrogen was generated in a radio-frequency discharge and transported to the 1S–2S interaction region through PTFE tubing (§5.3). The interaction region was located at the waist of an optical cavity (Chapter 4), which enhanced the 243 nm power from the laser by about an order of magnitude and provided the two counter-propagating beams. In the early stages of the work, the 1S–2S transition was excited and monitored using the method described in [21]: the chamber was pumped with a rotary pump and used as a low pressure ($\sim$0.3 Torr) gas cell. The excited atoms were collisionally transferred to the 2P state in the interaction region (see Fig. 3.1). The resulting Lyman-α fluorescence was monitored by a photomultiplier placed directly over the interaction region. The reason for exciting the transition in this way (hereafter referred to as "cell mode") was to check the performance of the laser, frequency doubling, enhancement cavity and hydrogen source under conditions which had previously [21] been shown to give reliable 1S–2S signals. No feasibility study is presented here for cell mode because it has been done before [21]. During that work, cell mode signals were observed and characterised. They were always about two orders of magnitude smaller than predicted, an effect tentatively ascribed to the inefficiency of the detection method based on collisional transfer.

Once cell mode signals had become commonplace, we moved on to the excitation of 1S–2S in an atomic beam. The atoms emerged into the interaction region through a nozzle at the end of the PTFE tube (§5.3.2). The chamber was pumped with a turbomolecular pump (§5.2) so the pressure was much lower ($\sim 10^{-4}$ mbar). The excited atoms produced in the interaction region travelled a distance (about 8 cm in the first instance) downstream to the detection region, where a small electric field mixed the 2S and 2P states. The resulting Stark-induced Lyman-α fluorescence was monitored by the photomultiplier, now located over the electric field wires. These conditions are referred to hereafter as "beam mode". The excitation of the 1S–2S resonance produced an optically excited beam of metastable hydrogen atoms which was used in the second part of the experiment. Later in the work, the distance travelled by the excited atoms to the detection region was increased to 40 cm, to allow room for the Balmer-β excitation (see Chapter 6). In order to observe the 1S–

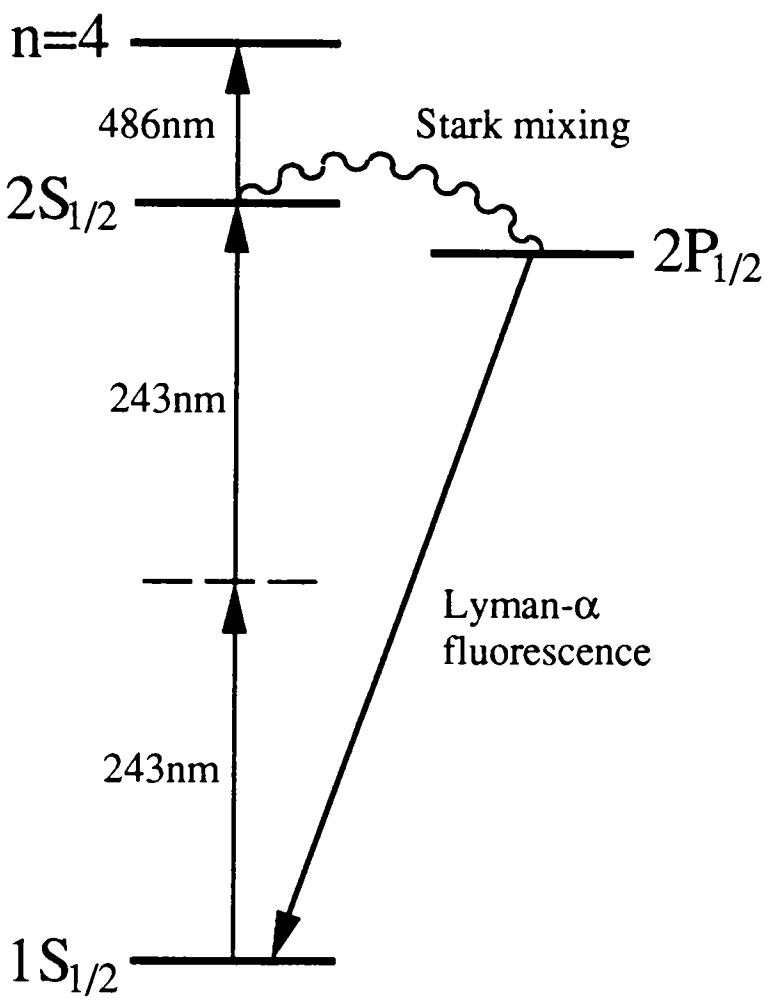


Figure 3.1: The transitions involved in this experiment.

2S signal under these conditions, it was essential to lower the background pressure by using a cryopump as well as the turbopump—the reason for this will be discussed below.

3.6 The expected size of the two-photon signal

From equation 3.12, we can obtain the following expression for the two-photon absorption rate for a single atom in two counterpropagating fields, each of amplitude $\mathcal{E}$ and polarised along the x-axis:

$$r = \frac{\mathcal{E}^4}{4\hbar^4} M^2 \frac{\Delta\omega_L}{(\omega_{eg} - 2\omega)^2 + (\Delta\omega_L/2)^2} \tag{3.16}$$

where

$$M = \left| \sum_j \frac{< g|ex|j >< j|ex|e >}{\omega_{jg} - \omega} \right|. \tag{3.17}$$

The quantity M has been calculated to be 1.36×10^{-74} $\mathrm{C^2m^2s}$ by Bassani et al [38].

On resonance ($\omega = \omega_{eg}/2$), equation 3.16 becomes

$$r = \frac{\mathcal{E}^4}{4\hbar^4} M^2 \times \frac{4}{\Delta\omega_L}. \tag{3.18}$$

However, as pointed out in §3.2, the total linewidth in this experiment is $\Gamma = \Gamma_{TT} + \Delta\omega_L$. The rate then becomes approximately

$$r = \frac{\mathcal{E}^4}{\hbar^4 \Gamma} M^2. \tag{3.19}$$

It is now necessary to calculate the total transition rate in the interaction region. The atoms interact with the laser beams at the waist (radius w_0) of an optical cavity. The length of the laser beam in which the excitation takes place is L, which is much less than the Rayleigh length ($kw_0^2/2$). The z-dependence of the field can therefore be neglected. We may write

$$\mathcal{E}(x, y) = \mathcal{E}_0 \exp\left[-\frac{(x^2 + y^2)}{w_0^2} \right]. \tag{3.20}$$

This is substituted into equation 3.19 and integrated over the interaction volume, which is approximated by a cylinder of length L and base radius w_0, to give the total excitation rate in the interaction region:

$$R = \frac{4}{\pi c^2 \epsilon_0^2 \hbar^4} n_i \frac{L}{w_0^2 \Gamma} P^2 M^2. \tag{3.21}$$

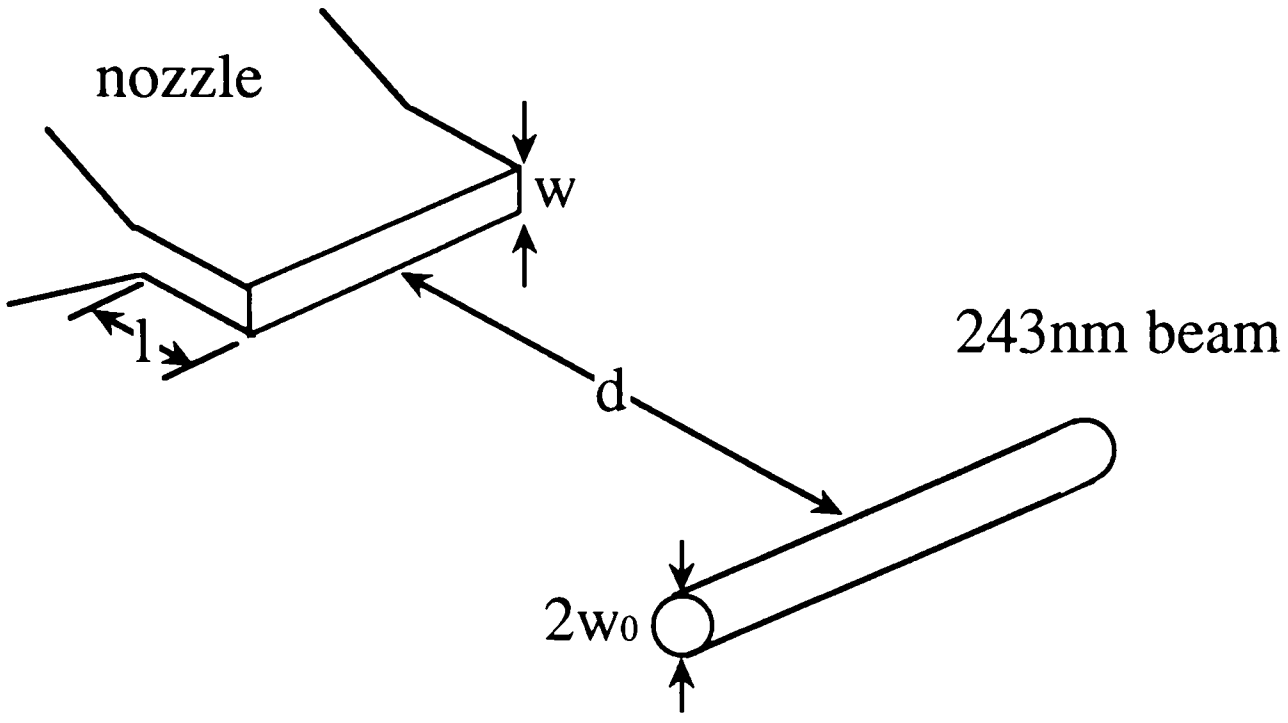


Figure 3.2: The hydrogen nozzle and 1S–2S interaction region.

The relationship between intensity and amplitude ($I = \frac{1}{2}c\epsilon_0\mathcal{E}^2$) has been used, together with $P = I/\pi w_0^2$, where P is the power (in watts) in each beam. The number density (in m^{-3}) of atoms in the interaction region is n_i.

It is now possible to use equation 3.21 to calculate the expected signal under the conditions of this experiment. Strictly speaking, one ought to consider a particular velocity and trajectory for an atom emerging from the source slit, calculate the transition probability for that trajectory through the laser beam, the probability of survival to, and being detected in, the detection region before finally averaging over all atomic velocities and trajectories. However, for the purpose of signal estimates, it is adequate to use a mean atomic velocity to calculate a mean number density of ground state atoms in the interaction region and use equation 3.21 to calculate the excitation rate there. The fraction of these which survive to the detection region and contribute to the observed signal is then estimated from experimental data. The effect of the finite transit time through the interaction region enters the calculation through the transit time width Γ_{TT} of §3.2.

The first step is to calculate the number density of ground state hydrogen atoms in the interaction region. To do this, one needs to know something about the conditions in the hydrogen source. If the pressure in the discharge region is P_1 Torr and χ is the dissociation fraction, the number density n_s of hydrogen atoms at 300 K is

$$n_s = 3.2 \times 10^{22} P_1 \chi \text{ Torr}^{-1}\text{m}^{-3} \tag{3.22}$$

from the ideal gas equation. In beam mode, the atoms emerge into the interaction region through a nozzle with a slit of area A, width w and length l (Fig. 3.2). The number emerging per second (Q) is

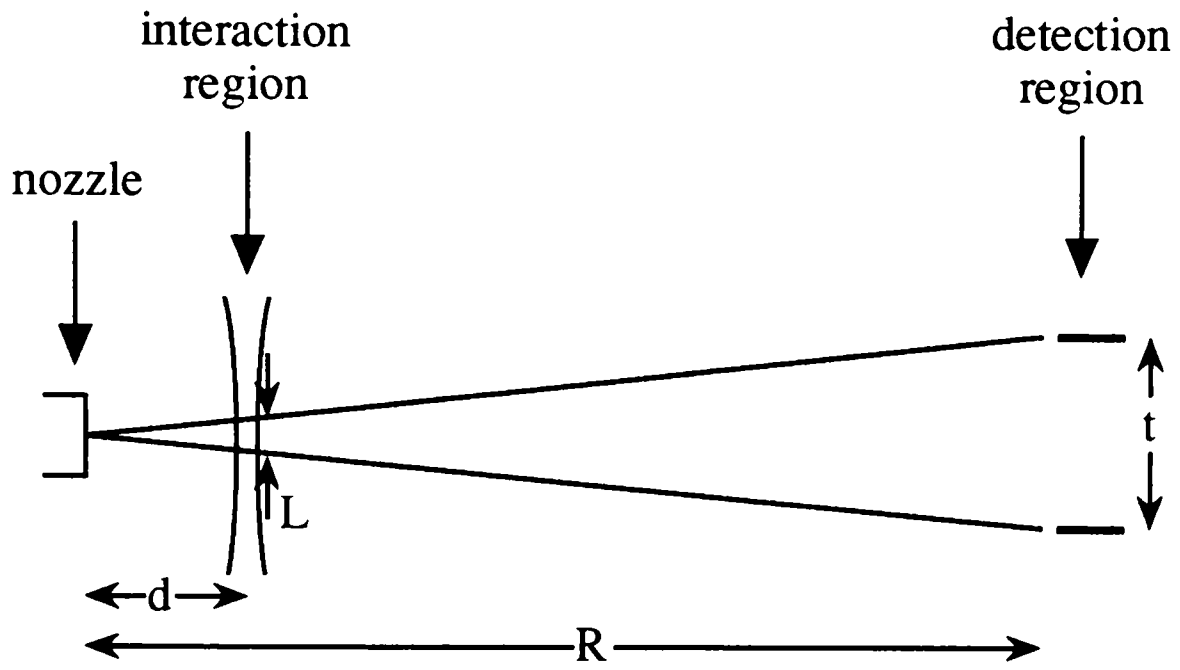


Figure 3.3: Plan view of the atomic beam chamber.

$$\begin{aligned} Q &= \frac{1}{4} n_s \bar{v} A \times \left(\frac{w}{l}\right) \ln\left(\frac{l}{w}\right) \\ &= 8 \times 10^{21} P_1 \chi \bar{v} A \left(\frac{w}{l}\right) \ln\left(\frac{l}{w}\right) \text{ Torr m}^{-3} \end{aligned} \tag{3.23}$$

where $\bar{v}$ is the mean speed at that temperature. In an atomic beam, the mean speed is $3\sqrt{\pi}/4 \times \sqrt{2KT/M}$ [39]. The quantity $\left(\frac{w}{l}\right) \ln\left(\frac{l}{w}\right)$ is the Clausing factor for a rectangular channel with $l \gg w$ [39]. It describes the reduction in total flux through the channel compared to that through an aperture of the same cross-sectional area A and negligible length. The presence of the channel alters the angular distribution of the emerging atoms, resulting in a greater flux in the direction of the channel.

The interaction region formed by the laser beam has a radius w_0 and is a distance d from the nozzle (Fig. 3.2). Assuming (rather pessimistically) that the atoms emerging from the nozzle expand into a solid angle of 2π srad, the number passing per second through unit area a distance d away is $Q(2\pi d^2)^{-1}$. This is of the correct order of magnitude but neglects the forward biassing of the emerging atoms which is increased by the presence of the channel. The mean transit time through the interaction region is approximately $2w_0/\bar{v}$. The approximate number density n_i in the interaction region is

$$\begin{aligned} n_i &\approx Q \times \frac{2}{\pi^2 \bar{v} d^2} \\ &\approx 8 \times 10^{21} P_1 \chi A \left(\frac{w}{l}\right) \ln\left(\frac{l}{w}\right) \times \frac{2}{\pi^2 d^2} \text{ Torr}^{-1}\text{m}^{-3}. \end{aligned} \tag{3.24}$$

Fig. 3.3 shows a plan view of the beam mode geometry. In order to be excited and then reach the detection region (which has a width t and is a distance R from

the nozzle), an atom emerging from the nozzle must pass through a region of the UV beam of length L where $L = td/R$. This is the L of equation 3.21.

The number of atoms (n_e) excited per second and en route for the detection region is

$$n_e \approx 4.4 \times 10^{14} \frac{P^2}{w_0^2 \Gamma} \frac{td}{R} P_1 \chi \left(\frac{w}{l}\right) \ln\left(\frac{l}{w}\right) \frac{A}{d^2}. \tag{3.25}$$

To reach the detection region, the metastable atoms have to travel a distance $(R-d)$ through a region of lower pressure P_2 (see Fig. 3.3). Some of them will be lost through collisions with the background gas. The fraction of metastables surviving to the detection region is given by

$$n(R) \approx n_e \exp\left[-\frac{(R-d)P_2}{4.8 \times 10^{-6}}\right] \tag{3.26}$$

where P_2 in in mbar and R and d are in metres. This result comes from the experimental data given by Biraben et al. [40]. The detection efficiency for those metastable atoms which do reach the detection region is ϵ (assuming that they all decay directly under the photomultiplier).

Combining these factors gives the total signal rate S (in counts s^{-1}):

$$S \approx 4.4 \times 10^{14} \frac{P^2}{w_0^2 \Gamma} P_1 \chi \left(\frac{w}{l}\right) \ln\left(\frac{l}{w}\right) A \frac{t}{Rd} \exp\left[-\frac{(R-d)P_2}{4.8 \times 10^{-6}}\right] \epsilon \tag{3.27}$$

This expression can be split up into a number of factors, each representing a different aspect of the experiment, which will be considered in turn.

3.7 The experimental conditions

3.7.1 Laser power and enhancement cavity.

The effect of the laser power and the design of the enhancement cavity are included in the factor

$$\frac{P^2}{w_0^2 \Gamma}. \tag{3.28}$$

Note the dependence of the signal size on the *square* of the laser power. In the early stages of the work, it was possible to get 2–3 mW of 243 nm power from the frequency-doubled laser. We knew from the experience of Boshier [21] that an enhancement in the cavity of about an order of magnitude (resulting in ~20 mW in each beam) would be adequate for cell mode experiments. On moving to beam mode, however, higher laser power was required. The new BBO crystal mount (described in Chapter 5), enabled up to 8 mW of UV power to be obtained from the laser, giving up to 80 mW in each beam in the interaction region.

The waist size w_0 is determined by the design of the enhancement cavity. w_0 also affects Γ through the transit time width $\Gamma_{TT} = 2\ln 2 \times (u/w_0)$ of §3.2. Decreasing w_0 will increase the peak signal rate but also the transit time width, while increasing w_0 will narrow the resonance at the expense of signal. A compromise w_0 must be chosen to give an adequate two-photon signal without excessive transit time broadening. One clearly loses when the waist size becomes large enough for transit time broadening to cease to be the dominant broadening mechanism. The laser linewidth contributes a few MHz (at the laser frequency). We used a waist size of approximately 100 μm, which resulted in a transit time width comparable to this. At a temperature of 300 K, the root mean square speed $u = 2.9 \times 10^3$ ms^{-1}. (Root mean square speed is used here for consistency with §3.2, but in fact there is very little difference between this and the mean speed $\bar{v}$ above.) If the waist size is 100 μm, this gives a transit time width at the atomic frequency of approximately 5 MHz. The total width Γ (at the atomic frequency) is therefore $\sim$10 MHz. The two-photon signal rates expected with this choice of waist are given below in Table 3.2.

3.7.2 The hydrogen source.

The hydrogen source and delivery system are represented by the factor

$$P_1 \chi \left(\frac{w}{l}\right) \ln\left(\frac{l}{w}\right) A. \tag{3.29}$$

For a given pumping speed, the pressure P_1 in the discharge is directly related to the pressure P_2 in the chamber. Pushing P_1 up will tend to increase the signal, but the corresponding rise in P_2 will tend to decrease it (see below), so an optimum P_1 must be found. The relationship between P_1 and P_2 also depends on the area of the slit A. The slit must be large enough to let through an adequate flux of atoms, but small enough that a large difference in pressure can exist between the source and beam chamber. The dissociation fraction χ is difficult to determine experimentally (see §5.3) and may well also be tied up with P_1. Experimentally, the optimum discharge pressure was found to be approximately 0.4 Torr.

The mean free path λ of a ground state hydrogen atom for kinetic collisions at a pressure P is given by [39]

$$\lambda(\text{mm}) \times P(\text{Torr}) = 0.088. \tag{3.30}$$

At 0.4 Torr, the mean free path is 220 μm. We chose to make the slit width roughly the same size so that a significant fraction of the collisions suffered by the atom would be with the PTFE walls of the slit and not with other atoms. This ensured channelling of the atomic beam and prevented a build-up of atoms around the slit region. If the slit was much smaller than this, there would be an insufficient flux of ground state atoms through the interaction region. The dimensions of the slit were 250 μm $\times$ 8 mm, ie. $A = 2$ mm^2. The length of the channel was 2 mm. For these values of w and l, the quantity $\left(\frac{w}{l}\right) \ln\left(\frac{l}{w}\right)$ is 0.25.

3.7.3 The detection region.

The overall efficiency of the detection region is represented by ϵ. The photomultiplier had a quantum efficiency of 10% for Lyman-α. The window was 1 cm in diameter, so if the photomultiplier was 5 mm above the quench region (as it was in beam mode), it saw rather more than 10% of the total solid angle for an atom which decayed directly underneath. This gives a total sensitivity of around 1%. On occasions (particularly in cell mode) the photomultiplier was used with a Lyman-α filter, which had a transmission of 23% at 121.6 nm and reduced the sensitivity to 0.3%.

The effect of the electric field is to cause Stark mixing of the $2S_{1/2}$ and $2P_{1/2}$ levels, thereby shortening the lifetime of the $2S_{1/2}$ level against decay to the ground state. It can be shown [41] that, in the presence of a static electric field $\mathcal{E}$ directed along the z-axis, the Stark-induced decay of the $2S_{1/2}$ level has a lifetime τ_S where

$$\tau_S = \frac{\hbar^2 \left[(\Delta\omega)^2 + (4/\tau_{2P}^2)\right]}{|V|^2} \tau_{2P}. \tag{3.31}$$

In this expression, τ_{2P} is the natural lifetime of the $2P_{1/2}$ level, $\Delta\omega$ is the frequency interval between the levels (ie. the $2S_{1/2}$ Lamb shift) and V is the matrix element

$$V = < 2P_{1/2} | e\mathcal{E}z | 2S_{1/2} > . \tag{3.32}$$

The magnitude of this matrix element can be shown (eg. [42]) to be equal to $3ea_0\mathcal{E}$ where a_0 is the Bohr radius.

Putting the values $\tau_{2P} = 1.6 \times 10^{-9}$ s and $\Delta\omega = 1$ GHz into equation 3.31 one finds that in a field of 30 Vcm^{-1}, the $2S_{1/2}$ lifetime is reduced from 1/8 s to 4×10^{-9} s. The distance travelled by an atom during this time is $\sim$8 μm so it will decay immediately upon reaching the leading edge of the field. For this reason, the voltage step was in practice (§5.5) positioned slightly downstream of the centre of the photomultiplier window. Experiments indicated that if the field was too high, many of the metastables decayed before they reached a point where the photomultiplier could see them.

3.7.4 The beam chamber.

The conditions in the beam chamber are represented by the factor

$$\frac{t}{Rd} \exp\left[-\frac{(R-d)P_2}{4.8 \times 10^{-6}}\right] \tag{3.33}$$

It is obvious that the pressure P_2 in the beam chamber should be kept as low as possible. However, P_2 depends not only on the pumping speed, but also on the pressure P_1 in the hydrogen source. It is also obvious that keeping the nozzle, interaction region and detection region close together (d and R small) will increase the signal. This fact was exploited in the first beam mode experiments (§5.10). The 243 nm beam acted as a collimating slit for the metastable beam generated by the 1S–2S excitation. The

degree of collimation was determined by the distance d. As will be seen in §6.2, we required a full angle spread in the metastable beam of about 1/100th of a radian in order to reduce the transverse Doppler width of the Balmer-β component to around 100 MHz. This collimation was achieved by increasing d to 20 mm. Once R had been increased to 42 cm in order to allow the Balmer-β excitation to be carried out, the background pressure had to be reduced still further (by the use of the cryopump) to make it possible to see a signal at all.

3.7.5 The expected signal rate

The design of the vacuum system allowed a choice of four positions for the detection region: $R = 0, 10, 34$ or 42 cm. $R = 0$ cm was effectively cell mode and is not covered here. We could pump the vacuum chamber either with the turbopump alone (which gave a pressure P_2 of 4×10^{-5} mbar) or with the turbopump plus cryopump (which gave a P_2 of 1.2×10^{-5} mbar). The nozzle to interaction region distance d is taken to be 2 cm: this was the largest value of d allowed by the version of the apparatus used in the experiment described here and therefore that which gave the best possible collimation of the metastable beam.

Table 3.2 gives the calculated signal S (in counts s^{-1}) for different combinations of P_2 and R—the other quantities in equation 3.27 having the values given in Table 3.1. The predicted signal sizes are probably on the high side, since the calculation assumed 100% dissociation (though the neglect of the forward biassing of the atoms from the slit offsets this to some extent). Comparing these with the observed signals will give some idea of the true dissociation fraction. Also, the size of the observed signal depends on the survival fraction of metastables: the formula 3.26 is a rough estimate. Nevertheless, the values in Table 3.2 give some idea of the feasibility of the 1S–2S excitation. In particular, note how the signal rate for $R = 0.42$ m is drastically improved by lowering the background pressure P_2.

The calculations have been based on a one-way intra-cavity power (power in each beam) of 50 mW—it is a simple matter to scale the results with the square of the laser power as necessary.

The size of the signal to background ratio was an important consideration when estimating the feasibility of the experiment. As will be seen in Chapter 5, 243 nm radiation scattered from the interaction region contributed to the background count rate: the size of which depended on how close the detection region was to the interaction region (ie. the distance R). The background could be be up to several thousands of counts s^{-1}—easily enough to swamp any signal. Under these circumstances it was essential to use the Lyman-α filter. The calculation above does not include the use of the Lyman-α filter—with it in place the signals are reduced by about a factor of three. It was generally not used with the largest values of R because then the scattered UV background was low enough (a few hundred counts s^{-1}) not to be a problem (§4.5).

There turned out to be reasonable agreement between the signal sizes estimated here and those achieved in practice: more details will be given in §5.10. The signal

Table 3.1: Experimental conditions used in the 1S–2S signal estimate.

Quantity		Value
P	One-way intra-cavity laser power	50 mW
Γ	Width of 1S–2S (laser linewidth plus transit time broadening)	$2\pi \times 10^7$ rads^{-1}
w_0	Waist size	100 μm
w	Width of slit in hydrogen nozzle	250 μm
A	Area of slit in hydrogen nozzle	2 mm^2
l	Length of channel in hydrogen nozzle	2 mm
P_1	Pressure in discharge	0.4 Torr
χ	Dissociation fraction	1
ϵ	Detection efficiency (no Lyman-α filter)	10^{-2}
t	Width of detection region	1 cm
d	nozzle–interaction region separation	2 cm
R	nozzle–detection region separation	see Table 3.2
P_2	Pressure in beam chamber	see Table 3.2

Table 3.2: Estimated signal rate S for various beam conditions.

R(m)	P_2(mbar)	S(counts s^{-1})
0.1	4×10^{-5}	9000
0.34	4×10^{-5}	400
0.34	1.2×10^{-5}	2300
0.42	4×10^{-5}	140
0.42	1.2×10^{-5}	1500

size in the early beam work (turbopumped conditions and $R = 0.1$ m) was slightly lower than that in the first entry in Table 3.2 after accounting for the presence of the Lyman-α filter. Table 3.2 overestimates the signal rates for the larger values of R by about an order of magnitude but makes clear the impossibility of performing such experiments without the extra pumping speed of the cryopump (Chapter 5).

Chapter 4

The UV enhancement cavity

4.1 Introduction

In this experiment, the 1S–2S two-photon transition was excited by two counter-propagating beams of 243 nm radiation at the waist of a non-confocal optical cavity. The cavity served a number of functions.

- It produced the two counter-propagating 243 nm beams from a single input beam.
- It allowed the beams to be accurately overlapped.
- It enhanced the UV power available from the laser (ie. the circulating power inside the cavity was larger than that coming out of the laser by a factor of over an order of magnitude.) This enhancement is vital because the two-photon rate is proportional to the square of the incident power.

During the course of the work, two different cavities were constructed—each with a different mirror set. The first version served for preliminary work and, although it was not used for the final experiment, the experience gained in working on it was invaluable when the second cavity was being developed. For this reason, this chapter contains an account of the construction of and difficulties associated with the first version, before going on to describe the one which was actually used.

The development of the enhancement cavity was carried out in parallel with that of the vacuum system. Chapter 5 contains more detail on the vacuum system but a brief outline is given here to put the stages of the work on the enhancement cavity in context.

Originally, the vacuum system consisted of one cubical box mounted directly on top of the turbopump. Both versions of the enhancement cavity were longer than the width of the box and were supported in side-arms on appropriate faces. The sidearms existed before the first cavity, which had therefore to be designed to fit in them. They allowed very little room for vibration isolating padding or mirror

adjustment. The stability of the cavity was badly affected by vibrations from the turbopump and elsewhere in the laboratory. For this reason, the first cavity could only be used for cell mode work, for which the vacuum chamber was pumped by a rotary pump instead of the turbopump (see §3.5 for an explanation of the term "cell mode"). Subsequently, new vacuum flanges with larger sidearms were constructed to hold the second version of the cavity. This made it possible to install more padding between the cavity spacer and the sidearms and made the mirror adjustment easier. At the same time, the design of the vacuum system itself was altered. A second box was connected to the one containing the cavity via a vibration isolating bellows. The turbopump was hung from the second box by another bellows. The much improved isolation of the new cavity meant that it could be used in beam mode as well as cell mode.

The first few sections which follow comprise a theoretical overview of the factors which were considered when designing the cavity. Choices had to made of mirror reflectivities and radii of curvature and the length of the cavity. The next two sections outline the problems of matching the 243 nm beam into the enhancement cavity and reducing the amount of UV being scattered out of it. The mirror holders and servo electronics were common to both cavity designs. These are described before the details of each individual cavity.

4.2 Enhancement factor and mirror reflectivities

The enhancement factor of the cavity is defined as the ratio of the one-way intra-cavity power to the input power. In this experiment we were looking for an enhancement of at least an order of magnitude. In the early stages of the work, there were about 3 mW of 243 nm power available from the laser, which would mean a power in each counter-propagating beam of ~30 mW — adequate for a good two-photon cell mode signal (see §3.7.1). Later, improvements to the frequency doubling system gave an available UV power of 8 mW from the laser. An enhancement of ~10 would give around 80 mW in each beam, which was the level needed for beam mode experiments (§3.7.1).

In the calculations which follow, it is assumed that all the input power is matched into the TEM_{00} mode. We were able to come close to this ideal in practice (see, for example, Fig. 4.8).

Consider a cavity having input and output mirrors with intensity reflection coefficients R_1, R_2, intensity transmission coefficients T_1, T_2 and absorption coefficients A_1, A_2 respectively such that

$$R_i + T_i + A_i = 1 \tag{4.1}$$

where $i = 1, 2$. The A_i account for all loss mechanisms at the mirrors, since for our purposes absorption in the coatings is not distinguishable from scattering from the surfaces or any other significant losses.

The incident electric field is E_i and the incident intensity is I_i. The field in the

cavity in the direction of propagation of E_i is

$$\begin{aligned} E_{ic} &= E_i\sqrt{T_1} + E_i\sqrt{T_1}\sqrt{(R_1R_2)}\exp i\delta + \cdots \\ &= \frac{E_i\sqrt{T_1}}{1-\sqrt{(R_1R_2)}\exp i\delta} \end{aligned} \tag{4.2}$$

where δ is the round trip phase delay. At resonance, the intra-cavity intensity is

$$I_{ic} = I_i \frac{T_1}{[1-\sqrt{R_1R_2}]^2} \tag{4.3}$$

The enhancement factor $\alpha = I_{ic}/I_i$ is therefore

$$\alpha = \frac{T_1}{[1-\sqrt{R_1R_2}]^2} \tag{4.4}$$

and the finesse can be shown to be

$$\mathcal{F} = \frac{\pi\sqrt[4]{R_1R_2}}{1-\sqrt{R_1R_2}} \tag{4.5}$$

In applying these expressions to the enhancement cavities developed in the present work, it is neccessary to take account of the change in properties of the mirrors during use. As described in §4.8, they degraded in the presence of UV radiation while under vacuum. The mirrors could be restored by running the UV in air. However, the effect must be allowed for in choosing the best nominal mirror reflectivities. The degradation was not readily quantifiable except in that it produced a measureable change in enhancement. No measurements on the individual mirrors were possible because only very small regions of the coatings (corresponding to the position of the UV spot for that particular cavity alignment) were affected.

Fortunately, general conclusions can be drawn using fairly crude assumptions. Let us suppose that the losses at the two mirrors are the same ($A_1 = A_2 = A$) and that the degradation causes A to increase at the expense of reflectivity. The transmissions T_1 and T_2 are assumed to remain at their initial values. Now consider the optimum choice of mirror specification.

The simpler case is that of the output mirror. It is clear from equation 4.4 that R_2 should be as high as possible. It was chosen to have $T_2 = 0.01$ in order to have sufficient output intensity for locking the cavity (§4.7). Of course any drop in R_2 during use will reduce the enhancement, but there is no reason why it should not be started off with a high value.

We now turn to the case of the input mirror. The curves in Fig. 4.1 show the dependence of α on the input mirror transmission (T_1) for different values of the loss factor A and with T_2 set to 0.01 in each case. The enhancement factor becomes very large in the case of $A = 0$ (zero losses), but we have to consider the degradation

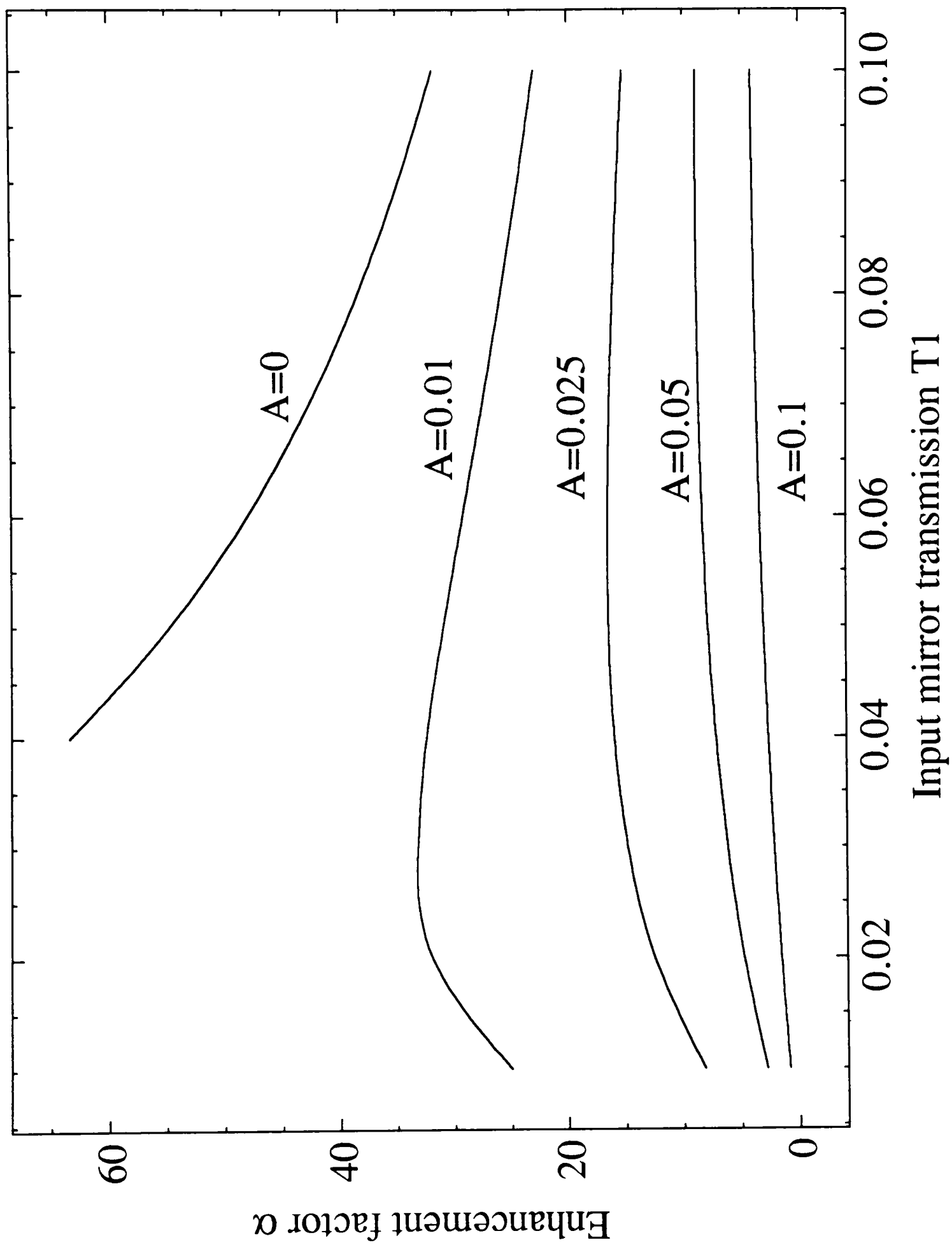


Figure 4.1: Enhancement factor α as a function of input mirror transmission T_1 for different values of the loss factor A.

effect. The curves show the enhancement attainable for losses of up to 10%. It can be seen that, for any A, the enhancement drops off if T_1 is too low. Therefore it is more satisfactory to have T_1 on the high side of optimum where the curves tend to flatten out. We were prepared to sacrifice the possibility of very high enhancement in the interests of keeping it at about the level of 10 or greater even with losses of a few percent. Therefore, input mirror transmissions of around 5% were chosen.

The transmissions and reflectivities of the mirrors actually used, together with the achieved enhancement factors, will be detailed below.

4.3 Mode structure and cavity geometry

A Gaussian beam can be trapped between two curved mirrors if the radii of curvature of the mirrors match those of the wavefronts at the positions of the mirrors, provided that the spot size on the mirrors is small compared to their size. In the particular case of a symmetric, non-confocal cavity (ie. one in which the mirrors have the same radius of curvature R and are separated by a distance $d \neq R$) the position of the beam waist is at the centre of the cavity. The waist size (w_0) is given by [43, 44]

$$w_0^2 = \frac{\lambda}{2\pi}\sqrt{[d(2R-d)]} \tag{4.6}$$

and the spot size on the mirrors (w_m) by

$$w_m^2 = \frac{\lambda R}{\pi}\left\{\frac{2R}{d} - 1\right\}^{-1/2} \tag{4.7}$$

where λ is the wavelength of the beam.

The frequency separation of the fundamental (TEM_{00}) resonant modes of the cavity is

$$\nu_{q+1} - \nu_q = \frac{c}{2d} \tag{4.8}$$

and the separation of adjacent higher order TEM_{lm} modes of a given order q is

$$\Delta\nu = \frac{c}{2d}\frac{2}{\pi}\arctan\left(\frac{d}{2b}\right) \tag{4.9}$$

where b is the confocal parameter and is related to the waist size w_0 by

$$b = \frac{\pi w_0^2}{\lambda}. \tag{4.10}$$

The UV enhancement cavity was designed to be non-confocal so that the position of the waist would be fixed at the centre of the cavity and the mode structure could easily be assessed. There is some theoretical advantage in using a confocal cavity since the higher symmetric modes coincide and lead to a higher intensity, but the

loss of control over the beam waist size and position offsets this. In addition, exact confocality is difficult to arrange. The arrangement chosen has well-separated modes so that laser frequency jitter and acoustic shocks are less likely to throw the cavity off lock on the fundamental mode and on to a lower power transverse mode. The waist size was chosen to be around 100 μm in order to give an adequate two-photon excitation rate without excessive transit time broadening (§3.7.1).

4.4 Mode-matching the UV beam

BBO produces a very large walk-off in the generated second harmonic beam. In our experiment, the 243 nm beam emerged from the crystal with an aspect ratio of approximately 20:1. In the elongated direction, the beam profile was almost rectangular whereas in the other direction it was Gaussian. A system of lenses matched this distorted beam to the waist at the centre of the UV enhancement cavity, thereby coupling as much power as possible into the fundamental mode. By calculating the overlap integral of a rectangular profile of width w and a Gaussian with a 1/e full width also equal to w, Boshier [21] calculated that the maximum possible coupling efficiency is approximately 88%.

The general outline of the mode-matching scheme was as follows. The 243 nm beam passed first through a converging lens which formed a waist of a certain size in the non-walkoff direction. Next, a cylindrical lens produced, in the walk-off direction, a waist of the same size and in the same position as the aforementioned waist in the non-walkoff direction. The cylindrical lens was orientated so that it only affected the walk-off direction. These two lenses produced an almost circular spot at a certain distance from the laser. A third, spherical, lens matched this waist to that at the centre of the UV cavity. All the lenses were of fused silica (Spectrosil B).

The positions of the lenses and waists, waist sizes and optical path length were calculated using the $ABCD$ law (see, for example, [43, 44]) starting from a knowledge of the beam characteristics in the BBO crystal. It should be noted that in some instances the UV cavity input mirror acted as a lens for the 243 nm beam.

The mode-matching layout for each version of the cavity is detailed later. The lens focal lengths and separations are not exactly the same as the values yielded by the $ABCD$ analysis, for several reasons. The focal lengths of the silica lenses were known for visible light and estimated (on the basis of refractive index data) to be approximately 10% shorter in the UV. In addition, there were usually only standard focal length lenses available. The $ABCD$ results were used to position the optics roughly correctly. Small adjustments in positioning were then made to optimise the mode matching as described later in this chapter.

4.5 Reduction of the UV background

The photomultiplier (EMI G26L314LF) used to detect the Lyman-α fluorescence from the excited atoms was of the solar blind type and, in the early stages of the work, had over its input window a Lyman-α filter with a transmission of 23% at 121.6 nm (§3.7.3). It had a small (~0.01%) quantum efficiency at 243 nm (compared to 10% at 121.6 nm). Nevertheless, it was found that 243 nm light scattered from the enhancement cavity could easily swamp any 1S–2S signal if suitable precautions were not taken. The problem was even more severe when the photomultiplier was moved away from the interaction region for beam experiments and the Lyman-α filter removed to improve the detection efficiency.

To reduce the scattered UV background, a series of baffles with small central holes (a few millimetres in diameter) were installed along the axis of the cavity. Different types of baffle were used for each version of the cavity: details of their design and effectiveness are given below.

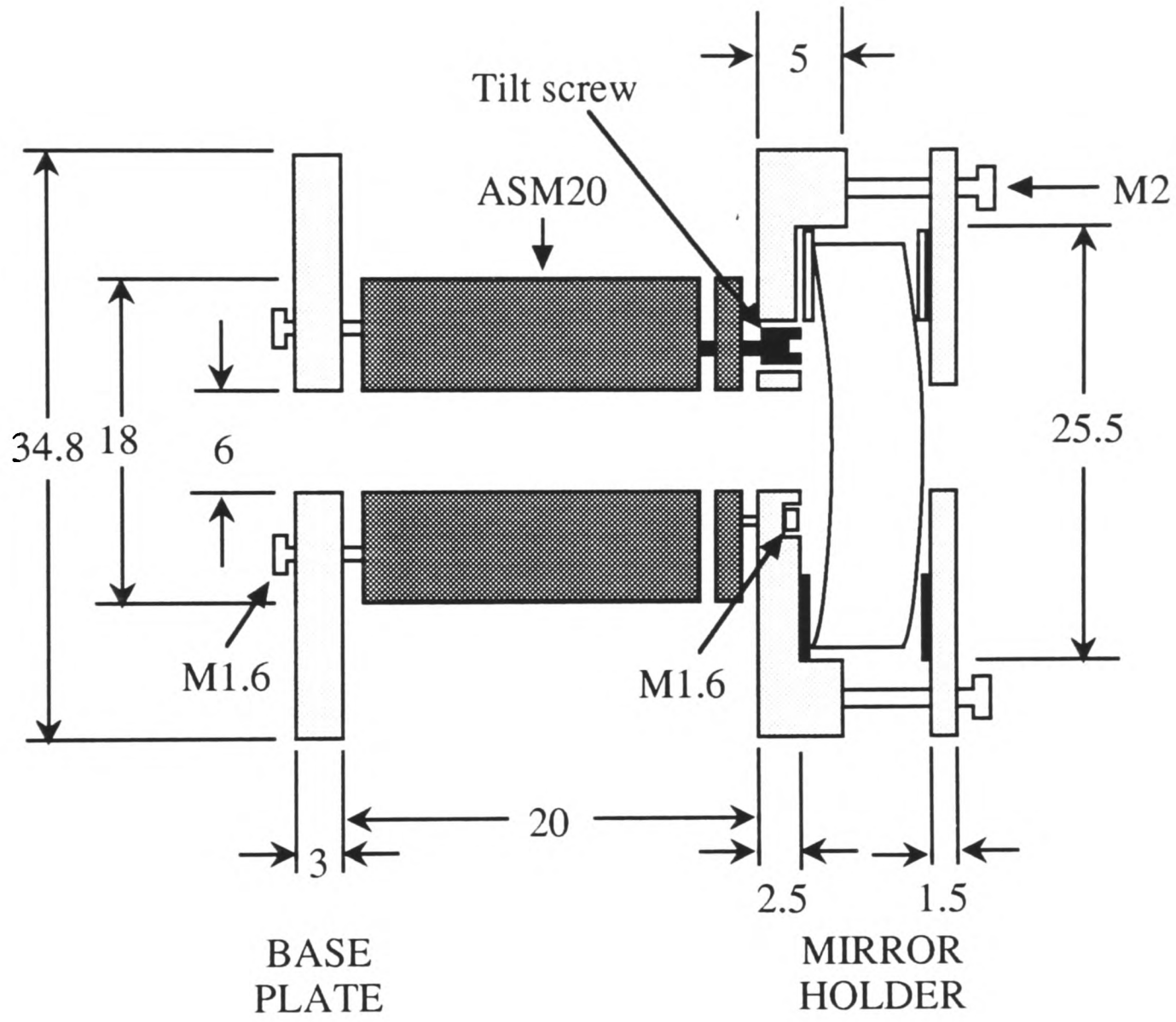
4.6 Mirror holders

In both versions of the cavity, one of the mirrors was mounted on a piezo-controlled mirror mount (Photon Control ASM20) to enable the cavity length to be dithered as described below. The piezo was mounted on a Dural disc which was attached to one end of the cavity spacer. Three tilt screws on the piezo allowed manual adjustment of the mirror alignment. This was straightforward if a small (~8 mm diameter) mirror was mounted on the piezo, but we also used it with a 25 mm diameter mirror. A Dural mount (Fig. 4.2) was constructed to hold such a mirror on the piezo, but unfortunately this meant that the tilt screws were inaccessible and other means had to be used to adjust the mirror alignment. The main design criterion for this mount was that it had to be as light as possible so as not to slow the response of the piezo excessively.

The other mirror was always one of 25 mm diameter and was also held in a Dural mount (Fig. 4.3). The mount was attached to the base plate by three fine thread (80 tpi) brass screws plus springs, which were used for tilt adjustment.

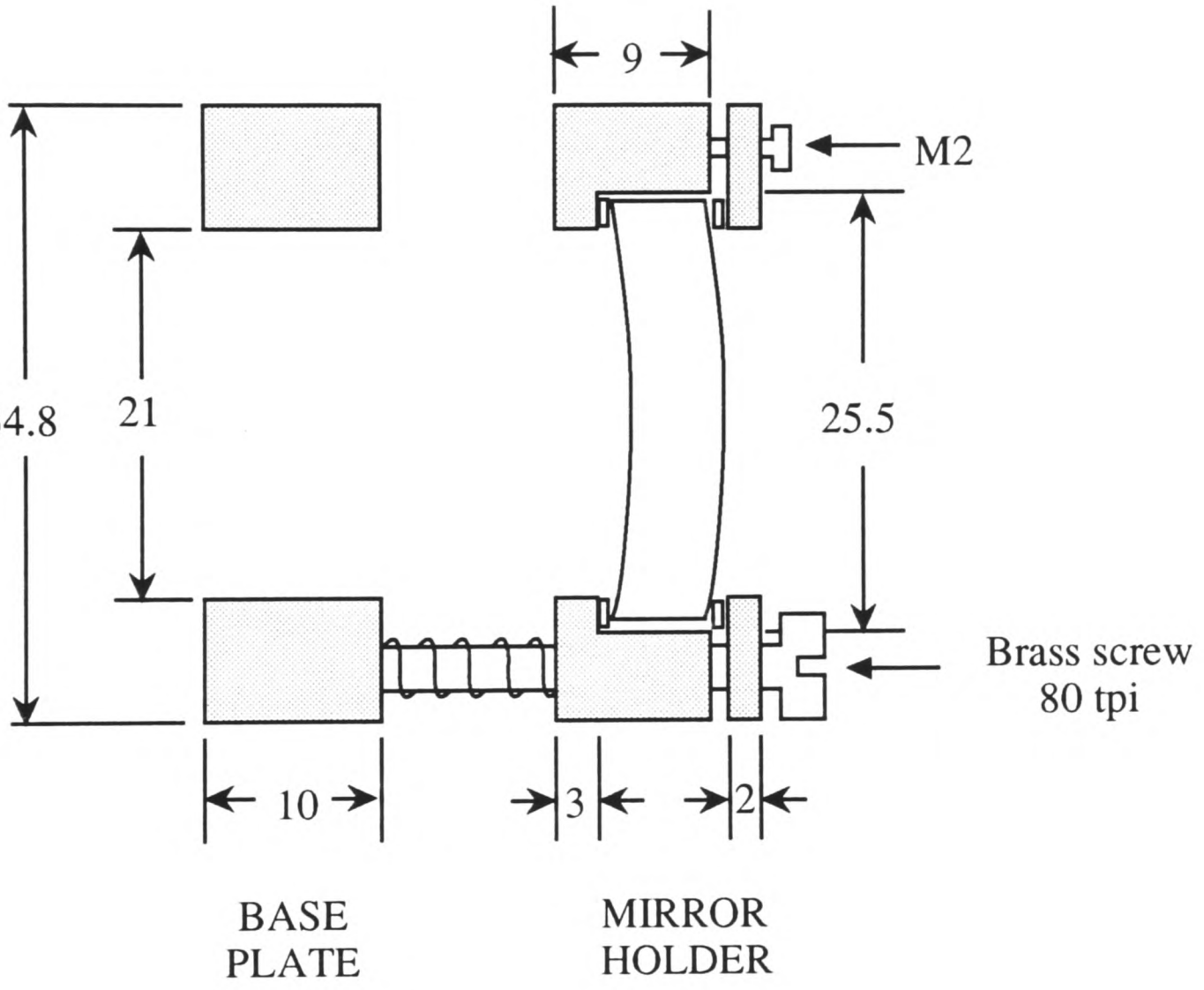
4.7 The servo system

The ASM20 mirror mount had three independent (X,Y,Z) piezo stacks. The cavity length was dithered by driving all three stacks with the same 11 kHz sinusoidal voltage. A photodiode monitored the output UV intensity from the cavity to provide an error signal for locking. A phase-sensitive detection technique was used to lock the cavity to the peak of the fundamental mode (Fig. 4.4). When the cavity was locked, the intensity falling on the photodiode was roughly constant but with fast amplitude



Dimensions in mm

Figure 4.2: Mirror holder used with the ASM20 piezo controlled mirror mount.



Dimensions in mm

Figure 4.3: Mirror holder with brass tilt screws.

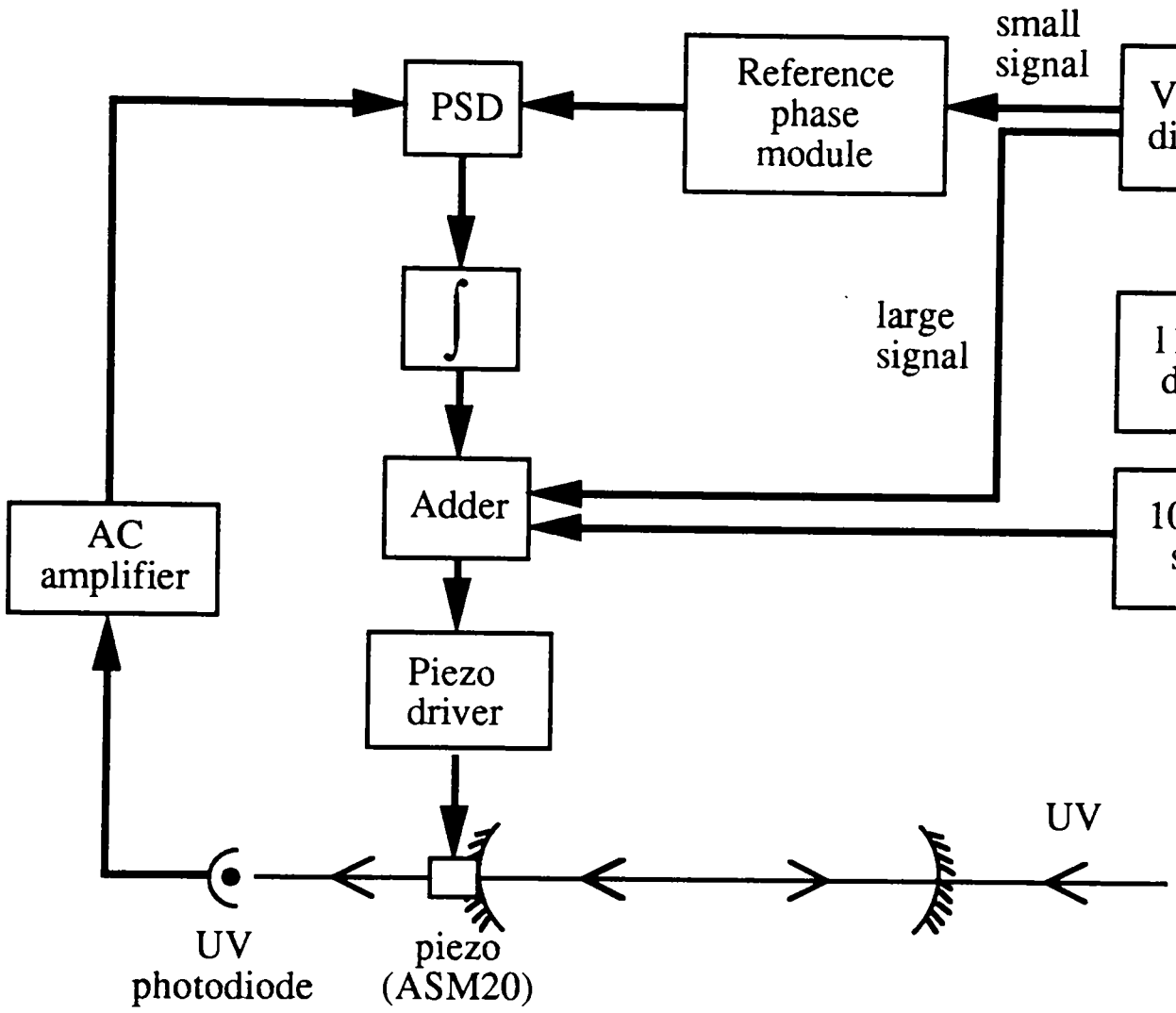


Figure 4.4: The servo electronics.

modulations as the dither took the cavity slightly off resonance on either side of the peak transmission. As the effect of this was to reduce the average intra-cavity power, the amplitude of the dither was always made as small as possible consistent with giving a reliable lock. Under some conditions (§4.8) vibrations arising from the vacuum pumps caused large amplitude modulations and could even throw the cavity off lock completely.

The cavity could be scanned slowly with a 100 Hz sinusoidal voltage in order to display the mode structure on an oscilloscope. Under these conditions, the locking system of Fig. 4.4 was disabled.

4.8 The 30 cm brass cavity

The first UV enhancement cavity to be constructed was approximately 30 cm long with 40 cm radius of curvature (RoC) mirrors. The spacer was made from a length of 38 mm OD, 35 mm ID brass tube. The size of the tube was chosen to allow it to fit into the sidearms of the vacuum can, which at that stage were constructed from KF40 welding flanges (40 mm ID). A rubber O-ring in a groove around the exterior of the tube near each end made a snug fit in the sidearms and provided some degree of vibration isolation (Fig. 4.5).

The 40 cm RoC mirrors were made by Tecoptics and had nominal reflectivities of 99.5% and 96.5% at 243 nm. There were each 25 mm in diameter and 6 mm thick. The substrates were of silica, zero power but wedged with an anti-reflection coating for 243 nm on the back surface.

The high reflector (output mirror) was mounted on the piezo-controlled mirror mount as described in §4.6 and shown in Fig. 4.2. The base plate was inserted a few millimetres into the end of the brass tube and held in place with two grub screws. The medium reflector (input mirror) was held in the other Dural mount (Fig. 4.3) The original plan was to use the fine thread brass screws for tilt adjustment, but have the mount sufficiently far into the end of the brass tube so that not only the base plate, but also the mirror holder itself would be fixed with grub screws. This extra clamping was found to be necessary to prevent the mirror wobbling because of pump vibrations. However, this idea had to be abandoned when it was found that, because the ID of the brass tube was only a few millimetres larger than the OD of the mirror holder, there was insufficient space for it to be tilted.

A crude but effective alternative was to dispense with the tilt screws and base plate altogether, and fasten the mirror holder itself into the brass tube with grub screws. A limited amount of tilt adjustment was available by loosening the grub screws slightly, tilting the mirror holder by hand and then tightening the grub screws to hold it in place. The same technique was employed to adjust the tilt of the high reflector on the piezo since its own tilt screws were inaccessible. The initial mirror alignment was performed with the aid of a helium-neon laser. The HeNe beam was directed through the cavity in the opposite direction to the UV beam, entering and

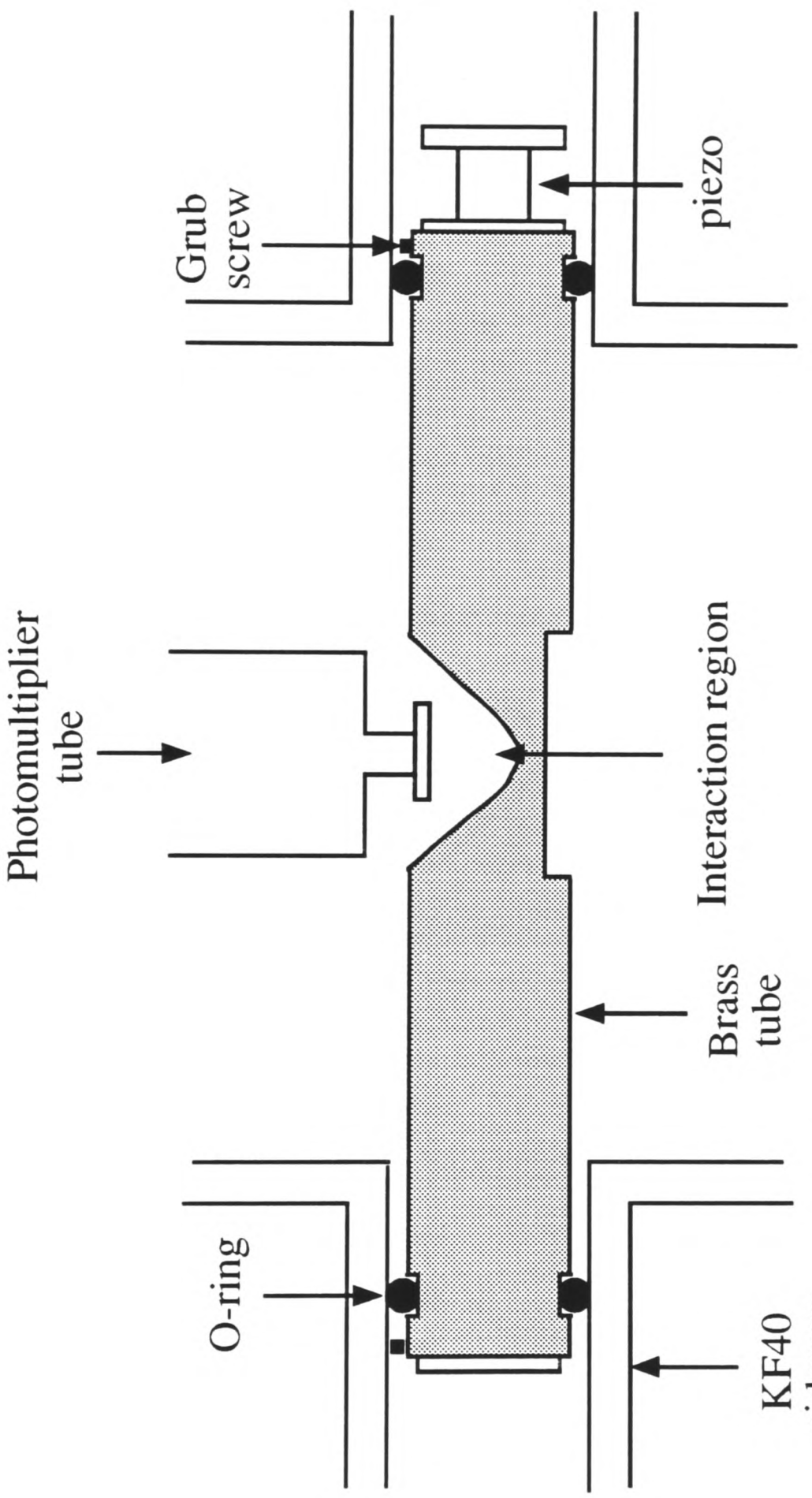


Figure 4.5: The 30 cm brass cavity.

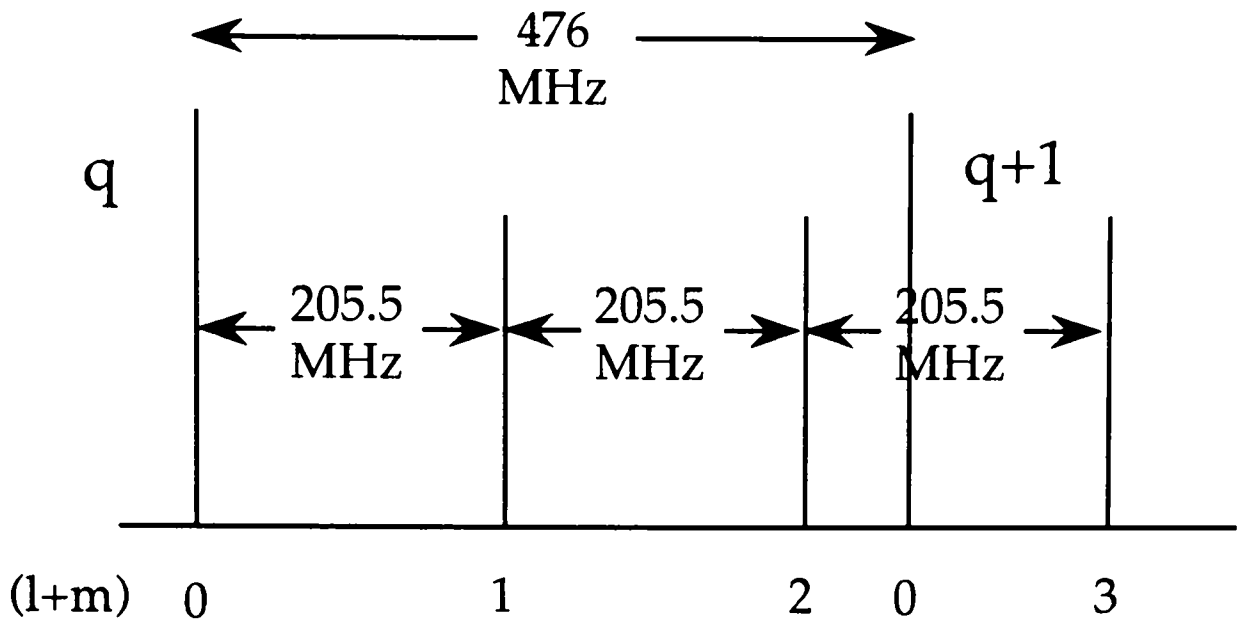


Figure 4.6: Predicted mode structure of the 30 cm cavity.

leaving the cavity through the centres of the mirrors. The tilt of each mirror was then adjusted to send the HeNe spots from the *reflecting* surfaces back along the incoming beam. When the alignment was correct, a back-reflected circular fringe pattern could be seen centred on the HeNe beam. This procedure ensured that the mirrors were parallel and defined the axis of the cavity along a line joining the centres of the mirrors. It could be rather tricky to perform, but, once the grub screws were tightened, the mirror holder was held so firmly that the entire cavity could be moved about, inserted into and removed from the vacuum can without destroying the mirror alignment.

The total length of the cavity was 31.5 cm. With 40 cm RoC mirrors equations 4.6, 4.7, 4.8, 4.9 give the following:

- Beam waist $w_0 = 123\,\mu\text{m}$
- Spot size on mirrors $w_m = 158\,\mu\text{m}$
- Order separation $\nu_{q+1} - \nu_q = 476\,\text{MHz}$
- Transverse mode separation $\Delta\nu = 0.432 \times 476\,\text{MHz} = 205.5\,\text{MHz}$

The predicted mode structure is shown in Fig. 4.6. Note that the first few transverse modes are well separated from the fundamental mode.

The system of lenses used to mode match the 243 nm light into the TEM_{00} mode of the cavity is shown in Fig. 4.7. Distances are measured from the output coupler (O) of the laser. In the absence of the cylindrical lens C (focal length 10 cm in the visible), the beam in the walkoff direction would be focussed to a waist smaller than 127 μm and closer to O than that shown. C produces a circular spot at 590 mm from O , and this is matched by the spherical lens L (focal length 30 cm in the visible)

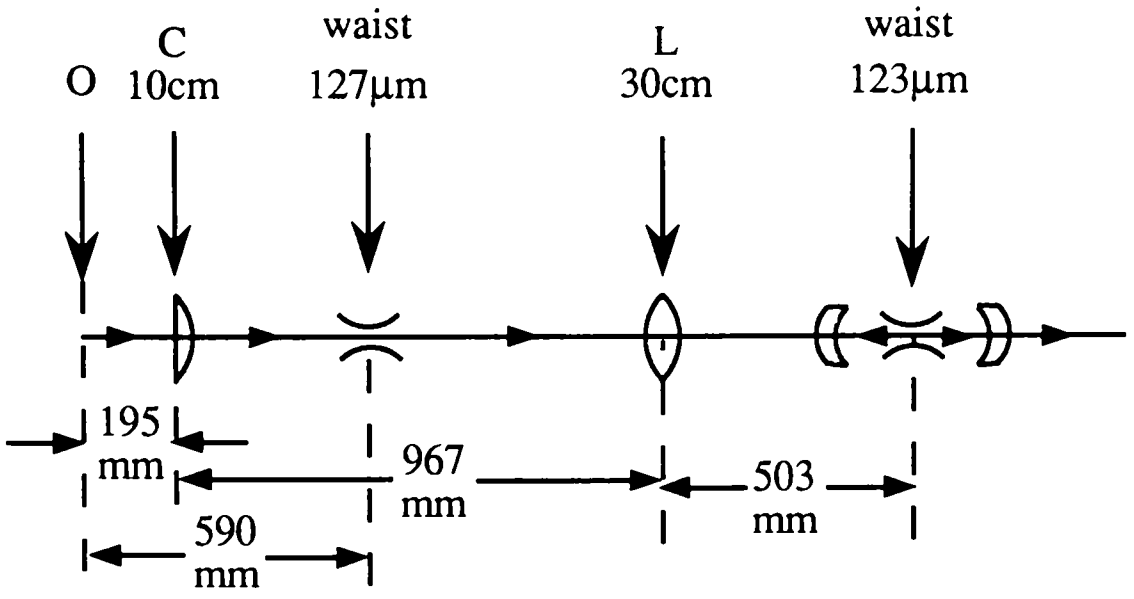


Figure 4.7: Mode matching layout for the 30 cm cavity with 40 cm mirrors.

to the 123 μm waist at the centre of the cavity. In this case the input mirror was zero power. The UV beam was matched into the cavity by directing it back along the HeNe alignment beam. The mode structure was displayed on an oscilloscope and adjustments made to the steering mirrors to maximise the power in the TEM_{00} mode.

The mode matching achieved with this system is shown in Fig. 4.8. We estimated the mode matching efficiency (ie. the fraction of the total UV power which is matched into the fundamental mode) to be approximately 80%.

The transmission curve for each mirror was obtained using a Perkin-Elmer spectrophotometer. At 243 nm the transmissions were found to be 5.11% and 0.93%. Using these values, the very best possible enhancement (ie. with zero loss in the cavity) is found from equation 4.4 to be 55. With a mode-matching efficiency of around 80%, this maximum possible enhancement drops to 44.

In practice, the enhancement was determined by measuring, with the *same* photodiode, the UV power entering and leaving the cavity. The UV photodiode had been calibrated against a power meter (a signal of 3 V corresponding to 2 mW). The transmission of the output mirror was known so the one-way intra-cavity power could be calculated. The ratio of this power to the input power gave the enhancement factor α.

This mirror set gave an enhancement factor of 18 in air. The corresponding finesse was estimated (from the 'scope display) to be 50. From the formulae of §4.2 and the curves in Fig. 4.1 we find that with $T_1 = 0.05$ and 80% mode matching efficiency, an enhancement of 18 is consistent with a finesse of about 60 and a loss of around 1.5%.

The above figures all apply to the enhancement and finesse measured in air. However, as remarked earlier, we observed that if the 243 nm beam was matched into the cavity when it was under vacuum, there would be an appreciable drop in enhancement and finesse over time. The rate of degradation increased with circulating UV power

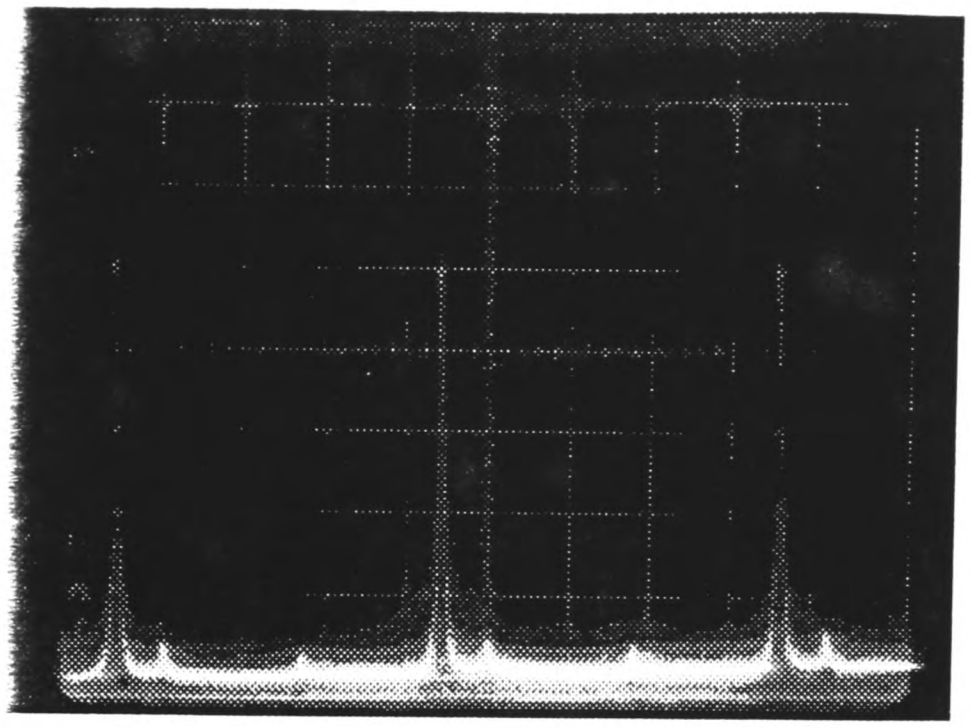


Figure 4.8: The mode structure of the 30 cm cavity.

and could be quite fast when the cavity was locked to the 243 nm light (thereby increasing the average intra-cavity power). With the cavity locked and 1–2 mW input power, the enhancement could drop from 18 to around 1 in less than 15 minutes. Hardly any degradation was observed if the cavity was merely placed under vacuum with no circulating UV. Fig. 4.9 illustrates the rate of degradation under various conditions. There was no *permanent* damage to the mirror coatings—no marks could be found on the surfaces and, more significantly, a complete recovery could be effected by locking the cavity to the UV in air for a few minutes. Very little recovery resulted from leaving the mirrors in air for a period (eg. overnight) without the UV.

It seemed at first that this phenomenon would render the experiment impossible. However, it became apparent that in the presence of *atomic* hydrogen, the rate of degradation was significantly slowed. Indeed, during early cell mode experiments the degradation was slow enough not to present a problem. It should be noted that the presence of atomic hydrogen did not recover the enhancement (even with the UV on) but did inhibit any further change. Also, flowing *molecular* hydrogen through the system had little effect.

This design of cavity proved to be very susceptible to vibrations from the turbopump (or the rotary pump in the case of cell mode work). It was isolated from the vacuum can by only a single thickness of rubber O-ring and its construction (from brass tube) meant that it was fairly light. In addition, the response of the piezo was slowed by the large mirror mounted on it. A set of small (8 mm diameter) 40 cm RoC. 93% reflectors were obtained for use with the piezo, but these turned out to suffer permanent damage on exposure to the 243 nm beam and were therefore unusable.

The problems arising from vibrations from the turbopump were addressed when

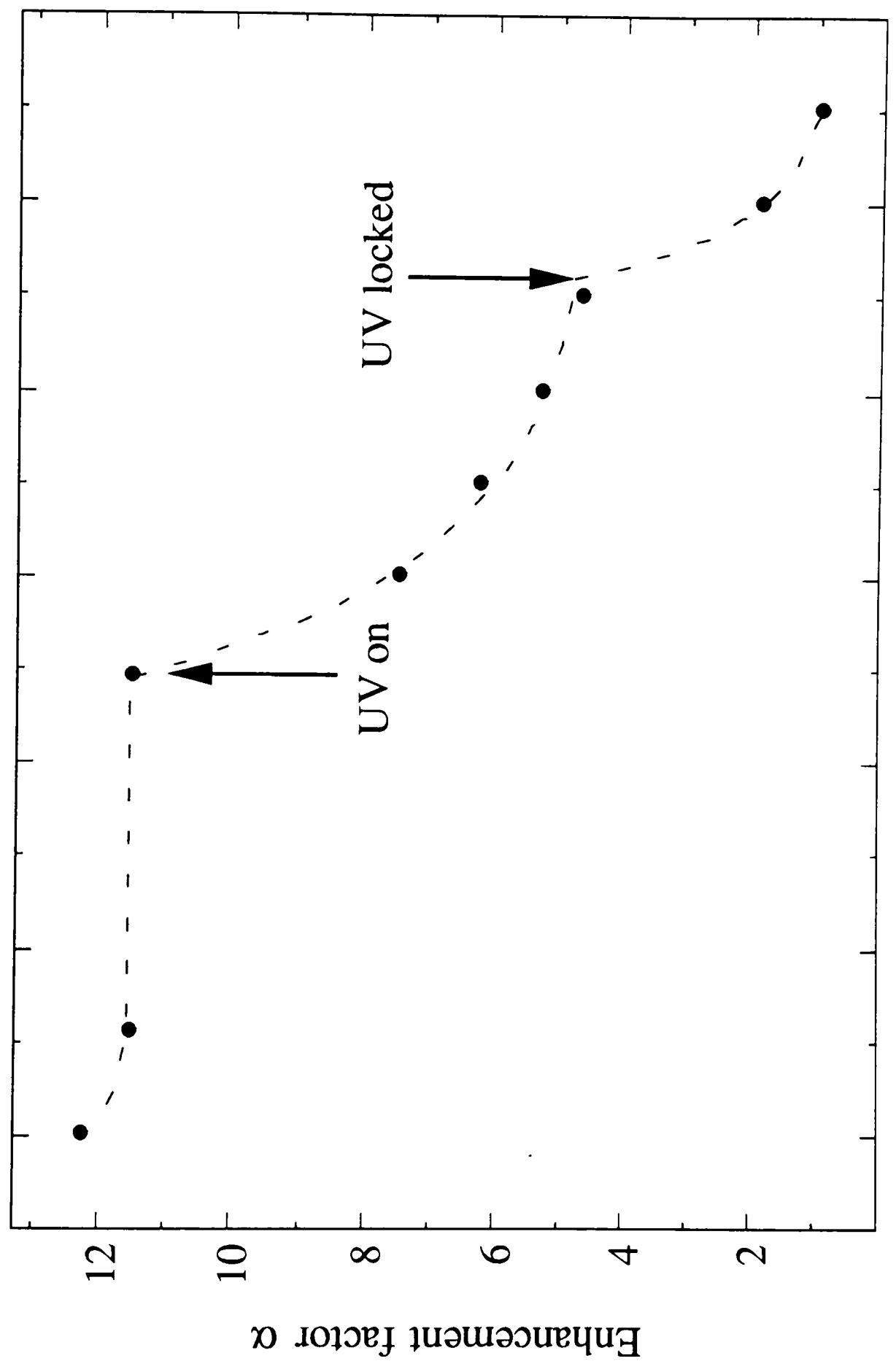


Figure 4.9: Enhancement degradation over time with no UV in the cavity, with UV in the unlocked cavity and with the cavity locked to the UV.

the next version of the enhancement cavity was being designed. The first cavity as described above was used for preliminary cell mode experiments. For this purpose, the chamber was pumped with a rotary pump. The rubber line connecting the pump to the chamber was laid along the floor and weighted down in order to damp the vibrations.

During cell mode experiments, the photomultiplier (with Lyman-α filter in place over the input window) was positioned directly above the interaction region in order to detect the Lyman-α fluorescence from collisionally quenched 2S atoms. Two large holes were cut in the brass tube, above and below the interaction region (Fig. 4.5). The upper one allowed the photomultiplier to see into the interaction region. The purpose of the lower one (directly opposite the photomultiplier window) was to ensure that the photomultiplier was not looking directly at a nearby metal surface which would be a source of scattered 243 nm background (§4.5).

These measures alone were not sufficient to reduce the UV background to an acceptable level for cell mode experiments so a system of baffles was installed in the cavity. Two sets of three baffles were inserted into the brass tube—one on either side of the interaction region. They were constructed from copper discs spaced along three lengths of threaded rod and had central holes of 4 mm, 7 mm and 4 mm in that order. Subsequently an extra baffle with a 4 mm hole was added on each side next to the interaction region. The baffles were held in place with Torrseal and painted with Aquadag.

Further baffling was ultimately provided by 4 strips of copper foil with 2 mm holes, which could be inserted into slots cut in the brass tube. The strips were slightly curved along their length so that they were held firmly in the slots. These baffles were designed to be installed after the cavity mirror alignment had been done—the very small axial holes would have made this procedure even more difficult.

This system of baffles reduced the background count rate from scattered 243 nm photons to around 50 counts s^{-1} per milliwatt of intracavity power in cell mode. With an intra-cavity power of 30 mW this meant a background of $\sim$ 1500 counts s^{-1}. As cell mode signals under these conditions were several thousand counts s^{-1}, this background level was not a problem.

4.9 The 40 cm Dural cavity

The main reason for abandoning the first enhancement cavity and developing a new one was to reduce the sensitivity of the cavity to vibrations. As pointed out earlier, the existing KF40 sidearms did not permit the use of extra padding and rendered the mirror adjustments extremely awkward. New flanges with ISO63 sidearms (internal diameter 70 mm) were therefore constructed to hold a larger, heavier cavity spacer, while still allowing for much thicker vibration isolating padding and easier mirror adjustments. The construction of the new cavity also allowed us to try a different mirror set. The situation which existed regarding the degradation of enhancement in

vacuum was clearly unsatisfactory.

The new cavity had the following dimensions. The spacer was an approximately 40 cm long section of 2" diameter Dural rod, with a 1/2" axial hole. Circular holes of diameter 35 mm were cut above and below the interaction region as before so that the cavity could be used in cell mode if need be. 20 mm×40 mm holes on either side allowed the atomic hydrogen to enter and leave the interaction region. Four 3/4" holes were bored through the spacer transversely to accommodate a new design of baffle (Fig. 4.10).

The first mirror set used with this cavity were made by the Acton Corporation (the company which supplied the mirrors used in the previous Oxford 1S–2S experiment [21]) and had radii of curvature of 30 cm. A number of 25 mm diameter high reflectors (>99%) were available. Unfortunately, the only corresponding medium reflector (the one which was actually used in that work) had a soft coating which had been partially removed by cleaning. However, one part of the coating appeared to be undamaged (Fig. 4.11). The mirror was covered in a protective wax coating and the undamaged section was sawn off by the Clarendon Laboratory glassblower. We were able to mount this section on to an ASM20 piezo-controlled mirror mount as shown (Fig. 4.11), leaving the tilt screws accessible.

The piezo with the mirror fragment was attached to a Dural base plate as before. The base plate was bolted directly on to the end of the Dural rod forming the cavity spacer. The high reflector was held in the mirror holder illustrated in Fig. 4.3, the base plate of which was also attached to the end of the Dural rod.

The total cavity length (d) including mirror mounts was 42 cm. With 30 cm mirrors, equations 4.6, 4.7, 4.8, 4.9 give the following:

- Beam waist $w_0 = 103\,\mu\text{m}$
- Spot size on mirrors $w_m = 188\,\mu\text{m}$
- Order separation $\nu_{q+1} - \nu_q = 357\,\text{MHz}$
- Transverse mode separation $\Delta\nu = 0.632 \times 357\,\text{MHz} = 226\,\text{MHz}$

The predicted mode structure is shown in Fig. 4.12.

The mirror alignment was carried out essentially as described in §4.8, with tilt adjustment for the medium reflector being provided by the piezo tilt screws and for the high reflector by the brass screws. The layout of the mode matching optics had to be altered to take account of the new cavity length and waist size as well as the fact that the new input mirror was plano-concave and acted as a lens on the 243 nm beam. The layout used in practice is shown in Fig. 4.13.

Later in the work, changes were made to the frequency doubling system which resulted in the UV beam exiting the laser from the side and not through the output coupler as before (§5.6). The mode matching scheme was changed to take account of this (Fig. 4.14). The starting point for the $ABCD$ calculation was at the exit face

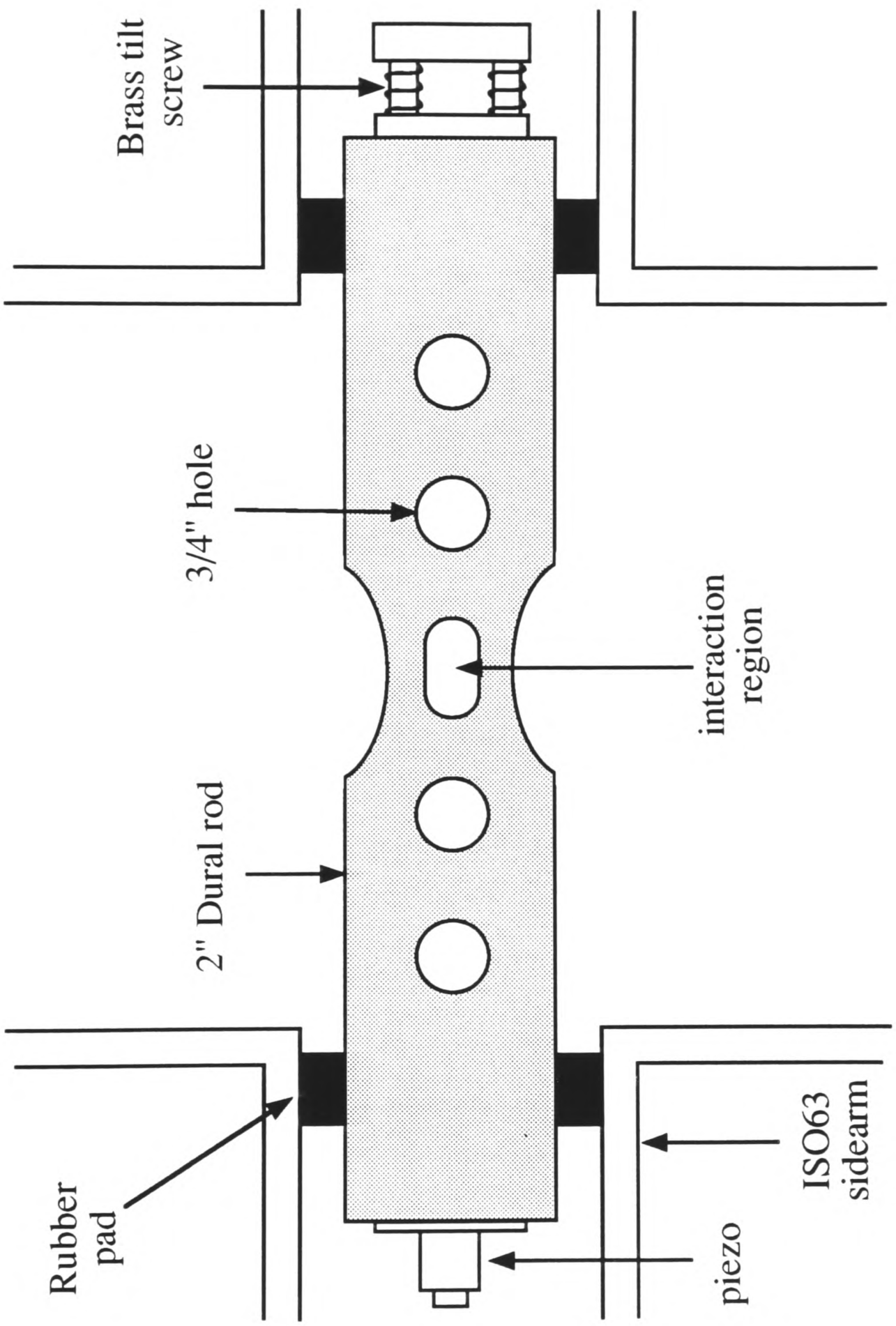


Figure 4.10: The 40 cm Dural cavity.

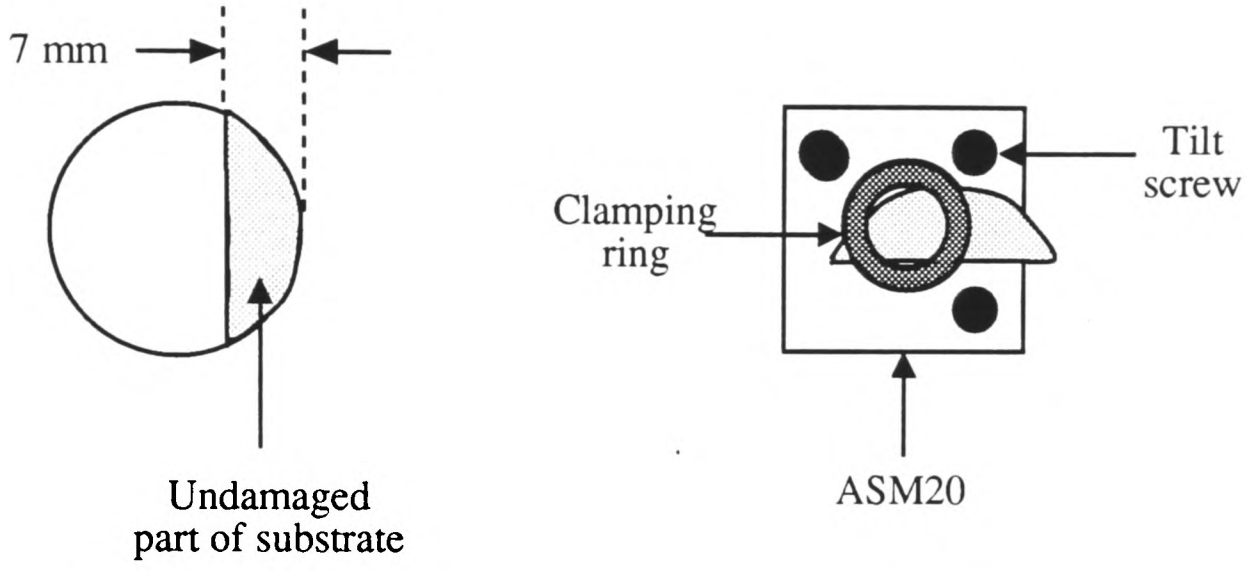


Figure 4.11: The undamaged section of the Acton 30 cm medium reflector.

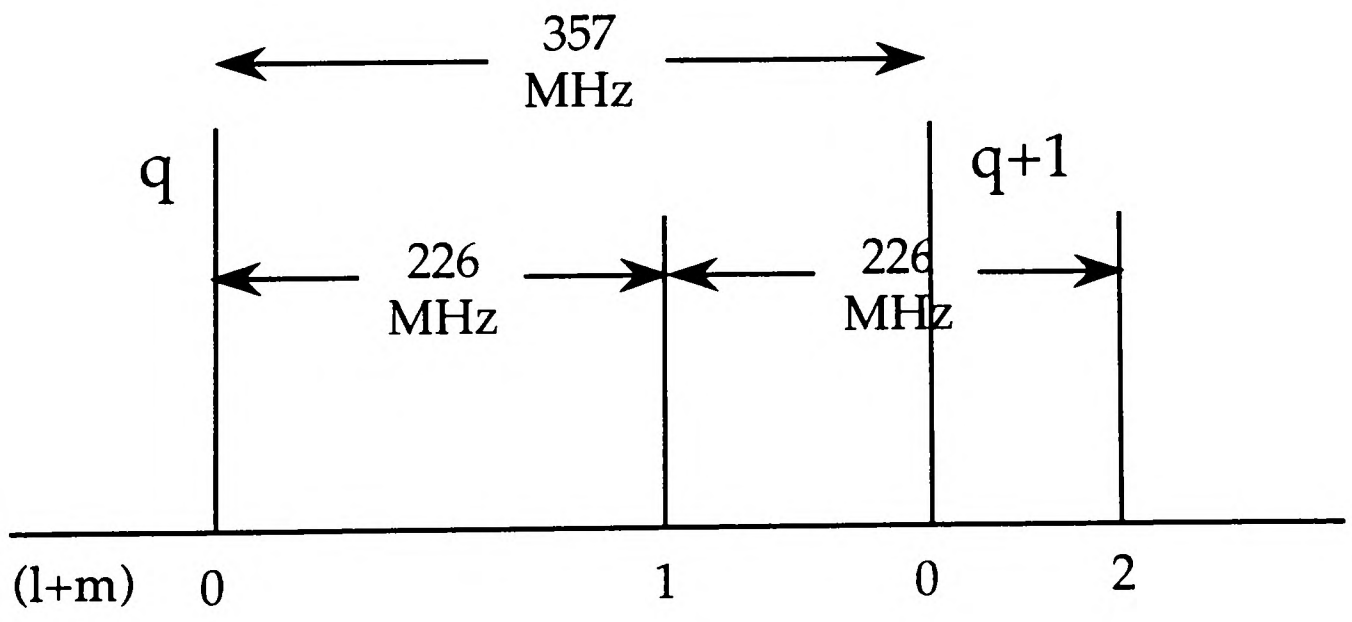


Figure 4.12: The predicted mode structure of the 40 cm cavity.

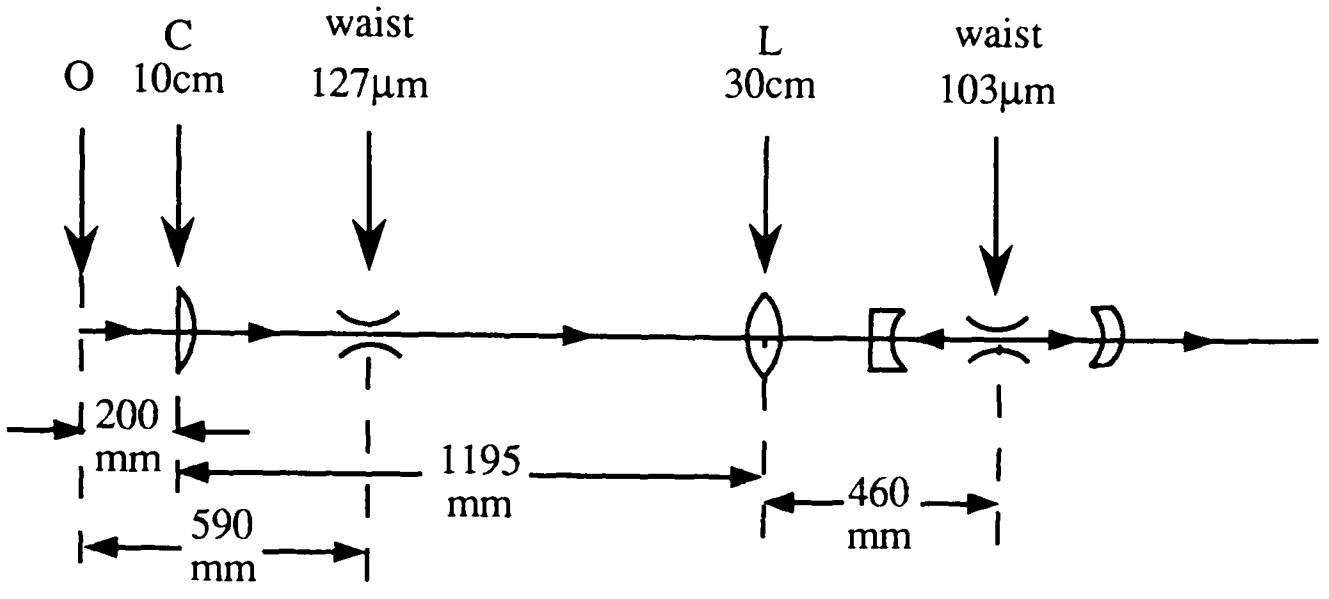


Figure 4.13: The mode matching layout for the 40 cm cavity.

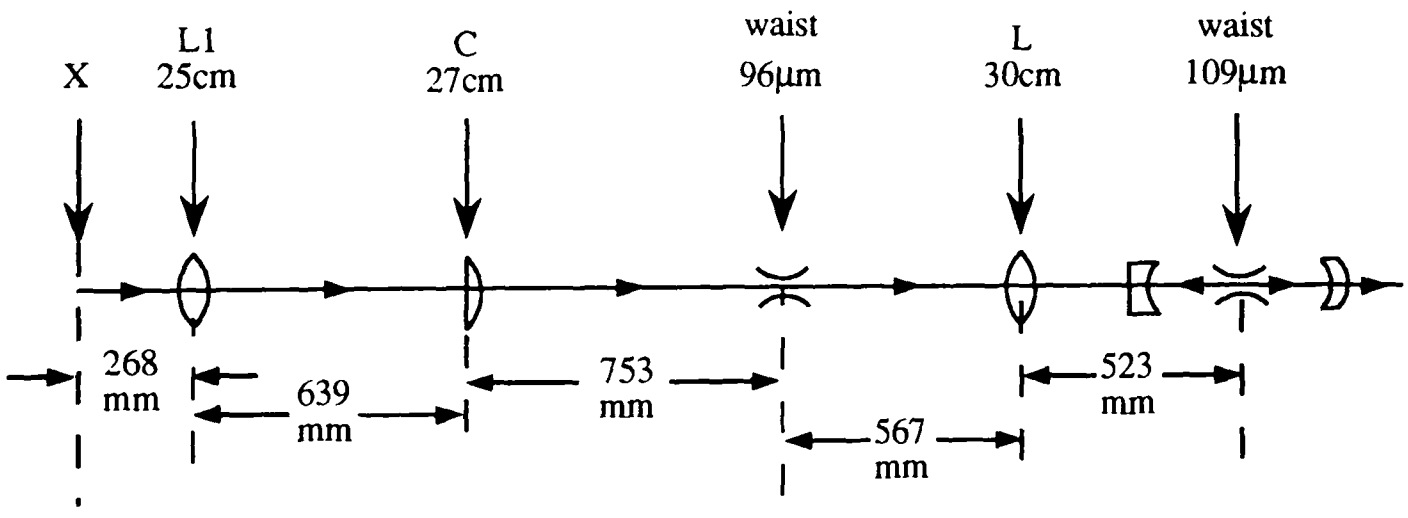


Figure 4.14: Mode matching layout for the 40 cm cavity with modified UV beam.

of the BBO crystal, marked as X in the diagram. The most important difference is the inclusion of the lens L1 which takes on the role of forming the first waist in the non-walkoff direction.

The mirror reflectivities were taken to be 99% and 95% at 243 nm. The mode-matching efficiency was similar to that achieved with the previous cavity, ie. better than about 80%. The theoretical best possible enhancement is therefore 44 as before. In practice, the enhancement factor for the new cavity was measured to be approximately 13 in air. This figure is consistent with a loss (A) of around 2.5% (from Fig. 4.1 and equation 14.4). It turned out that these mirrors also suffered degradation in vacuum in the presence of the 243 nm radiation. Once again, atomic hydrogen appeared to inhibit the process. This cavity was mainly used for beam mode experiments, in which degradation was slightly more of a problem than in cell mode—presumably because of the lower atom density around the mirrors. If the vacuum chamber was being cryopumped (as it was for the final experiment), the enhancement factor would drop from its normal value of around 13 to about 9 over a couple of days of running. Locking the cavity in air to a few milliwatts of UV for 20 minutes or so effected a complete recovery.

The new cavity was very insensitive to turbopump vibrations. Around the spacer in each sidearm were three rubber pads, each about 1 cm thick, which provided good vibration isolation. In addition, the cavity was much heavier than the previous version and the turbopump had by this stage been doubly decoupled from the box containing the cavity (see introduction to this chapter and §5.2).

A different design of 243 nm baffle was used for this cavity. The experience gained with the old cavity had led to the view that baffles which could be inserted *after* the cavity had been aligned were superior to permanently fixed ones, because the very small (~2 mm) apertures (which were required to reduce the scattering adequately) made preliminary alignment extremely difficult. However, non-permanent baffles had to be easy to insert and remove with the cavity already installed in the vacuum can. Also, once in place, they should be held firmly enough not to be dislodged if accidentally knocked. These requirements were satisfied by the following design.

The baffles were constructed from 8 cm lengths of 3/4" thin wall brass tube. A small hole (2 mm or 4 mm in diameter) was drilled into the wall of the tube as shown in Fig. 4.15. Opposite to this was a larger (7 mm) hole. The interior was painted with Aquadag. Once the cavity had been aligned, the baffles were inserted into the 3/4" holes in the spacer and moved around until the UV beam passed cleanly through the small hole. Each baffle was slit along its length so that it could be opened out slightly to make a fairly tight fit in the 3/4" holes. There were two baffles on either side of the interaction region: one each with 2 mm and 4 mm holes. The larger hole was closer to the interaction region.

This cavity was primarily used for beam mode work with the photomultiplier in the second vacuum can and the Lyman-α filter removed. It was found that, under these conditions, the baffles prevented a large amount of scattered UV coming from

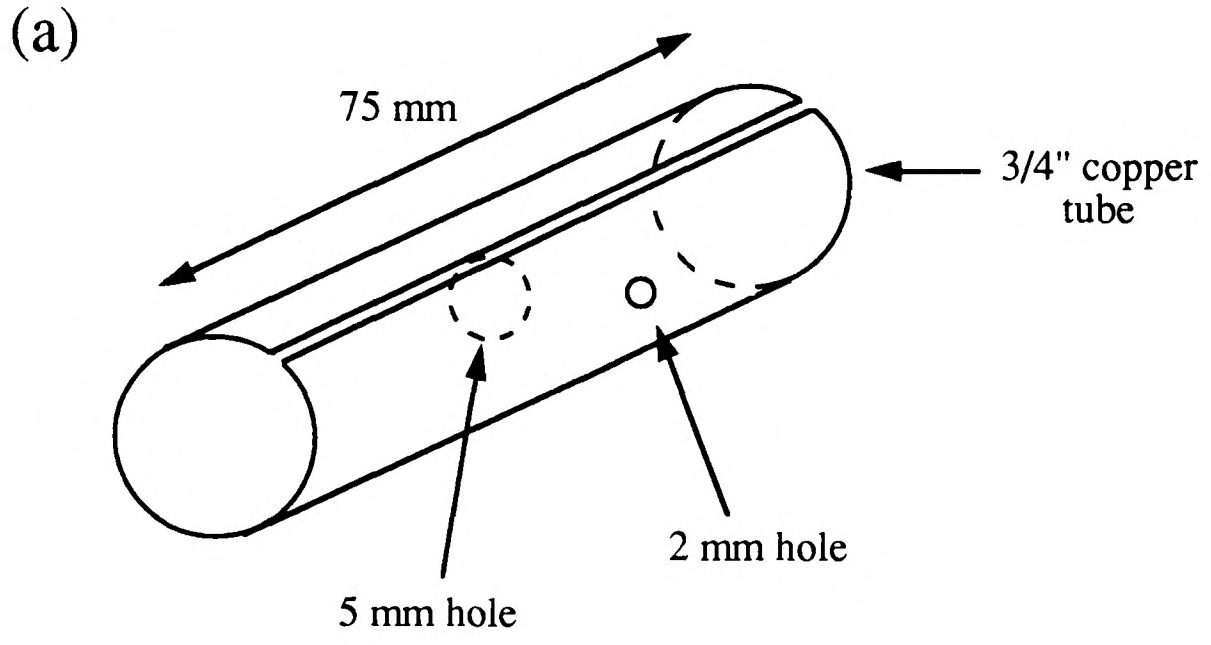


Figure 4.15: (a) tubular baffle. (b) endcap.

the interaction region to the photomultiplier along the path of the atomic beam. However, some scattered UV was directed out of the open ends of the tubular baffles themselves. To counteract this, copper end caps were placed over the ends which pointed towards the photomultiplier. This reduced the UV background count rate in the second can to around 2 counts s^{-1} per milliwatt of intra-cavity UV power. In beam mode, a typical intracavity power was 50 mW, giving a background of $\sim$ 100 counts s^{-1}. Beam mode signals under these conditions were usually a few hundred counts s^{-1} (§5.10).

4.10 Summary

The 40 cm Dural cavity with 30 cm mirrors (shown in Plate I) was the one which was ultimately used for all beam mode work, including the eventual 1S Lamb shift measurement. It always had the same mirrors: the Acton 25 mm high reflector and the fragment of Acton medium reflector. Despite its somewhat eccentric appearance this mirror set gave adequate enhancement and the degradation was sufficiently well characterised to be an inconvenience rather than an insurmountable problem. Given that both the 30 cm and 40 cm RoC mirrors had shown this effect despite being from different manufacturers (and that the small medium reflectors had been prone to permanent damage from the UV beam), there seemed little point in delaying the progress of the work further by trying out yet another mirror set which was unlikely to perform much better.

While the exact mechanism for the degradation is not certain, it seems likely that it is somehow connected with oxide-based dielectric mirror coatings. The Münich group have also experienced this problem, and have overcome it by using mirrors with fluoride based coatings. As mentioned above, we had observed that degradation was slightly more severe in cryopumped experiments. The use of fluoride coatings may become unavoidable if in future work it becomes necessary to reduce the background pressure further in an attempt to improve on signal.

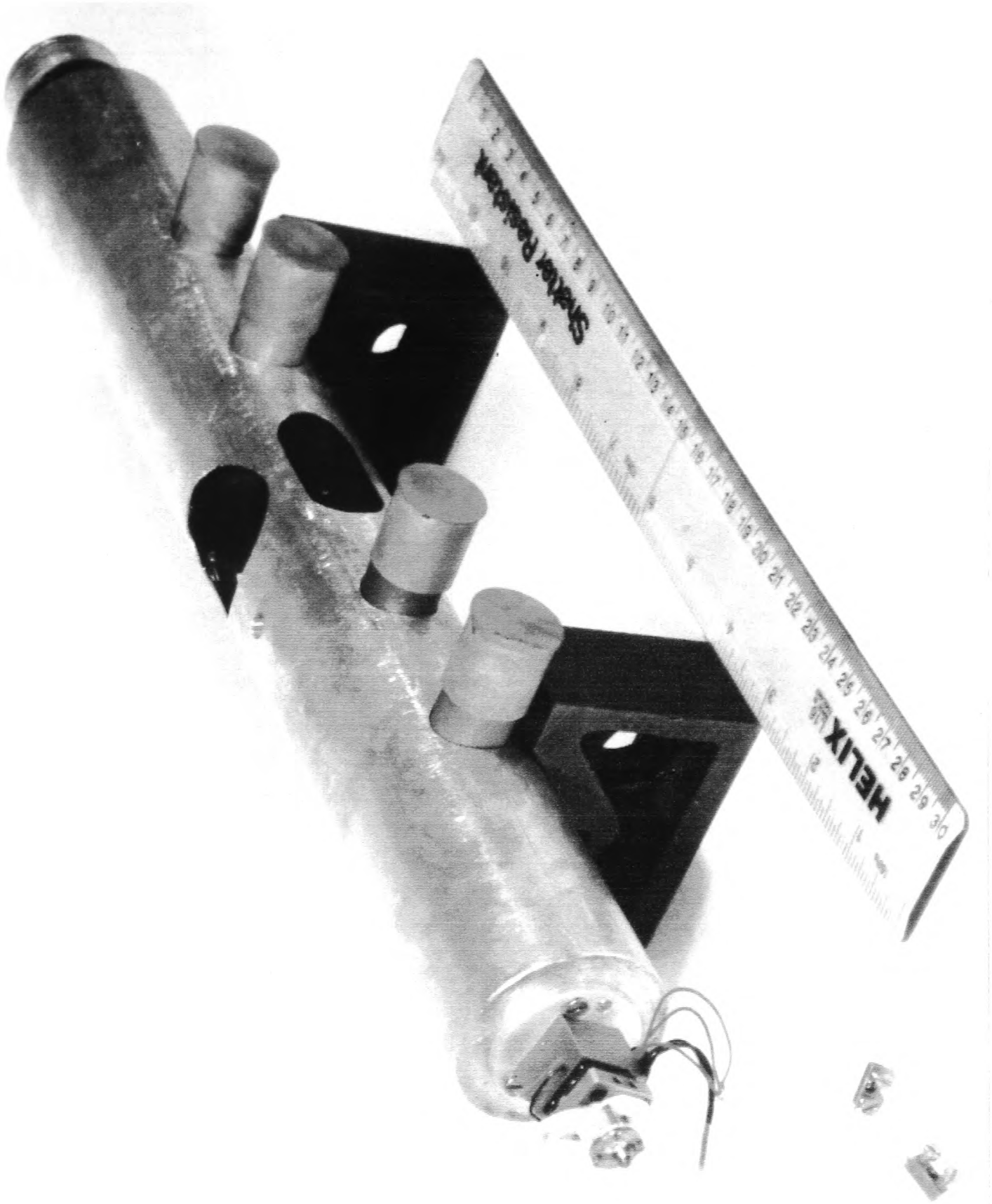


Plate I: The 40 cm Dural cavity, with the 30 cm RoC Acton mirror set and the tubular baffles. The medium reflector fragment can be seen mounted on the ASM20 mirror mount.

Chapter 5

The hydrogen beam and 1S–2S excitation

5.1 Introduction

This chapter describes the apparatus required for the excitation of the 1S–2S transition in an atomic beam.

The process is illustrated schematically in Fig. 5.1. 243 nm radiation from the frequency-doubled laser excited the transition at the waist of the enhancement cavity described in Chapter 4. This process generated an optically excited beam of metastable hydrogen atoms. The laser frequency was set using a wavemeter, offset locked to a stabilised cavity and scanned under computer control over the transition with an acousto-optic modulator (AOM). The metastable beam played an important part in the second part of the experiment—the direct comparison of 1S–2S with Balmer-β (Chapter 6).

The system as described evolved over a period of time. A brief account of its history is given here to set the later sections in context. The first experiments attempted with this apparatus were "cell mode" ie. the pressure in the chamber was maintained at around 0.5 Torr with a rotary pump and the photomultiplier was placed directly over the interaction region to pick up the Lyman-α fluorescence from collisionally quenched atoms (see §3.5). The purpose of this exercise was to check the performance of the laser, hydrogen source etc. before proceeding to the more demanding "beam mode". As explained in §3.5, beam mode involved pumping the chamber with the turbopump to keep the background pressure at the $\sim 10^{-4}$ mbar level. The excited atoms were detected by monitoring Stark-induced Lyman-α fluorescence downstream from the interaction region. The earliest beam mode work was done with the nozzle, interaction region and detection region as close together as possible (d and R of Chapter 3 small) in order to maximise the observed 1S–2S signal. Later, the nozzle was pulled back to improve the collimation of the metastable beam and the detection region was moved further away to allow room for the Balmer-β excitation.

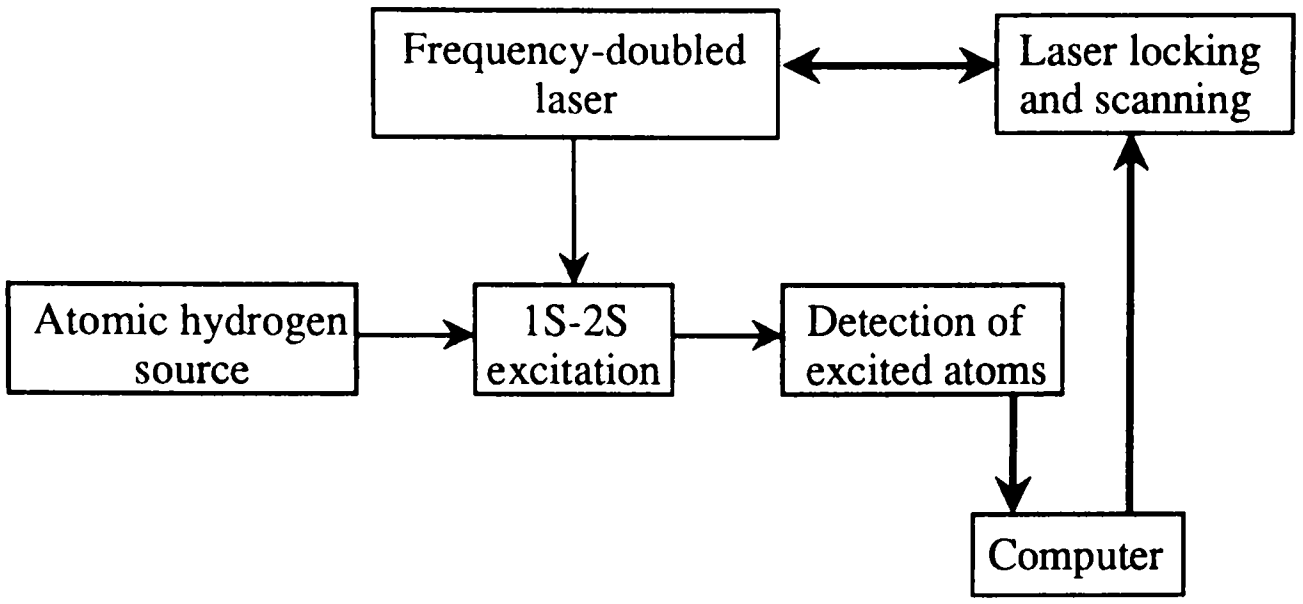


Figure 5.1: The 1S–2S excitation—schematic.

Under these conditions it was necessary to lower the background pressure by use of the cryopump in order to see a signal at all.

5.2 The vacuum system

The vacuum system (Fig 5.2) was based on two stainless steel cubical boxes with an external side measurement of 26 cm and 1/2" thick walls. They were constructed by the Nuclear Physics Workshop in Oxford.

Five of the six faces of each box had 6" diameter apertures surrounded by eight M8 tapped holes. The sixth face had a similar 4" aperture. Stainless steel flanges of diameter 22.5 cm were compatible with the 6" apertures and could be bolted onto the boxes in the desired orientation. Aluminium seals were used for all except the top and end flanges of each box since the latter had frequently to be removed; Viton co-seals were used there. The faces with the 4" apertures were used to connect the two boxes as explained below.

Box 1 contained the 1S–2S interaction region. In the final version, the UV enhancement cavity was supported in two ISO63 sidearms (ID 70 mm), centred on the horizontal axis of the system at a distance of 40 mm from the centre of the box. The end flange had a CF40 flange holding an XYZ manipulator, through which the

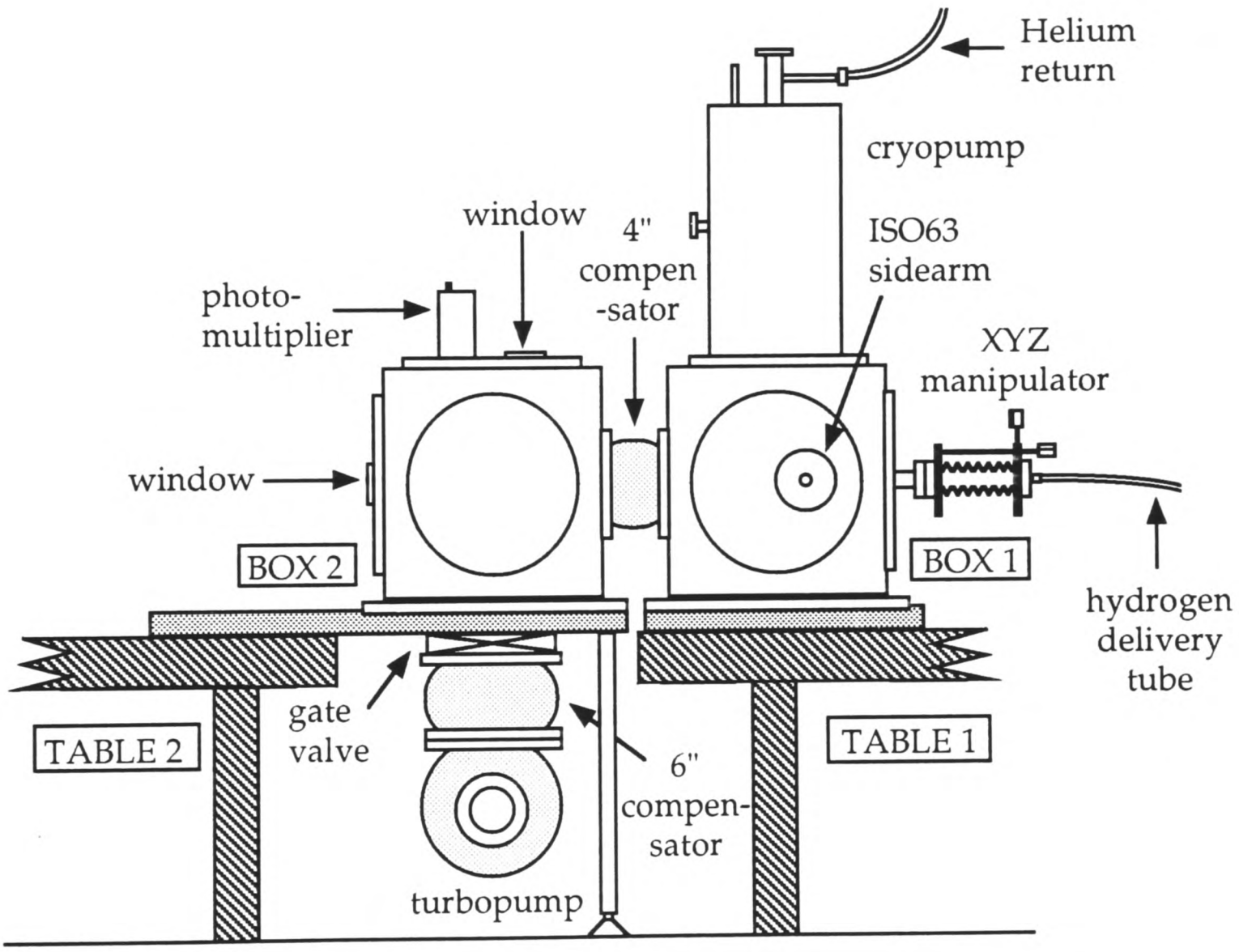


Figure 5.2: The vacuum system.

atomic hydrogen delivery tube entered the chamber (§5.3.2). Box 1 also had an air admittance valve, a Penning gauge and several spare ports.

Box 2 contained the detection system and ultimately the Balmer-β excitation region. The top flange held the photomultiplier in its housing and a window to admit light from the Balmer-β laser. The end flange had a central window, through which the alignment of the parts of the metastable beam could be checked.

The boxes were connected by a 4" vibration isolating bellows, or "compensator" (Balzers DN100 ISO-K) and each rested on its own 2" high rails on *separate* steel tables. In the case of box 2, the rails overhung the edge of the table by 28 cm. A turbomolecular pump (Balzers TPU510) was hung from a 6" compensator (Balzers DN160 CF-F) attached to the base of box 2. The turbopump had a pumping speed of 500 litres/second for H_2 and could be isolated from the vacuum chamber by a pneumatically operated 6" gate valve (VAT SVV 150 PF). The purpose of the two compensators (and the mounting of the boxes on separate tables) was to isolate the UV enhancement cavity in box 1 from the vibration arising from the 60,000 rpm rotation of the turbopump vanes (§4.9).

Additional pumping speed was provided by a liquid helium cryopump on top of box 1. The cryopump was designed by J. Cosier of the Clarendon Laboratory Cryogenic Facilities Group, and manufactured in the Clarendon Laboratory workshop. Its main features are shown in Fig. 5.3. It contained a 1.2 litre liquid helium reservoir, below which were blackened copper radiation baffles of diameter 4.5". The baffles protruded a distance of 10 cm into the vacuum chamber. The cryopump was a single fill device, one fill of helium lasting approximately seven hours. After this time the hydrogen which had condensed on the pump would evaporate off and be pumped away by the turbopump. The pumping speed of the cryopump was about twice that of the turbopump. A typical pressure achievable with both pumps in operation and no hydrogen input was 6×10^{-7} mbar. This is to be compared with 1.5×10^{-6} mbar with the turbopump alone. With 0.4 Torr of hydrogen in the discharge region, typical chamber pressures were 4×10^{-5} mbar with just the turbopump, and 1.2×10^{-5} mbar with both pumps. The survival fraction for metastable hydrogen atoms at these pressures after a distance of 40 cm can be calculated using equation 3.26. We find that approximately 4% can be expected to survive 40 cm at the higher (turbopumped) pressure compared to approximately 37% at the lower (cryopumped) pressure.

5.3 The atomic hydrogen source

The atomic hydrogen source was based on that described in [21] and is shown in Fig. 5.4. Molecular hydrogen was dissociated in a radio-frequency discharge. The atomic hydrogen was then transported through PTFE tubing to the 1S–2S interaction region inside the vacuum can. The hydrogen atoms emerged through a nozzle with a slit of dimensions 8 mm by 250 μm.

The component parts of the atomic hydrogen source are described in detail below.

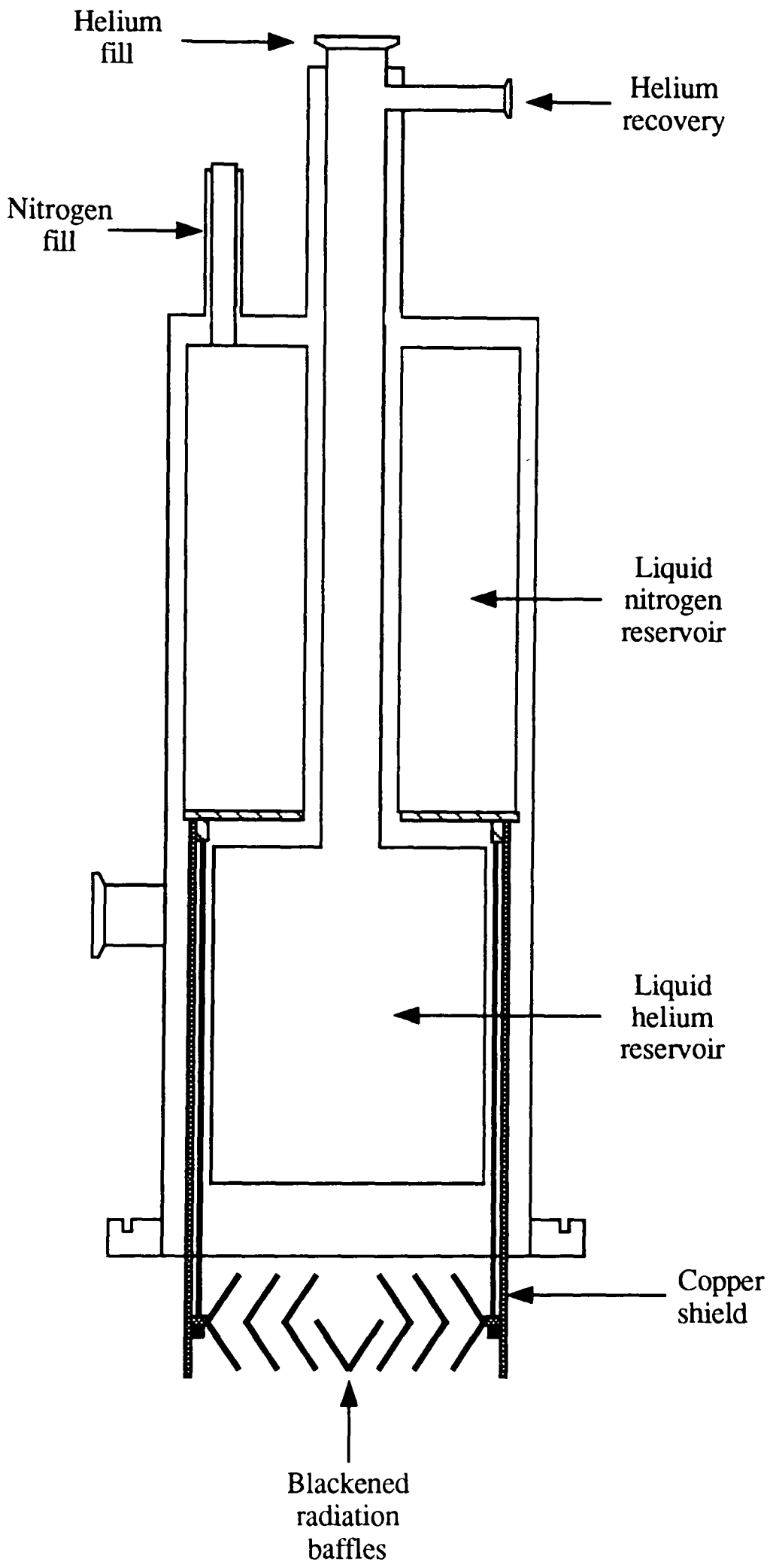


Figure 5.3: The cryopump.

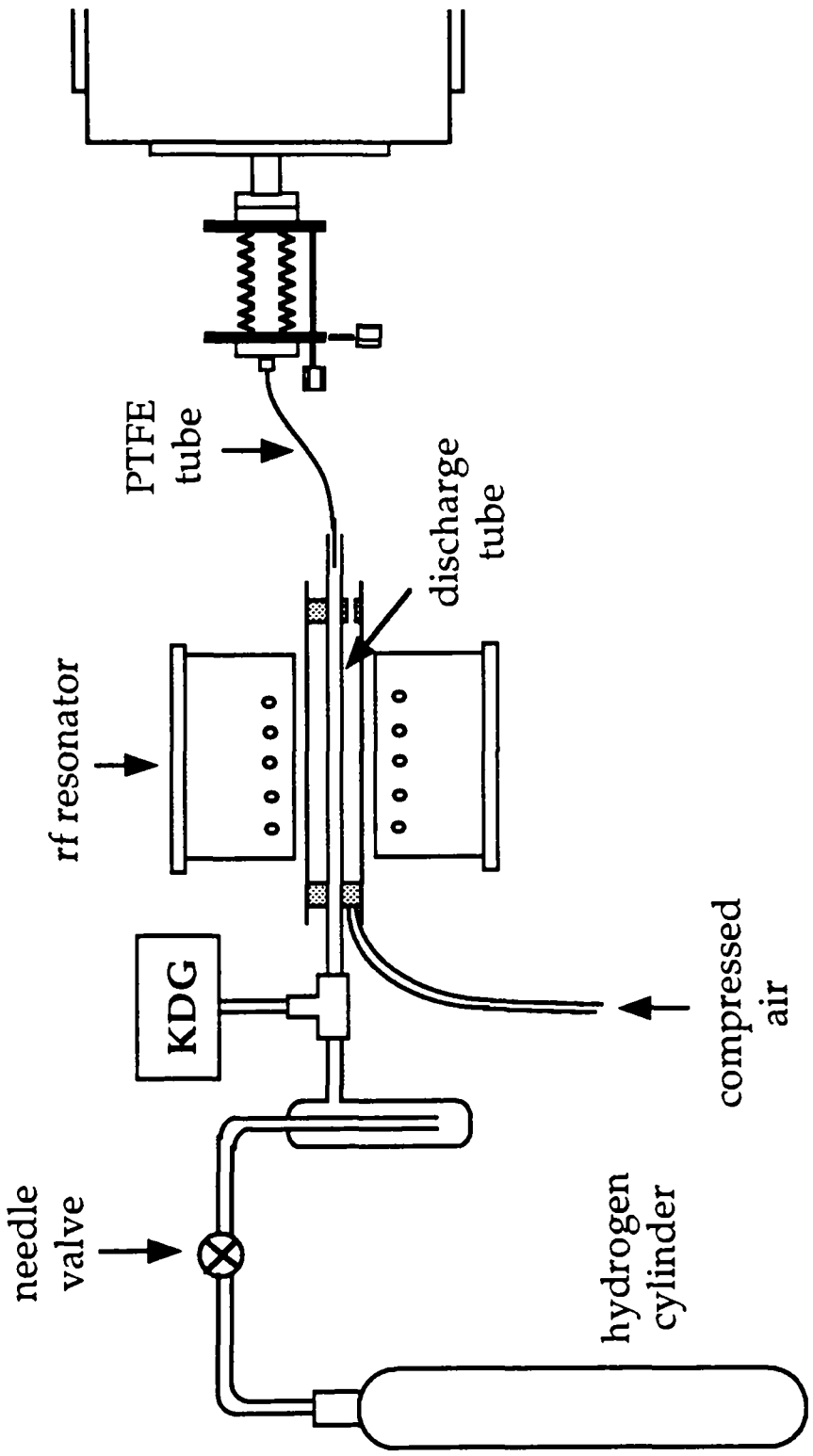


Figure 5.4: The atomic hydrogen source.

5.3.1 Dissociation of molecular hydrogen

The hydrogen gas was BOC industrial grade (purity 99.5%). The main impurity was compressor oil so a liquid nitrogen cold trap was included in the delivery system between the gas bottle and the discharge. The gas was pumped through the dissociator under steady flow conditions. A needle valve controlled the flow rate and the pressure in the discharge tube. A KDG inductance manometer connected into the line just before the Pyrex tube measured the pressure in the discharge region.

The dissociator consisted of a Pyrex discharge tube placed inside a radio-frequency (rf) resonator [45], the design of which was based on the analysis of MacAlpine and Schildknecht [46]. It was essentially a quarter-wavelength section of a transmission line, short-circuited at one end. The helical inner conductor consisted of a 13-turn copper helix (72 mm in diameter and 106 mm in length) enclosed in a copper cylinder (129 mm in diameter and 170 mm in length). The whole was enclosed in a copper box to provide extra shielding of stray rf.

About 50 watts of rf power at 28.7 MHz from a Heathkit DX–100U amateur radio transmitter were coupled into the resonator through a single copper loop near the short-circuited end. The somewhat elderly Heathkit—based as it is on valve technology—was ideal for this purpose because it can deliver large amounts of power and take sizeable quantities of back-reflected power without suffering damage.

The Pyrex discharge tube was approximately 30 cm long with an internal diameter of 10 mm. It was enclosed in a cylindrical jacket which facilitated cooling by compressed air, this whole assembly fitting inside the inner conductor of the rf resonator as shown in Fig. 5.4. Pyrex was used for the discharge region because it has been found to give a high dissociation fraction provided that the walls of the discharge tube do not get too hot.

The dissociation fraction also depends very sensitively on the cleanliness of the discharge tube. This is because the main recombination mechanism for atomic hydrogen is a three body process so it primarily takes place on the walls of the tube. The rate is increased by the presence of dirt. A satisfactory method of cleaning was developed which involved soaking the new tube in hot Decon 90 for a few hours, then rinsing thoroughly with distilled water prior to use. It was found that after a prolonged period of running, the discharge tube developed a transparent, filmy deposit on its inside surface. Some attempts were made to clean this off with dilute hydrochloric acid, but it was eventually found more satisfactory to replace the soiled tube with a fresh one.

If the Pyrex tube was kept properly clean, the discharge showed the deep pink colour characteristic of atomic hydrogen immediately upon switching on. Using a pocket spectroscope one could clearly see the first three lines of the Balmer series with little trace of a molecular continuum, indicating that the hydrogen was being almost completely dissociated.

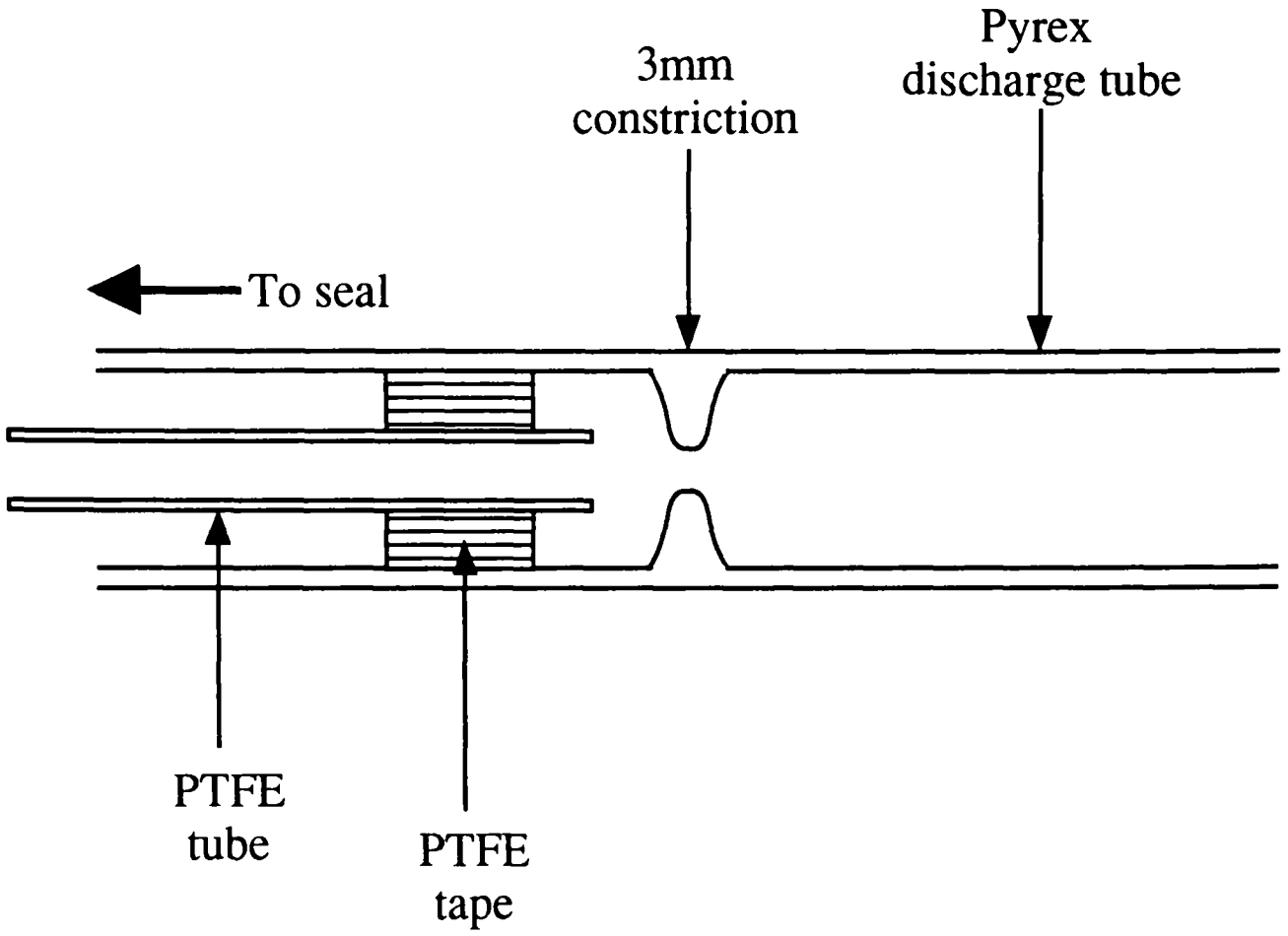


Figure 5.5: The constriction in the Pyrex discharge tube and the end of PTFE tube.

5.3.2 Transport of atomic hydrogen

The atomic hydrogen was transported to the 1S–2S interaction region through a length of PTFE tubing. PTFE was used because it has a low surface recombination rate for hydrogen at room temperature [47]. During the course of the work, we tested a number of different types of tubing in an effort to produce a reliable atomic hydrogen delivery system. In an experiment of this complexity, it was essential to be certain that an absence of signal was not due merely to a lack of atomic hydrogen in the interaction region.

The Pyrex discharge tube had a constriction with a 3 mm aperture near the downstream end. The end of the PTFE transport tube was positioned close to this constriction (Fig. 5.5). This arrangement minimised the amount of bare Pyrex in the path of the atomic hydrogen while the constriction prevented the discharge from running into the PTFE. It had been found [21] that if this occurred, the end of the PTFE would be blackened and the hydrogen transport would be ruined.

It was necessary to have some means of determining the hydrogen atom density in the interaction region. For this purpose we used a Thermoflake (Thermometrics No. A50–2F40M105Q). This is a thick film thermistor material (a sintered combination of nickel oxide, manganese oxide and cobalt oxide) which has been shown [48] to be useful as a selective detector of atomic hydrogen. The material responds to

the presence of atomic hydrogen by undergoing a drop in resistance. Surprisingly, the mechanism responsible for this response is not certain. Two possibilities are suggested in [48]. Atomic hydrogen could be recombining on the surface of the Thermoflake. This reaction is exothermic (the binding energy of the molecule is 4.476 eV) and can heat the material causing a change in resistance. Alternatively, hydrogen atoms could be undergoing chemisorption (ie. becoming chemically bound) on the flake surface. The electron from each atom is transferred to a surface state in the semiconductor to form an accumulation layer which, because of an excess of electrons, leads to an increase in conductivity. We did not pursue the matter since for our purposes, it was not necessary to know which of these mechanisms was responsible for the observed Thermoflake response.

Thermoflakes are 1.0 mm square and 50 μm thick, with two platinum electrodes on opposite edges of one face. The flake is held by four 18 μm platinum wires (one at each corner) attached to four posts on a TO-5 header. Needless to say, Thermoflakes are extremely fragile. The resistance of a *new* Thermoflake plus connecting wires was about 0.8 MΩ in the absence of atomic hydrogen. The "no hydrogen" resistance of a Thermoflake tended to rise over a period of time. This may be connected with contamination of the flake surface. Along with this it was found that the absolute resistance change for a given set of conditions also tended to alter. It turned out that the fractional (or percentage) change in resistance was the best indicator of the atom density.

It should be noted that because of the problem mentioned above, and the fact that the flake response is not linear with atom density, it is almost impossible to make quantitative measurements of hydrogen atom densities using a Thermoflake. The device was useful for making qualitative comparisons of the performances of different delivery systems or checking that conditions in the interaction region were similar to those which existed on a previous occasion.

In order to test the hydrogen transport properties of different tubes, a Thermoflake was connected to a vacuum BNC leadthrough set into a 1/2" PTFE T-piece immediately downstream from the discharge. The flake response was noted in order to give an indication of the atomic hydrogen density at that point. A length of the tubing under test was then inserted between the discharge and the T-piece containing the Thermoflake. The same flow rate was maintained for each sample. The flake signal under these conditions gave an indication of the atom density at the output of the delivery tube and hence the efficiency of hydrogen transport through it.

Four different types of delivery tube were tested:

- 1/2" bore PTFE.
- 1/2" bore Pyrex.
- 1/4" OD, 3/16" ID PTFE.
- 6 mm OD, 4 mm ID PTFE.

Table 5.1: Hydrogen transport efficiency through different types of tubing.

Tubing type	λ(cm)	Transport through 40 cm
1/2" PTFE	90	65%
1/4" PTFE	40	35%
1/2" Pyrex	30	25%
4 mm PTFE	15	5%

The results are summarised in Table 5.1. It was assumed that the flake signal S at the end of a tube of length l was related to that at the start of the tube (S_0) by an exponential law of the form

$$S = S_0 \exp - \left(\frac{l}{\lambda}\right) \tag{5.1}$$

The table shows the experimental value of λ for each tube and, for comparison, the calculated approximate percentage transport of atomic hydrogen through a 40 cm length.

As has been mentioned earlier, PTFE has a low surface recombination rate for atomic hydrogen and therefore good transport efficiency. However, transport efficiency through a given tube does seem to depend on the bore. Note that the smallest bore PTFE performed less well than the Pyrex, which is known to have a poorer transport efficiency than PTFE. Walraven and Silvera [49] obtained a dissociation fraction of 60% at the end of 25 cm of 5 mm bore PTFE with an atom density comparable to ours of 6×10^{20} m^{-3}, corresponding to a value for λ of 49 cm and a predicted transport through 40 cm of 44%. Our atom density was $\sim 10^{21}$ m^{-3} (see §3.7.2). Our results therefore compare well with those of Walraven and Silvera, remembering that the transport efficiency is very dependent on the cleanliness and surface quality (especially at the ends) of the transport tube. In our experience, different lengths of the same type could show considerable variation in performance. Given this, and the fact that the existing vacuum leadthrough was designed for use with 1/4" tubing, we decided to go ahead and use the 1/4" PTFE, even though it did not come out top in the above test. This tubing also had the advantage of being fairly flexible, enabling it to be bent into an S-shape as described below.

For the purposes of the above measurements, the Thermoflake was connected into a Wheatstone bridge circuit as described in [48]. The drop in resistance caused by the presence of atomic hydrogen was reflected by a change in the bridge imbalance

voltage, which was monitored on a chart recorder. We were therefore able to study the behaviour of the flake response with time. When the discharge was first struck, the flake signal would start to rise steadily before eventually flattening off. Turning off the discharge would cause the signal to drop abruptly to the "no hydrogen" value. On several occasions, we observed a series of "dips" superimposed on the general trend. Typically there were several small dips followed by a drop to the "no hydrogen" value, which coincided with the discharge momentarily appearing whitish (ie. more molecular). The signal then began to rise again. This phenomenon was not investigated in any great detail, but as it occurred only in the "running in" period just after a new tube had been installed, it seemed to be connected with the presence of dirt in the system.

It was therefore vitally important to keep not only the discharge tube but also the PTFE clean. The procedure developed to ensure this was as follows. Firstly, any new length of tube was soaked in hot Decon 90 for two to three hours and then rinsed thoroughly with distilled water. There was no real benefit to be gained in soaking for a longer time (eg. overnight) because then it was more difficult to rinse the detergent away properly. The cleaned PTFE was always handled with gloves and special care was taken not to dirty the ends when threading it through the various vacuum fittings. Before these were finally done up, the ends of the tube were sliced off with a clean razor blade, in order to expose a fresh, clean PTFE surface. Great care was taken not to damage the interior of the tube by scratching or kinking as it was feared that such damage to the PTFE surface would increase the recombination rate and spoil the atomic hydrogen transport efficiency.

The PTFE delivery tube entered the vacuum can through an XYZ manipulator (Vacuum Generators XYZ50) via a 1/4" swage lock fitting set into a CF40 stainless steel flange (Fig. 5.6). A stainless steel pipe attached to the inside of the flange supported the PTFE tube, which terminated in a nozzle approximately 8 mm$\times$250 μm in area and 2 mm in length. The manipulator enabled the nozzle to be positioned up to 25 mm away from the 243 nm beam. The total length of the PTFE tube from discharge to nozzle was typically 40 cm. The PTFE tube was bent into an S shape in order to reduce the amount of Lyman-α radiation which could travel through it from the discharge into the vacuum can, where it would be picked up by the photomultiplier and contribute to the background count rate.

The nozzle was formed by squeezing down the end of the PTFE tube itself. This arrangement avoided the introduction of a separately machined piece of PTFE: it was feared that machining marks, burrs etc. would spoil the hydrogen transport by increasing the recombination rate. The most satisfactory method of nozzle formation is shown in Fig. 5.6 in which the PTFE was clamped between two Dural jaws. Prior to clamping, the end of the tube was squeezed with pliers wrapped in clean tissue. In order that it squeeze down more evenly, small nicks were made with a clean razor blade at the edges of the slit. Even so, there was a tendency for the slit to close up in the centre. If this happened, the best solution was to close it down completely with

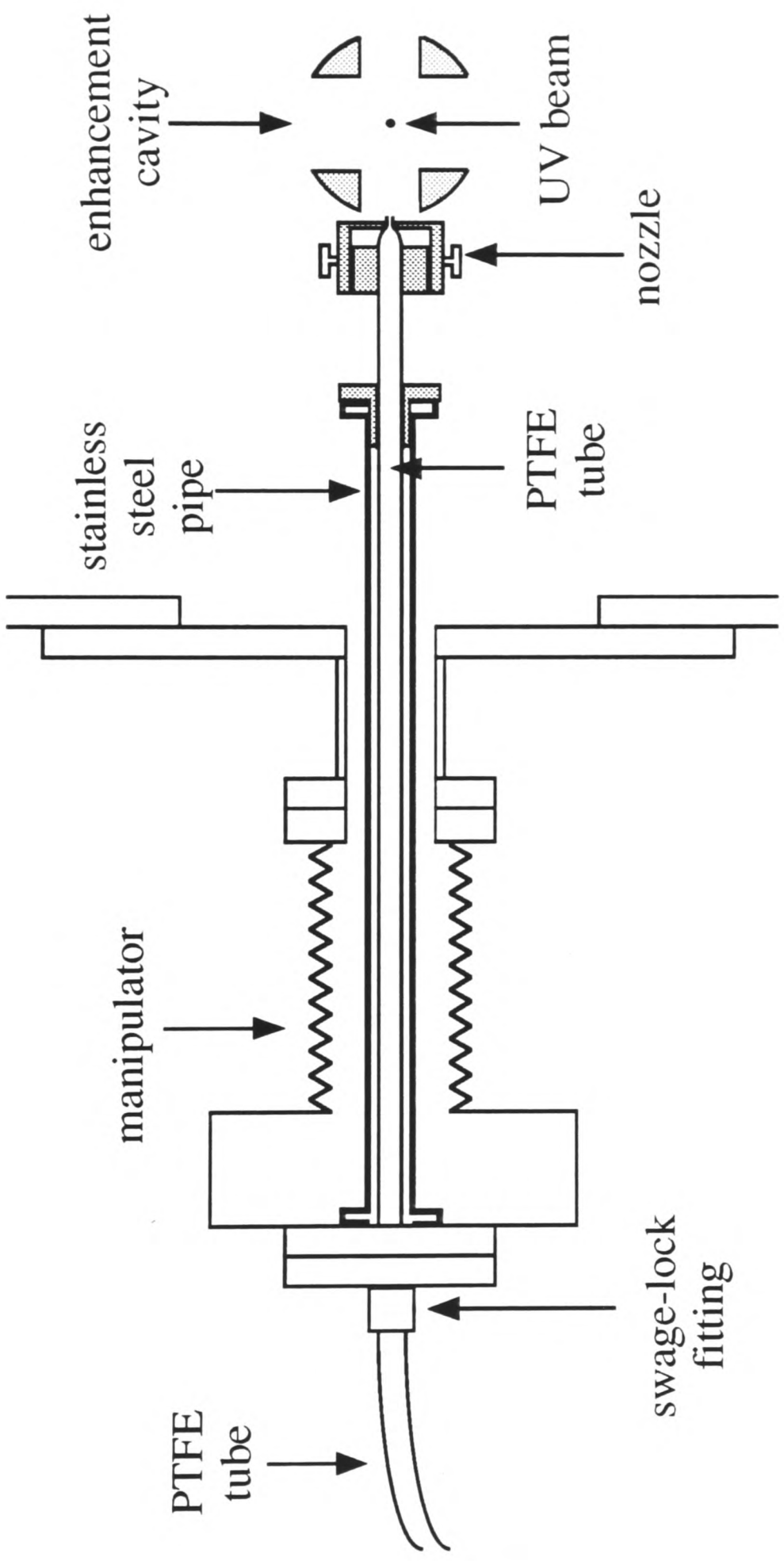


Figure 5.6: The PTFE tube entering the vacuum can, the manipulator and the hydrogen nozzle.

the Dural jaws and leave it for a period (usually overnight) before loosening the jaws to open it up to the correct size.

5.3.3 Running conditions

Once a reliable hydrogen delivery system had been developed, it was necessary to determine a "benchmark" Thermoflake signal which we knew would correspond to an adequate flux of ground state hydrogen atoms through the interaction region.

For these purposes, the flake response was measured as follows. The Thermoflake was mounted on stiff copper wires attached to a vacuum BNC in a KF40 blanking flange. The wires supported the flake and formed the electrical connections for the resistance measurement. The wires could be bent to hold the flake in the location of the 1S–2S interaction region at a standard distance of 25 mm from the PTFE nozzle. The *percentage* change in resistance caused by the atomic hydrogen flux was measured with a digital ohmmeter. With 0.4 Torr discharge pressure and about 4×10^{-5} mbar in the turbopumped chamber, it was found that a resistance change of 3% corresponded to an adequate hydrogen delivery. If alterations had been made to the system, there was a "running in" period of about a day before the hydrogen delivery would be back up to standard.

Under the conditions described above, calculations based on the geometry of the excitation and the observed two-photon signals suggested a dissociation fraction of about 10% in the interaction region.

5.4 The 1S–2S interaction region

The 1S–2S transition was excited at the waist of the UV enhancement cavity described in Chapter 4. The cavity used for the final experiment was the 40 cm Dural version, the design and construction of which are described in Chapter 4. Some further information relevant to the 1S–2S excitation is given here.

The cavity was supported in the ISO63 sidearms of the vacuum can by vibration isolating rubber pads as described in §4.9. Attached to each sidearm were adaptors which terminated in KF10 flanges. Sealed on to these were quartz windows (25 mm diameter, 3 mm thick and anti-reflection coated for 243 nm) through which the UV beam entered and left the vacuum can. The wires from the ASM20 piezo-controlled mirror mount were connected to a vacuum BNC leadthrough at the input end of the cavity.

The XYZ manipulator enabled the hydrogen nozzle to be moved with respect to the 243 nm beam. Before any attempt was made to excite the 1S–2S transition, a visual check was made (through the end window) to ensure that the slit through which the atoms emerged was vertically aligned with the 243 nm beam inside the enhancement cavity. Because of the comparatively large distance to the detection region, the size of the 1S–2S signal depended very critically on this alignment.

It was important to earth the cavity spacer to the vacuum can, to avoid quenching of the metastable atoms by stray electric fields before they reached the detection region.

5.5 The detection system

The metastable atoms generated by the 1S–2S excitation were detected by monitoring, with a photomultiplier, the Lyman-α fluorescence from the 2P level. As explained in §3.5, the atoms were transferred to the 2P level either by collisions in the interaction region (cell mode) or by Stark mixing downstream from the interaction region (beam mode).

The solar-blind photomultiplier (and its dynode chain) was contained in a stainless steel housing (Fig. 5.7), inserted into a 71 mm diameter hole in the top flange of one of the vacuum cans. It could be installed in either box as the occasion demanded. Vacuum seals were provided by an O-ring on a flange around the housing and one in a groove on the inside of the base of the housing, which sealed against the photomultiplier tube as shown. The dynode chain was therefore not under vacuum.

For cell mode work, the photomultiplier was positioned directly over the interaction region to detect the fluorescence from the excited atoms. To cut down on the background from scattered 243 nm radiation (see §4.5), the Lyman-α filter was in place over the photomultiplier window.

In beam mode, the excited atoms travelled a distance downstream to a region where they were quenched by a small electric field. The quench wires were contained in a stainless steel extension attached to the base of the photomultiplier housing (Fig. 5.7). The metastable beam entered through a 15 mm diameter circular hole. A second 15 mm hole enabled the alignment of the quench wire assembly and the interaction region to be visually checked through the end window of the vacuum system.

The design of the quench wires was essentially that described in [40] and is illustrated in Fig. 5.8. Two sets of "plates", above and below the atomic beam, were formed by winding thin copper wires around two 7 mm thick brass rods, 20 mm apart. The plates were separated by an electrically insulating slice roughly halfway along each brass rod. The pair of plates through which the beam passed first were grounded by being directly connected to the vacuum can. The second pair of plates were held at 30 V. The metastable atoms thus passed through a grounded, zero field region before encountering a voltage step. Quenching was likely to occur at the leading edge of the voltage step. The junction between the two pairs of plates was therefore $\sim$ 5 mm downstream from the centre of the photomultiplier window to ensure that most of the atoms would emit Lyman-α photons directly below it.

The Lyman-α interference filter was removed for most beam mode work in order to increase the sensitivity of the photomultiplier to Lyman-α by about an order of magnitude. However, as the sensitivity to 243 nm photons was also increased by this

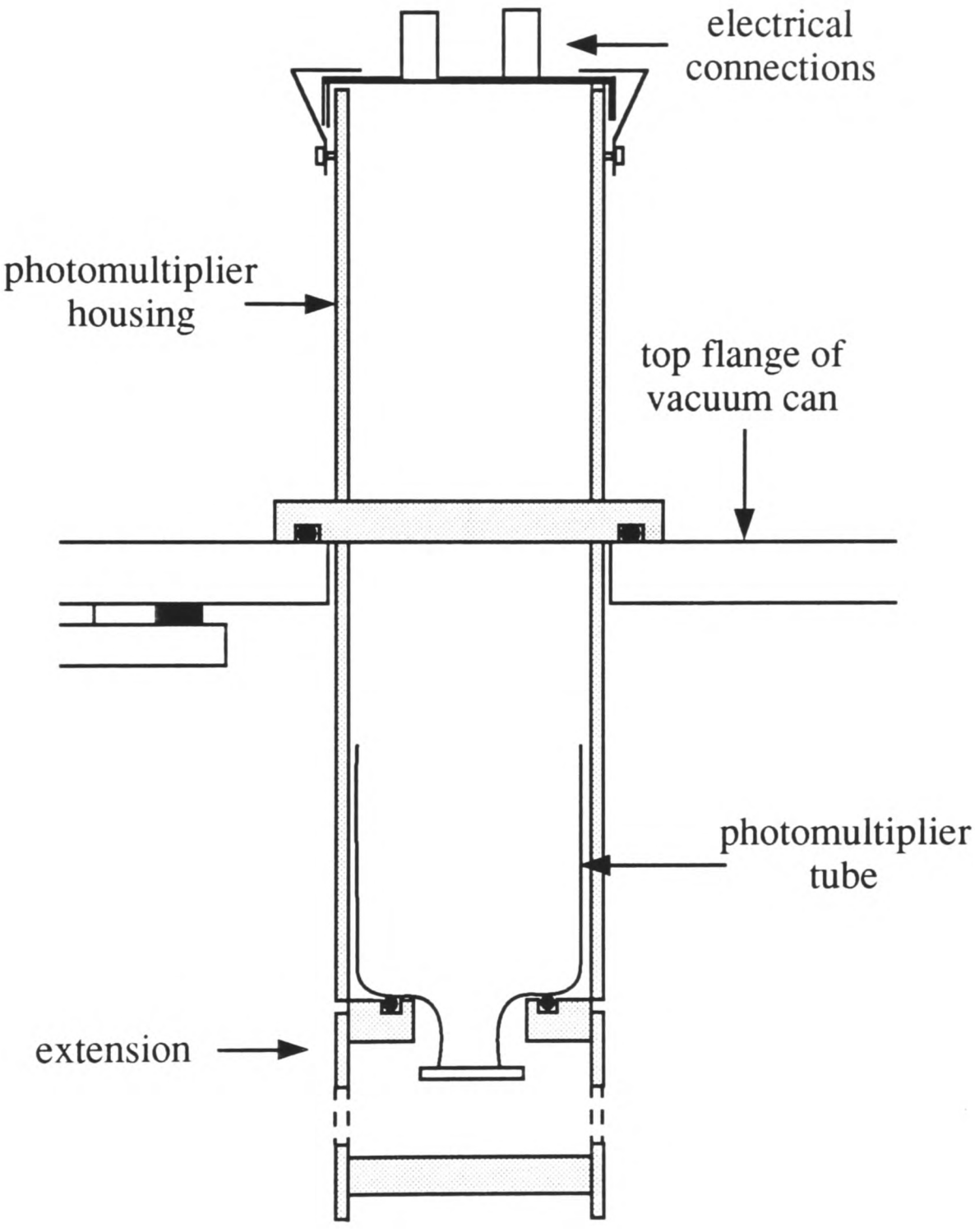


Figure 5.7: The photomultiplier housing and extension.

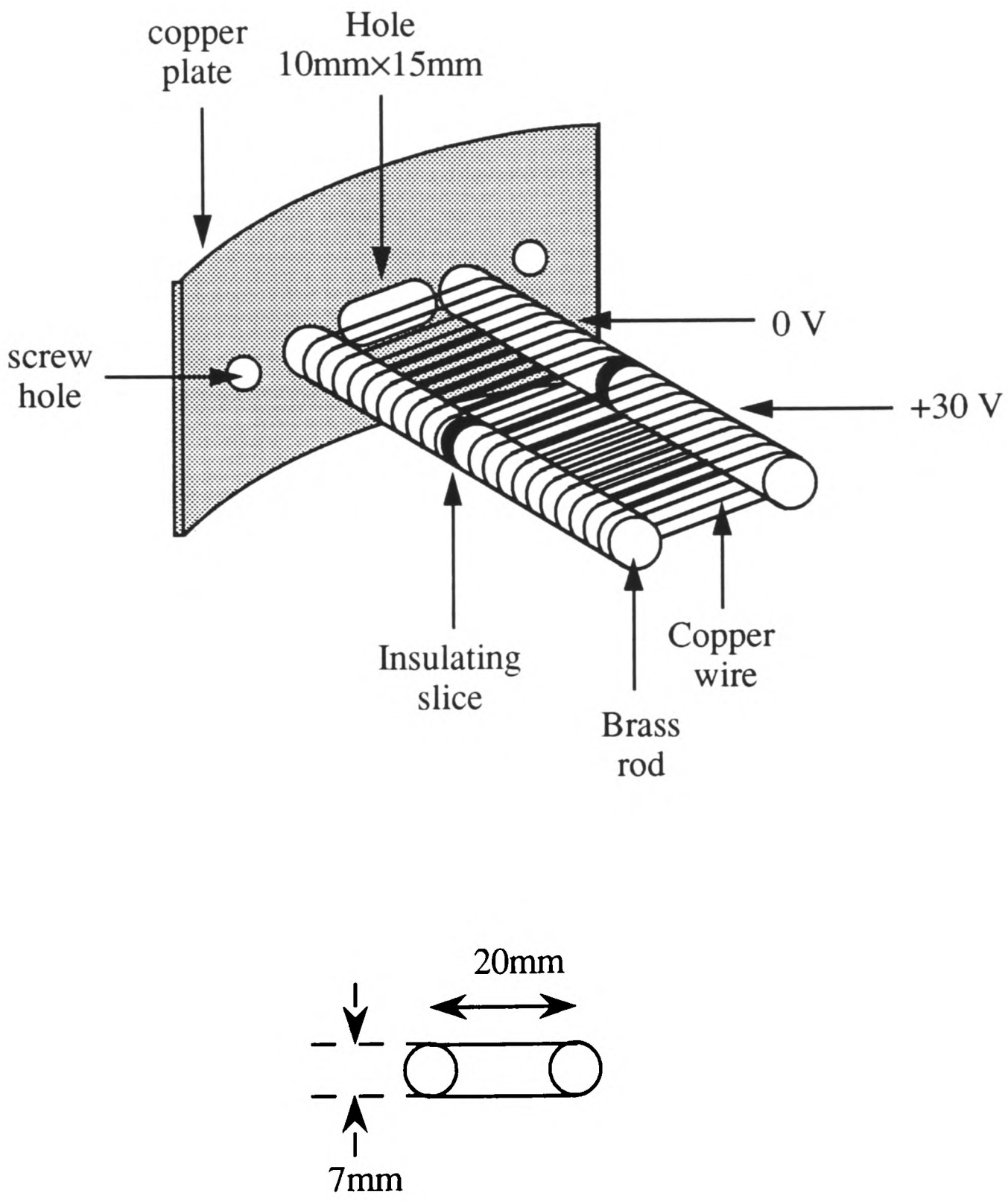


Figure 5.8: The quench wires.

measure, extra precautions had to be taken to reduce the amount of 243 nm radiation reaching the detection region (even when the photomultiplier was some distance away from the 243 nm beam). The baffling of the UV enhancement cavity is described in §4.5. In addition, a copper box with a 15 mm hole was added in front of the hole through which the metastable beam entered the detection region. This extra baffle prevented a direct line of sight between the 243 nm beam and the photomultiplier window.

The detection efficiency for atoms reaching the quench region was discussed in §3.7.3 and turns out to be 0.3% with the Lyman-α filter in place and 1% without it.

The photomultiplier was used with a tube voltage of 3 kV. The cathode was held at ground to reduce the build-up of stray electric fields in the detection region. The photopulses were amplified in two stages of a pulse amplifier (Stanford Research Systems SR440) and sent to a photon counter (Stanford Research Systems SR400). The discriminator level was set to 20 mV. The photon counting system was rather sensitive to pickup of stray rf from the discharge region, so care was taken to have a common earth for all the devices.

5.6 The frequency doubled laser

The laser which performed the 1S–2S excitation was a modified Coherent Radiation CR-699 ring dye laser operating at 486 nm. 243 nm radiation was generated by intracavity frequency doubling in β-barium borate (BBO). Type 1 phase matching was achieved by angle-tuning the crystal. The dye was Coumarin 102 and was pumped with the violet output of a Coherent Radiation Innova 100 krypton ion laser. The krypton typically gave a power of 5 W.

The modifications made to the dye laser are described in [21]. They are summarised here.

- The Brewster cut BBO crystal was inserted into the ring cavity in place of the astigmatic compensation rhomb at the tight focus.
- The magnet stack on the optical diode was reversed in order to run the ring "backwards". This meant that the second harmonic beam left the laser cavity through the upper fold mirror.
- The upper fold mirror (high reflector) was replaced by a dichroic mirror with a transmission of 87% for 243 nm and 0.08% for 486 nm. The normal output coupler was replaced with one having a transmission of 0.3% at 486 nm. The purpose of this was to optimise the circulating fundamental power.

During the course of the work, two different BBO crystal mounts were used. The first was the same as that described in [21]. The 8 mm long Brewster cut crystal was sandwiched between two quartz plates. The second harmonic beam emerged

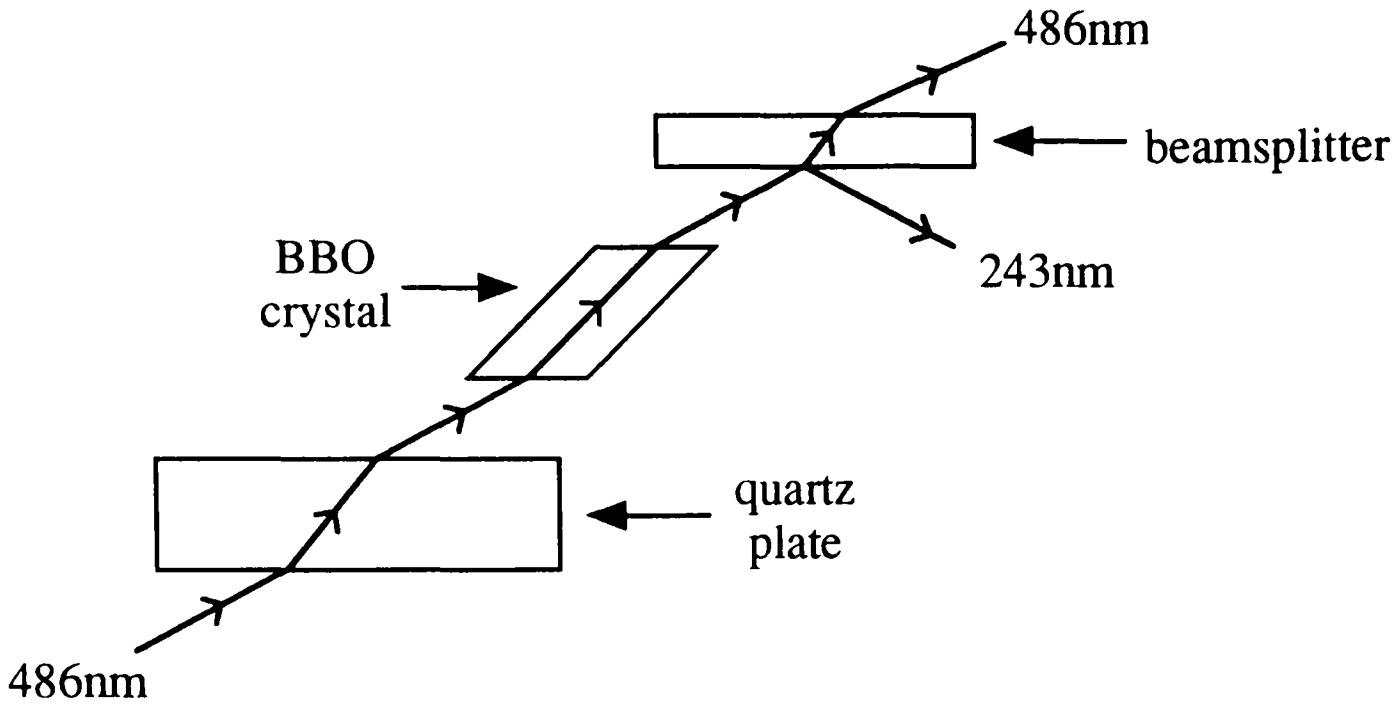


Figure 5.9: The new BBO crystal mount (schematic).

from the crystal in the same direction as the fundamental and left the laser cavity through the dichroic mirror. The crystal and quartz plates were Brewster angled for the 486 nm light but were not for the second harmonic, since it was polarised orthogonally to the fundamental. The 243 nm beam therefore suffered Fresnel losses of about 19% on leaving the crystal and approximately 13% at each face of the upper quartz plate. This problem was overcome by the design of a new crystal mount in which the BBO crystal was immediately followed by a beamsplitter [50]. This was designed by Mr. G.H. Woodman and built in the Clarendon Laboratory Workshop. It is shown schematically in Fig. 5.9. The beamsplitter allowed the 486 nm beam to pass through while reflecting the 243 nm beam (the reflectivity at 243 nm was 97%) down towards a mirror, which directed the beam out of the laser. Because the UV no longer passed through the dichroic mirror (which had a power for transmitted light of ~ 12), it emerged from the laser with somewhat altered characteristics. The modified optical path used to match this beam into the UV enhancement cavity was described in §4.4.

With fresh dye and around 5 W of pump power, a typical UV power was 8 mW. Coumarin 102 laser dye degrades very quickly, so to maintain this kind of power level, it was necessary to change the dye roughly every two days. The power and stability of the dye laser were greatly improved by keeping the dye cool (it tends to be heated by the circulator pump). The circulator contains a heat exchanger which facilitates cooling by mains water. An improved system was constructed for the frequency doubled laser involving a commercial beer cooler. This device used a reservoir of

iced water containing a heat exchanger to cool water which was being pumped by a commercial shower pump around a closed loop system. This water cooled the laser dye by means of a home-made heat exchanger. The dye reached a temperature of around 4°C.

A perpetual cause for concern in this experiment was the performance of the violet option krypton ion pump lasers (there were two of these—the second pumped the Balmer-β laser). These lasers are specified by the manufacturers for an output of 3 W, but we required around 5 W. Previously, good power output was obtained by disconnecting the automatic gas fill and manually overpressuring the tube. Fortunately, the quality of krypton plasma tubes has improved in recent years and we were able to get the required power without resorting to such measures, but it was always necessary to run the tube at full current (65 A). Krypton ion lasers are inherently less reliable than their argon counterparts; we suffered two plasma tube failures in three years.

Most of the fundamental output of the dye laser was piped across to a second optical table via a monomode, polarisation preserving optical fibre. There, a fraction of the power was split off to go to the wavemeter and the rest went to the locking and scanning system.

5.7 The wavemeter

The wavemeter was described in Boshier's thesis [21]. It was based on the design of Kowalski et al. [51] and consisted of a fringe counting Michelson interferometer with a stabilised helium-neon laser (Fig. 5.10). The corner-cube reflector moved up and down a track of total length 50 cm though in practice only 30 cm was used for fringe counting. This movement gave rise to fringes at each photodiode. The fringes arrived at the photodiodes at the rate of ~100 kHz. Counting accuracy was improved by the use of a phase locked loop which multiplied the frequency of the fringes by 50 while remaining locked to the phase of the input signal from the photodiodes.

The reference HeNe (Spectra-Physics 155) was stabilised by balancing the intensity of two adjacent, orthogonally polarised modes [52]. The optical path between the two cavity mirrors was kept constant by heating the plasma tube to a few degrees above ambient temperature. The stabilisation scheme is shown in Fig. 5.11. The linewidth of the HeNe was approximately 10 MHz.

The wavemeter could be operated in two different modes. In "manual" mode, the experimenter started the fringe counters attached to each photodiode. Both would stop when the one on D_{HeNe} reached a preset value (N_{HeNe}). In this time, the other counter would have seen a number of dye laser fringes N_{dye}. The two fringe counts are related by

$$N_{dye} = N_{HeNe} \frac{n_{dye}\nu_{dye}}{n_{HeNe}\nu_{HeNe}} \tag{5.2}$$

where ν_{HeNe}, ν_{dye} are the frequencies of the two lasers in GHz and n_{HeNe}, n_{dye} are the

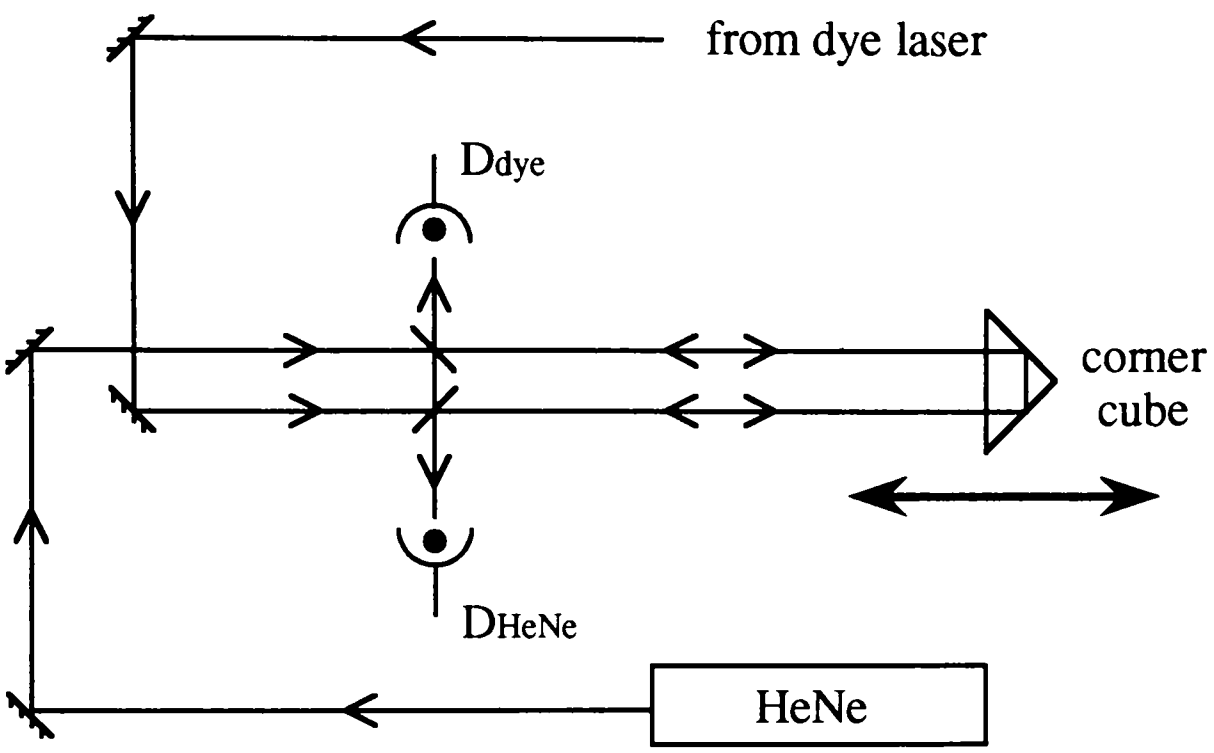


Figure 5.10: The wavemeter.

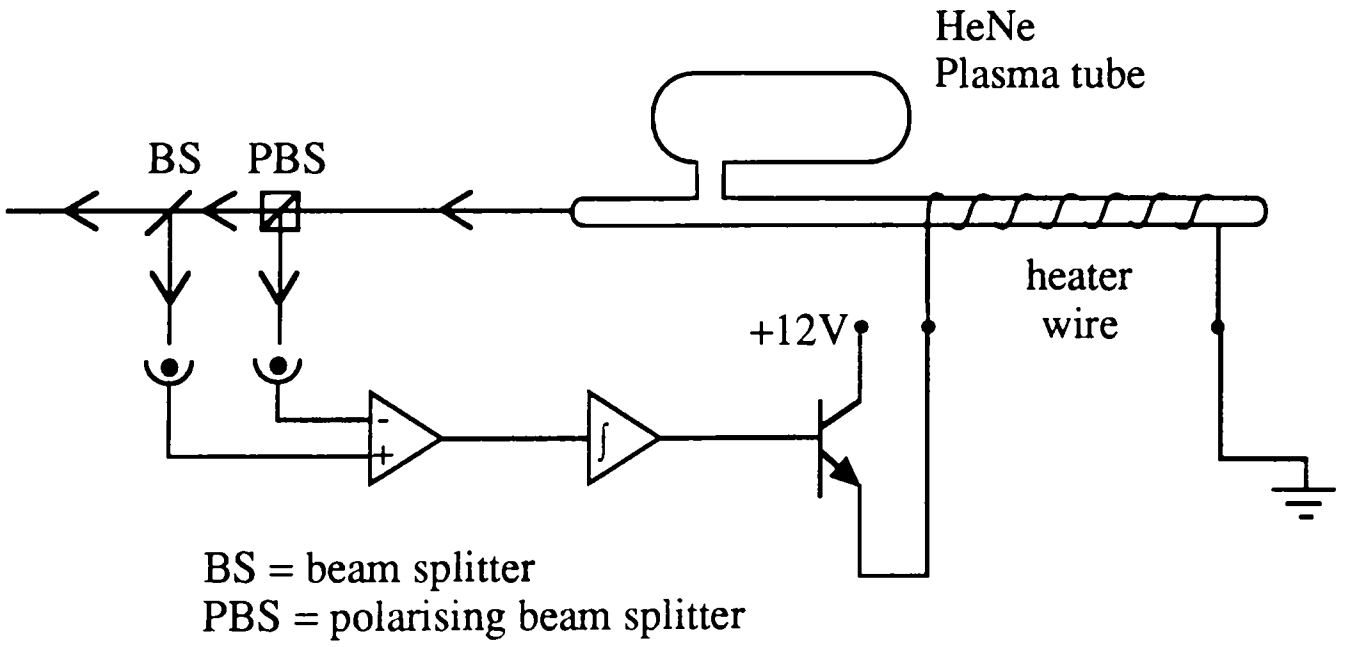


Figure 5.11: The stabilisation scheme for the reference HeNe.

refractive indices of air at 633 nm and 486 nm respectively. Now if N_{HeNe} is chosen so that

$$N_{HeNe} = \frac{n_{HeNe}}{n_{dye}} \nu_{HeNe} \tag{5.3}$$

then N_{dye} will be equal to ν_{dye} (in GHz). N_{HeNe} is set on the thumbwheel display on the front of the wavemeter control box, and N_{dye} was shown on the LED display. In "manual" mode, the frequency of the dye laser was given with an accuracy of 20 MHz. There was an alternative mode of operation ("free run") in which the counter on D_{HeNe} ran until it reached a value of $0.1 \times N_{HeNe}$. The accuracy in this case was 200 MHz. However, this mode gave a reading every second so it was useful for tuning the laser roughly to the correct frequency. "Manual" mode was necessary for the final adjustments.

The reference HeNe had been previously calibrated [21] against an iodine stabilised standard HeNe. Based on this calibration, we expected the 1S–2S signal to appear at a wavemeter reading of 616515.27 GHz provided that the thumbwheel setting (N_{HeNe}) was 47361113. In fact, the signal appeared at a reading of 616515.33 GHz.

5.8 The locking and scanning system

The laser was locked to a stabilised optical cavity by the method of Hänsch and Couillaud [53]. The frequency of the laser could be swept over a small range (~30 MHz) using an acousto-optic modulator (AOM). The principle of the system is outlined here: more details are given in Woodman's thesis [50].

The cavity to which the laser was locked had a 25 cm long Zerodur spacer and 30 cm radius of curvature mirrors. The free spectral range was 600 MHz. It was contained within a temperature stabilised and evacuated housing. To make it suitable for use with the Hänsch-Couillaud system, a Brewster angled thin glass plate was inserted into the spacer. The effect of this was to render the cavity extremely lossy for light of one linear polarisation, while leaving the orthogonal linear polarisation almost unaffected. With the Brewster plate in place, the finesse of the cavity was approximately 30.

The Hänsch-Couillaud locking scheme operated as follows (Fig. 5.12). Light linearly polarised at approximately 45° to the transmission axis of the intra-cavity polariser was directed into the cavity. This light could be resolved into two orthogonal linearly polarised components. One of these was parallel to the transmission axis of the intra-cavity polariser and saw a relatively low loss. The perpendicular component on the other hand saw a very high loss and was simply reflected out of the cavity. There was in general a phase difference between these two components, which made the light reflected from the cavity elliptically polarised. At resonance however, the two components were in phase and the reflected light was linearly polarised (but rotated). So, ellipticity indicated that the light was off resonance and the handedness

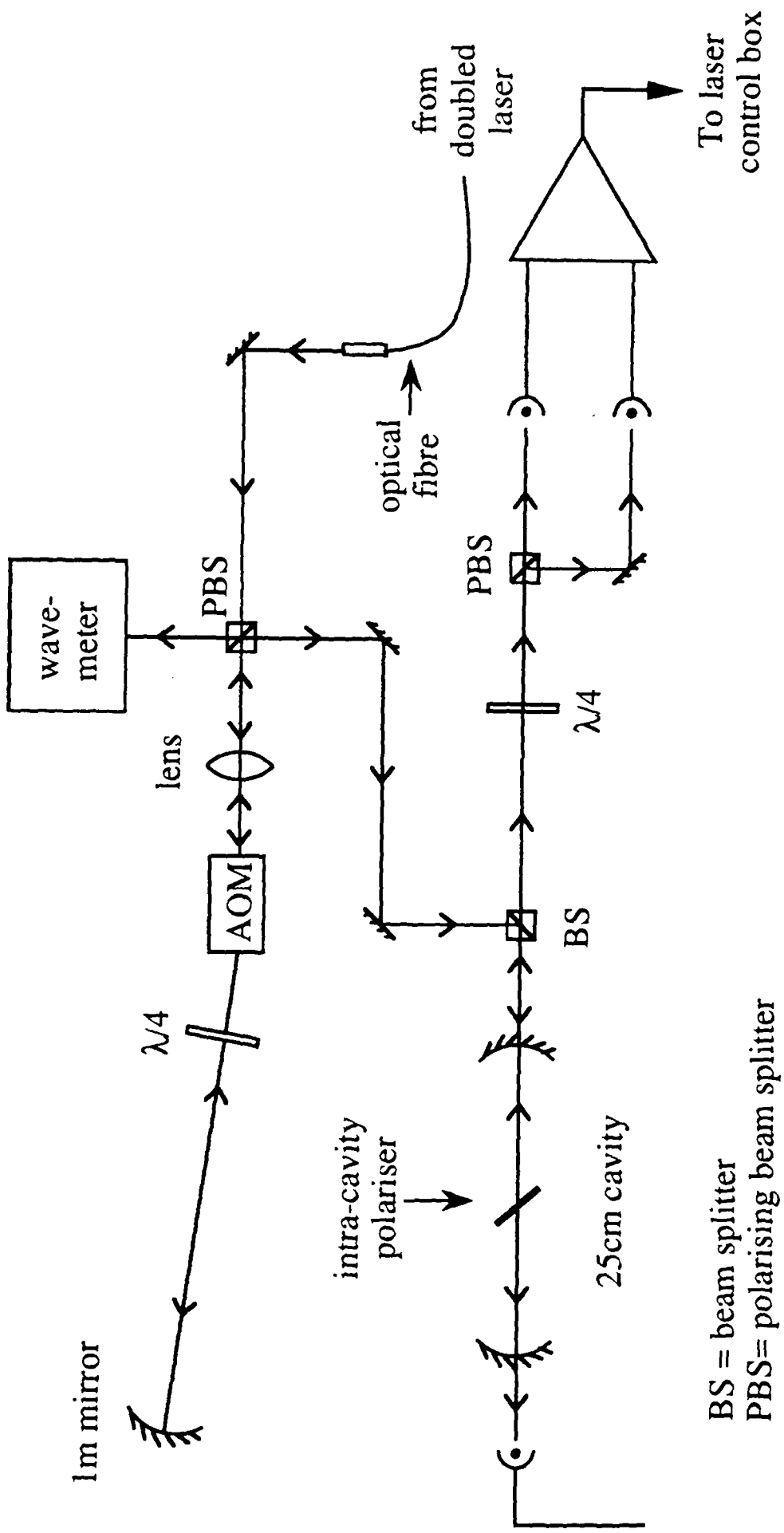


Figure 5.12: The Hänsch-Couillaud locking and AOM scanning system.

gave the sign of the detuning. A full mathematical analysis of this system is given in [53].

The ellipticity was detected with a quarter-wave plate followed by a polarising beam splitter. The quarter-wave plate decomposed the elliptical light into orthogonal linear components of unequal amplitudes. These were separated by the polarising beam splitter and sent to two different photodiodes. The difference in the signals at the two photodiodes gave rise to a dispersion shaped error signal which was used to lock the laser to the cavity. The Hänsch-Couillaud error signal was fed into the laser control box where it effectively replaced the normal error signal, derived from the laser's own reference cavity using the side-of-fringe technique.

An acousto-optic modulator (AOM) was incorporated into the beam path before the 25 cm cavity (Fig 5.12). The AOM was driven by a signal generator (Marconi Instruments 2019A) via an rf amplifier. The centre frequency of the AOM was 200 MHz and its range was 125–250 MHz. A spherical mirror (radius of curvature 1.05 m) was placed at a distance equal to its radius of curvature away from the AOM in order to reflect the frequency-shifted light back for a second pass through the AOM. The quarter-wave plate between the AOM and the 1 m mirror ensured that the beam (which was linearly polarised on entering the AOM) was rotated through 90°after it passed through the AOM for the second time and could therefore be picked off using a polarising beamsplitter as shown in Fig. 5.12. Because of the double pass, the beam was shifted in frequency twice and the total range was 250–500 MHz. As the free spectral range of the cavity was 600 MHz, there were some regions of frequency which could not be reached by this system. If by any chance the 1S–2S signal happened to fall in one of these "dark regions" (owing to the cavity having drifted), it was possible to get to it by using the second-order diffracted spot from the AOM, thereby doubling the range once again but at the expense of power.

5.9 Locating and scanning the 1S–2S resonance

The procedure for locating and scanning over the 1S–2S resonance involved both the laser's own internal scan facility and the AOM scan described above. The principle is illustrated in Fig 5.13. Firstly, the laser was tuned to the correct frequency with the aid of the wavemeter. The UV output was optimised and the enhancement cavity locked. The laser was then scanned with its own control box (set to "internal") over about 300 MHz centred on the correct frequency. Meanwhile, the count rate from the photomultiplier was monitored on a chart recorder. The point during the laser scan when the signal appeared was noted. The laser control was then set to "manual" and its frequency adjusted back to that point, where the signal would appear again. Very small adjustments to the frequency were made with the manual control to keep the laser on resonance.

At this point, the position of the 1S–2S signal (or, more precisely, one quarter of the 1S–2S frequency) relative to a peak of the 25 cm cavity was determined by ad-

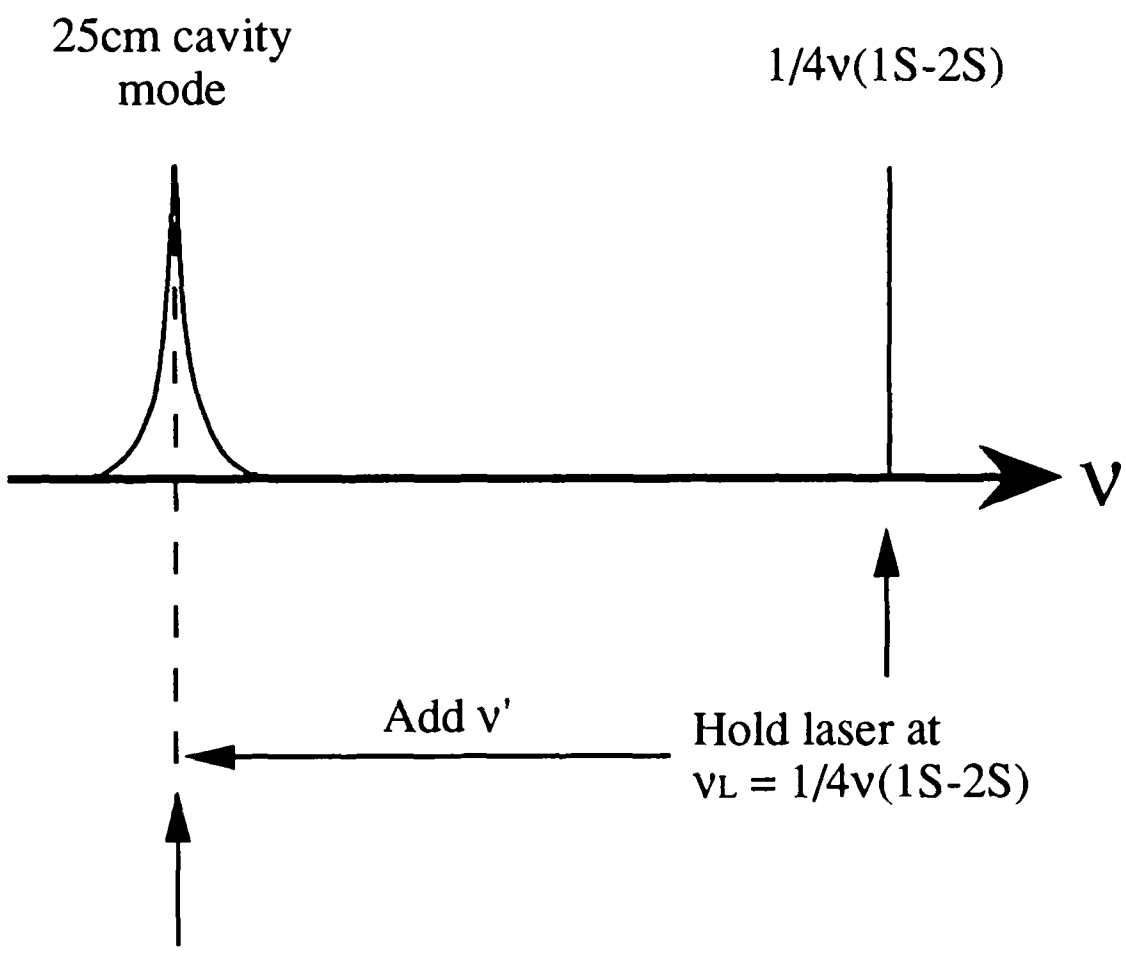


Figure 5.13: The method of scanning the laser over the 1S–2S transition using the AOM.

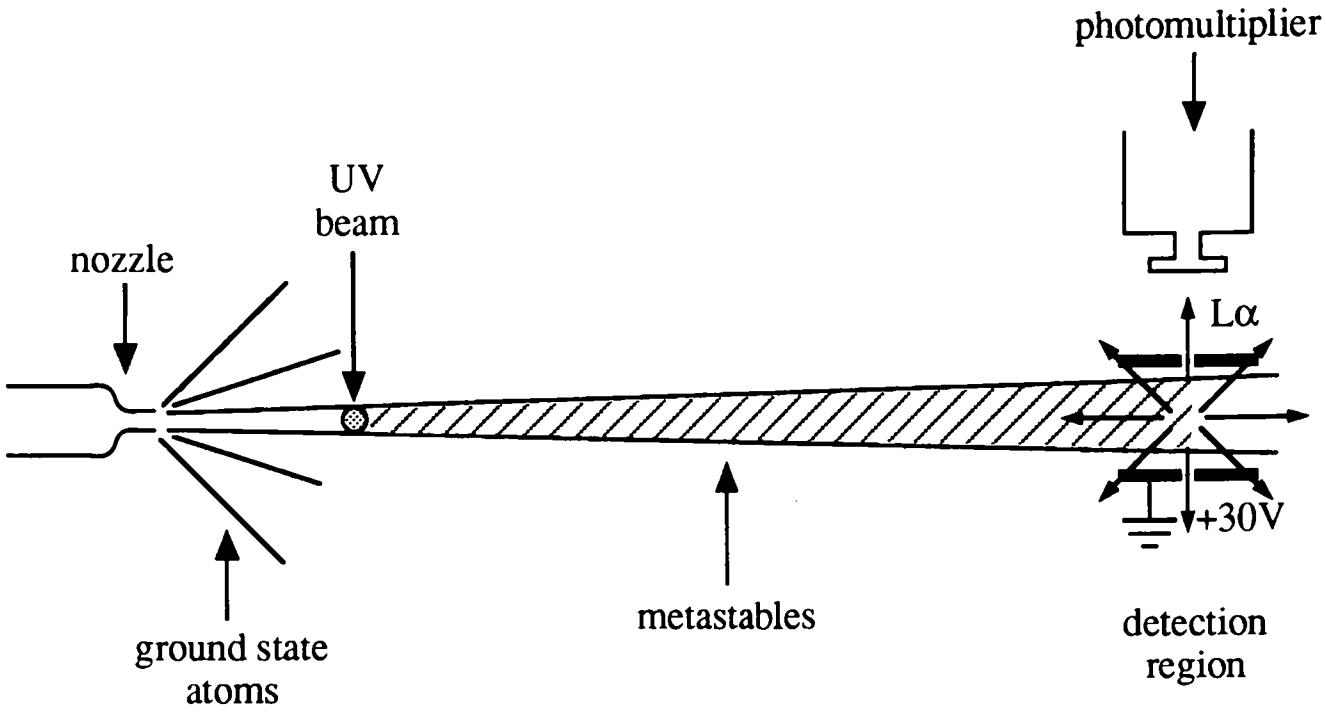


Figure 5.14: The optically excited metastable beam.

justing the AOM frequency to bring the shifted beam on to resonance with the cavity. Call this AOM frequency ν'. The laser control was then turned to "external" and the shifted beam locked to that peak. Sending the frequency ν' to the AOM brought the laser back on resonance with 1S–2S. The laser was scanned under computer control over the 1S–2S transition by scanning the AOM frequency over a small range (about 10 MHz) centred on ν'.

5.10 The metastable beam

In early work, the 1S–2S transition was excited in "cell mode". The first step towards "beam mode" conditions involved pumping with the turbopump and installing the quench wires below the photomultiplier. At first, the photomultiplier remained over the interaction region and wires were wrapped around the enhancement cavity to provide the Stark quenching.

Once the 1S–2S signal had been observed in this way, the detection system (of photomultiplier plus quench wires) was moved 8 cm downstream. Pumping with the turbopump gave a chamber pressure of 4×10^{-5} mbar with 0.4 Torr in the discharge region. The detection system was in the same vacuum can as the UV cavity (box 1) so the Lyman-α filter remained in place.

The 1S–2S excitation generated a ribbon-shaped beam of metastable atoms for which the 243 nm beam acted as a collimating slit approximately 200 μm across—the waist of the UV beam having a radius of $\sim$100 μm (Fig. 5.14). The term "collimation" is used here to mean the ratio of the collimating slit width to the distance between

it and the hydrogen nozzle. In the above-mentioned early beam mode work, the nozzle was 5 mm from the UV beam, giving a collimation of around 1 in 25. Further improvements in collimation were deemed necessary in order to achieve a reasonable linewidth (~100 MHz) on the Balmer-β excitation (Chapter 6). A collimation of 1 in 100 was achieved by drawing the nozzle back to 20 mm from the UV beam. With the same pressures as above, and with around 50 mW of circulating UV, the size of the observed 1S–2S signal was $\sim 10^3$ counts s^{-1} on a background (largely due to scattered UV) of a few hundred counts s^{-1} [54]. Table 3.2 gives for these conditions ($R = 0.1$ m and $P_2 = 4 \times 10^{-5}$ mbar) a predicted signal rate of 9000 counts s^{-1} *without* the Lyman-α filter in place. This should be reduced by about a factor of three to account for it being there (§3.7.3).

The next step was to move the detection region into box 2 (a a distance of 40 cm from the interaction region) and remove the Lyman-α filter to improve the size of the observed signal. It proved impossible to observe the 1S–2S signal with this configuration if only the turbopump were used—the background pressure was too high and too many of the metastable atoms were lost by collisions with stray atoms before they reached the quench wires. It was therefore necessary to reduce the background pressure by the use of the cryopump. This measure resulted in pressures of $\sim 1.2 \times 10^{-5}$ mbar with 0.4 Torr in the discharge region.

Table 3.2 predicts a signal of 140 counts s^{-1} for $R = 0.42$ m and turbopumped conditions. This is probably an optimistic estimate. The UV background with the photomultiplier in this position was ~2 counts s^{-1} per mW of circulating UV (§4.9). ie. around 100 counts s^{-1} with 50 mW. In contrast, if one looks at cryopumped conditions ($P_2 = 1.2 \times 10^{-5}$ mbar, Table 3.2 predicts a signal rate ten times larger while the UV background of course stays the same. Experimentally, we observed signals of around 250 counts s^{-1} on a background of 100 counts $s^{-1}$with a circulating UV power of 80 mW [55]. Scaling the result of Table 3.2 by the square of the UV power gives a predicted signal rate of 3800 counts s^{-1}. The discrepancy between this number and our observed signal rate can be accounted for by a dissociation fraction of less than 100% or a horizontal spreading of the metastable beam which meant that not all the excited atoms entered the detection region. If it is assumed that the true signal under turbopumped conditions was also ten times smaller than that predicted by table 3.2, it becomes obvious why it was impossible to observe, given the background.

Chapter 6

The Balmer-β excitation

6.1 Introduction

The preceding three chapters have described the excitation of the 1S–2S two-photon transition in an atomic beam environment. This process generates an optically excited beam of metastable (2S) hydrogen atoms, collimated by the 243 nm laser beam. This metastable beam was used in the second part of the experiment—namely the comparison of one quarter of the 1S–2S transition frequency with that of a component of Balmer-β. As described in Chapter 1, we had decided to concentrate our efforts in the first instance on the single photon 2S–4P transition, with the aim of demonstrating the feasibility of such an experiment rather than attempting a high precision measurement using 2S–4S which is a longer term objective. This chapter covers the excitation of 2S–4P in the metastable beam and the experimental procedure developed to determine the frequency difference δ calculated in Chapter 2. The data analysis is described in Chapter 7.

To excite the 2S–4P transition, a laser beam at 486 nm (from a second ring dye laser) was incident transversely on the metastable beam. The resonance appeared as a depletion in the number of metastables reaching the detection region. This process is referred to as "optical quenching" of the metastable beam. This chapter begins with a calculation of the conditions required to obtain a good 2S–4P signal, ie. one giving rise to a large depletion in the metastable count rate. The width of the observed signal depends largely on transverse Doppler broadening, the magnitude of which is determined by the collimation of the metastable beam. The chapter continues with a description of the apparatus required for this part of the experiment and concludes with a summary of the performance of the whole system.

6.2 Residual Doppler width and collimation

The room temperature Doppler width of 2S–4P is approximately 8 GHz. We were able to get down to a residual Doppler width of around 100 MHz by collimating the

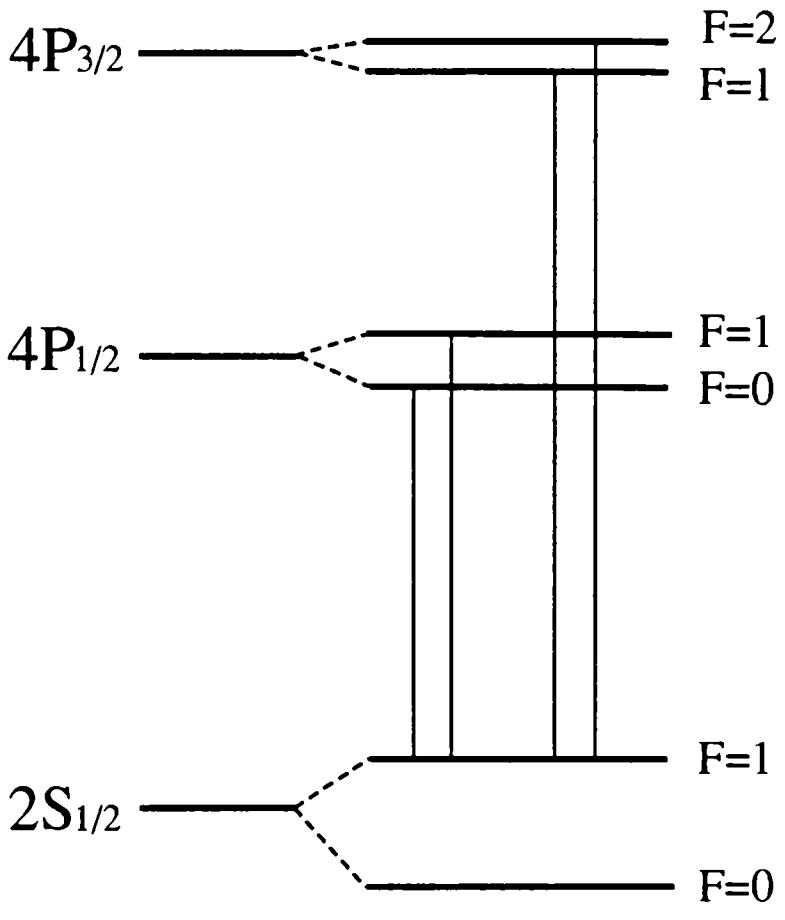


Figure 6.1: The relevant hydrogen energy levels for the Balmer-β excitation (not to scale).

metastable beam. The collimation required to do this was 1 in 100 (see §5.10 for an explanation of the term "collimation"). The best collimation achievable with our apparatus without introducing further apertures along the metastable beam was 1 in 100. Aperturing the beam would have reduced the metastable count rate at the detection region and was therefore not adopted in this pilot experiment.

6.3 Estimate of the 2S–4P signal

6.3.1 The transition probability

Fig. 6.1 shows the hydrogen energy levels involved in this part of the experiment. Throughout this work, we excited only the stronger hyperfine component of 1S–2S, ie. $F = 1 \rightarrow F' = 1$ (§3.4). This meant that only the upper hyperfine level of $2S_{1/2}$ was populated in the metastable beam. We assume that the magnetic sublevels are equally populated. The transition to 4P was excited with linearly polarised light. The experimental parameters which had to be chosen were the power incident on the atoms, the size of the illuminated region and the divergence of the light beam. The aim was to cause as many of the metastables as possible to be transferred to the 4P level during their transit through the laser beam while not broadening the observed resonance significantly beyond the limit set by the collimation.

First, it is necessary to calculate the transition probability as a function of laser

intensity for each of the transitions shown in Fig. 6.1. We assume that the transition is unsaturated. The transition probability for absorption from a plane polarised, collimated laser beam is (see, for example, [35])

$$P_{i\to k} = \frac{\pi e^2}{\epsilon_0 \hbar^2} |< k|z|i >|^2 \int \rho(\omega) g(\omega) d\omega \tag{6.1}$$

where $|i>$ and $|k>$ are non-degenerate states, the light has energy density $\rho(\omega)$ per unit bandwidth and is polarised along z [35]. The atomic response function, $g(\omega)$, is in this case a Lorentzian

$$g(\omega) = \frac{\Gamma/2\pi}{(\omega - \omega_0)^2 + \Gamma^2/4}. \tag{6.2}$$

At line centre $\omega = \omega_0$ and $g(\omega_0) = 2/\pi\Gamma$. We now consider the form of $\rho(\omega)$ for monochromatic light, ie. the case in which the bandwidth of the light is much less than the natural width Γ of the line (13 MHz in this case). We can assume that over a small interval $\delta\omega$ at line centre, $\rho(\omega) = \rho_0$. Then equation 6.1 becomes

$$P_{i\to k} = \frac{2e^2}{\epsilon_0 \hbar^2 \Gamma} |< k|z|i >|^2 \rho_0 \delta\omega. \tag{6.3}$$

Using the relationship between intensity and energy density

$$\mathcal{I} = \frac{\rho_0 \delta\omega}{c} \tag{6.4}$$

the above becomes

$$P_{i\to k} = \frac{2e^2}{\epsilon_0 \hbar^2 c \Gamma} \mathcal{I} |< k|z|i >|^2 . \tag{6.5}$$

We now identify $|i>$ and $|k>$ with the individual magnetic hyperfine sublevels involved in the transition.

$$\begin{aligned} |i> &= |J_l F_l M_F> \\ |k> &= |J_u F_u M_F> \end{aligned} \tag{6.6}$$

Here the subscripts l and u represent the lower and upper levels respectively. The magnetic quantum numbers are the same because of the use of plane polarised light. The fraction of atoms in a given M_F state of the lower level is $1/(2F_l + 1)$. The total transition probability P can therefore be written

$$P = \frac{2e^2}{\epsilon_0 \hbar^2 c} \left(\frac{\mathcal{I}}{\Gamma}\right) \frac{1}{2F_l + 1} \sum_{M_F} |< J_l F_l M_F|z|J_u F_u M_F >|^2 . \tag{6.7}$$

Now,

$$\begin{aligned} \sum_{M_F} |< J_l F_l M_F|z|J_u F_u M_F >|^2 &= \sum_{M_f} \begin{pmatrix} F_l & 1 & F_u \\ -M_F & 0 & M_F \end{pmatrix}^2 |< J_l F_l||\mathbf{r}||J_u F_u >|^2 \\ &= \frac{1}{3} |< J_l F_l||\mathbf{r}||J_u F_u >|^2 \end{aligned} \tag{6.8}$$

by the orthogonality relations of the 3j symbols (see, for example [56]). The squared reduced matrix element may be written

$$|< J_l F_l ||\mathbf{r}|| J_u F_u >|^2 = |< J_l ||\mathbf{r}|| J_u >|^2 (2F_l + 1)(2F_u + 1) \left\{ \begin{array}{ccc} J_l & F_l & I \\ F_u & J_u & 1 \end{array} \right\}^2 \quad (6.9)$$

where I is the nuclear spin. The transition probability then becomes

$$P = \frac{2e^2}{\epsilon_0 \hbar^2 c} \left(\frac{\mathcal{I}}{\Gamma} \right) \frac{2F_u + 1}{3} \left\{ \begin{array}{ccc} J_l & F_l & I \\ F_u & J_u & 1 \end{array} \right\}^2 |< J_l ||\mathbf{r}|| J_u >|^2 . \quad (6.10)$$

The reduced matrix element can be expressed in terms of the Einstein A coefficient using the relationship [56]

$$A = \frac{e^2 \omega_0^3}{3\pi \epsilon_0 \hbar c^3} \frac{1}{2J_u + 1} |< J_l ||\mathbf{r}|| J_u >|^2 . \quad (6.11)$$

This gives

$$P = \frac{2\pi c^3}{\hbar \omega_0^3 c} \left(\frac{\mathcal{I}}{\Gamma} \right) A(2F_u + 1)(2J_u + 1) \left\{ \begin{array}{ccc} J_l & F_l & I \\ F_u & J_u & 1 \end{array} \right\}^2 \quad (6.12)$$

or, converting to Hz,

$$P = \frac{\lambda^3}{4\pi hc} \left(\frac{\mathcal{I}}{\delta \nu} \right) A(2F_u + 1)(2J_u + 1) \left\{ \begin{array}{ccc} J_l & F_l & I \\ F_u & J_u & 1 \end{array} \right\}^2 \quad (6.13)$$

where $\delta\nu$ the linewidth in Hz and λ is the wavelength.

In this experiment, $\lambda = 486$ nm, $\delta\nu = 13$ MHz and $A = 9.668 \times 10^6$ s^{-1}, giving

$$P = 1.09 \times 10^4 (2F_u + 1)(2J_u + 1) \left\{ \begin{array}{ccc} J_l & F_l & I \\ F_u & J_u & 1 \end{array} \right\}^2 \mathcal{I}. \quad (6.14)$$

Now consider the cases of the $2S_{1/2}$-$4P_{1/2}$ and $2S_{1/2}$-$4P_{3/2}$ transitions. In both these cases, $J_l = 1/2$, $F_l = 1$ and $I = 1/2$. The upper F's are not resolved so the total transition probability is equal to the sum of the probabilities for each hyperfine component. In Table 6.1, γ is the combination of angular momentum factors in equation 6.14 and the total transition probability is $P = K\mathcal{I}$.

The relative intensities and therefore the positions of the centres of gravity of the hyperfine components are determined by the fact that only the $F = 1$ level was populated in the metastable beam. The use of linearly polarised light rather than unpolarised light does not further shift the centres of gravity because the linear light in fact accesses one third of the total transition probability for each hyperfine component. This information was used in the calculations of the frequency interval δ in §2.5.

Table 6.1: Transition probability for the hyperfine components of 2S–4P.

J_u	F_u	γ	K ($W^{-1}s^{-1}m^2$)
$\frac{1}{2}$	1	$\frac{2}{3}$	1.09×10^4
	0	$\frac{1}{3}$	
$\frac{3}{2}$	2	$\frac{5}{3}$	2.18×10^4
	1	$\frac{1}{3}$	

6.3.2 Application to this experiment

We first consider the geometry of the input 486 nm laser beam. The metastable beam was ribbon-shaped and approximately 1 cm wide at the position of the 2S–4P interaction region, 32 cm downstream from the UV beam (ie. 8 cm before the quench wires). The Balmer-β laser beam entered the vacuum chamber through a window (5 cm in diameter) in the top flange of the second box. In order that the whole width of the metastable beam be illuminated over roughly the same length, the circular laser spot had a radius r of approximately 1.5 cm (Fig. 6.2). The laser power $\mathcal{P}$ in this beam is

$$\mathcal{P} = \mathcal{I}\pi r^2 \tag{6.15}$$

and the mean transit time t of the atoms through the illuminated patch is

$$t = \frac{2r}{\bar{v}} \tag{6.16}$$

where $\bar{v}$ is the mean atomic speed.

To ensure the maximum possible depletion of the metastable beam, the collimation of the laser beam was matched to that of the atomic beam. Atoms moving with speed v at an angle α to the horizontal have a transverse Doppler shift $kv\sin\alpha$. If an undiverging laser beam intersects the atomic beam at right angles, these atoms will only be on resonance if the magnitude of this transverse Doppler shift is less than the natural width $\delta\nu$ (about 13 MHz in the case of the 2S–4P transition). This condition is satisfied if

$$\left|\frac{v}{c}\sin\alpha\right| < \frac{\delta\nu}{2\nu}. \tag{6.17}$$

In order for all the atoms to contribute to the depletion at line centre, the angular divergence of the laser beam must be such that every atom is on resonance simultaneously. If the (full angle) collimation of the atomic beam is θ, the fraction of the

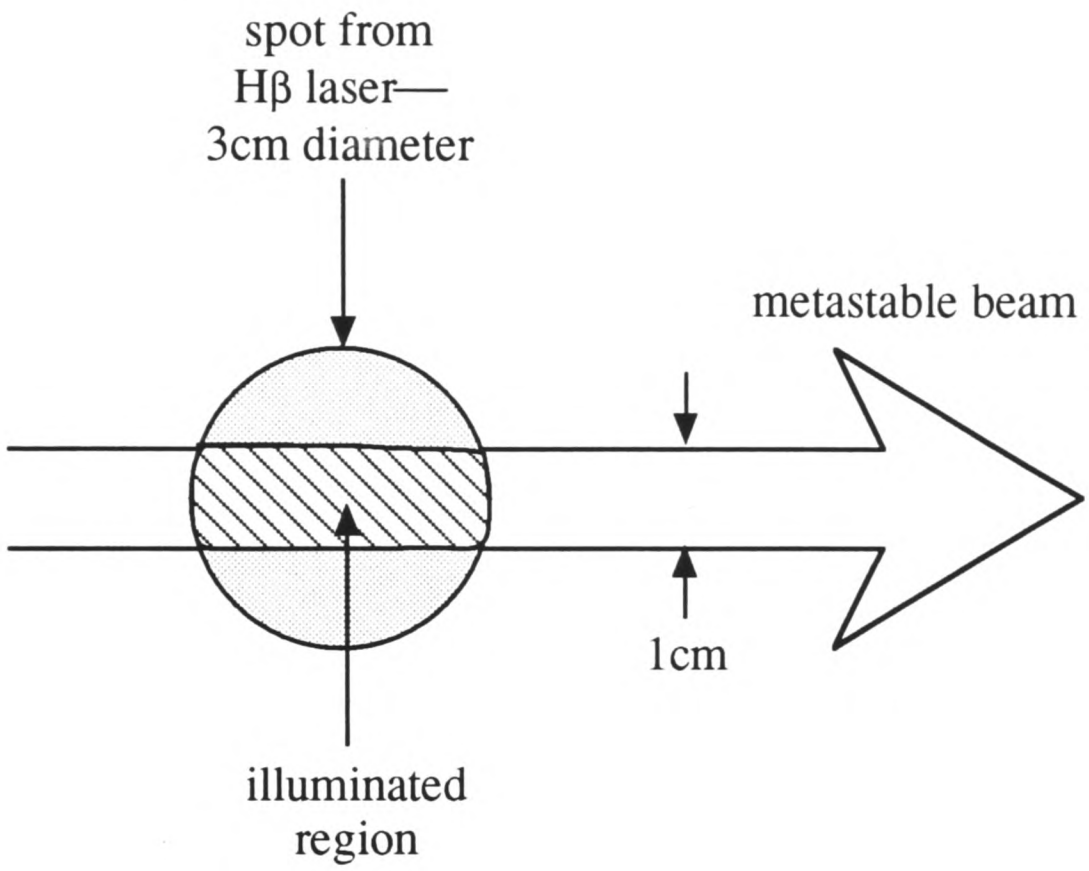


Figure 6.2: The illuminated region of the metastable beam.

time spent by any atom in the illuminated region for which it is on resonance is

$$f = \left[\frac{c}{\bar{v}}\frac{\delta\nu}{\nu}\right]/\theta \tag{6.18}$$

so the intensity $\mathcal{I}$ should be replaced by an effective intensity $\mathcal{I}f$. We required the laser beam to have a divergence of 1 in 100 to match that of the metastable beam (§6.2). The use of a spherical rather than a cylindrical lens to achieve this divergence introduces only second order terms into the final expression for the transition probability and therefore has little affect on the observed signal. A spherical lens system was in fact used in practice (§6.5).

We now turn to the required power. In a time t, the fraction of atoms undergoing a transition is simply

$$1 - \exp(-Pt). \tag{6.19}$$

Using the above expressions for laser power $\mathcal{P}$, effective intensity $\mathcal{I}f$ and transit time t, we obtain for the laser power required to deplete a fraction ϕ of the metastables:

$$\mathcal{P} = \frac{\pi\bar{v}^2 r\theta}{2K\lambda\delta\nu}\ln\frac{1}{1-\phi}. \tag{6.20}$$

The laser power required for approximately 90% depletion of the metastable beam is therefore 38 mW on the $2S_{1/2}$-$4P_{1/2}$ transition and 19 mW on $2S_{1/2}$-$4P_{3/2}$.

Higher laser powers will of course give even greater depletion, but will have relatively little effect on the signal to noise, so these figures were used as our target. We

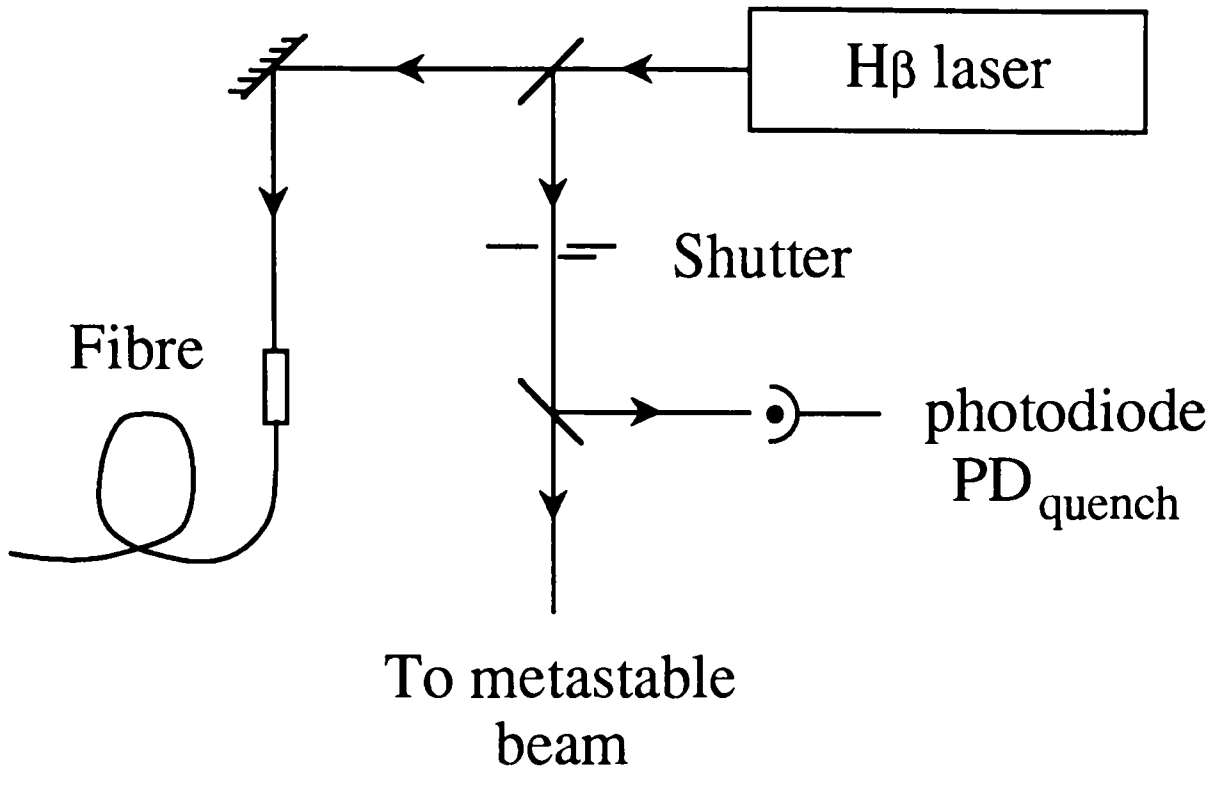


Figure 6.3: The output of the Balmer-β laser.

note that the signal will not be broadened appreciably even if the incident laser power is much higher than this, because the inhomogeneous Doppler width ($\sim$ 100 MHz) completely swamps the natural width (13 MHz). Significantly lower power will decrease the depletion of the metastable beam at line centre and reduce precision.

6.4 The Balmer-β laser

The laser which excited the Balmer-β transition was an unmodified Coherent Radiation CR-699 ring dye laser, operating on Coumarin 102 and pumped by a violet option krypton ion laser. It gave 300 mW at 486 nm with fresh dye and 4.5 W pump power. Most (around 80%) of the output was directed to the Balmer-β interaction region, except for a small fraction which was split off by a beamsplitter to a photodiode. A computer controlled shutter was installed in this beam (Fig. 6.3). The rest of the output went to a monomode optical fibre which transported the light to the wavemeter and 1 m reference cavity on another optical table. The fibre had a transmission of 44%. The laser was locked to its own reference cavity and scanned over the resonance under computer control using the "external" input to its control box.

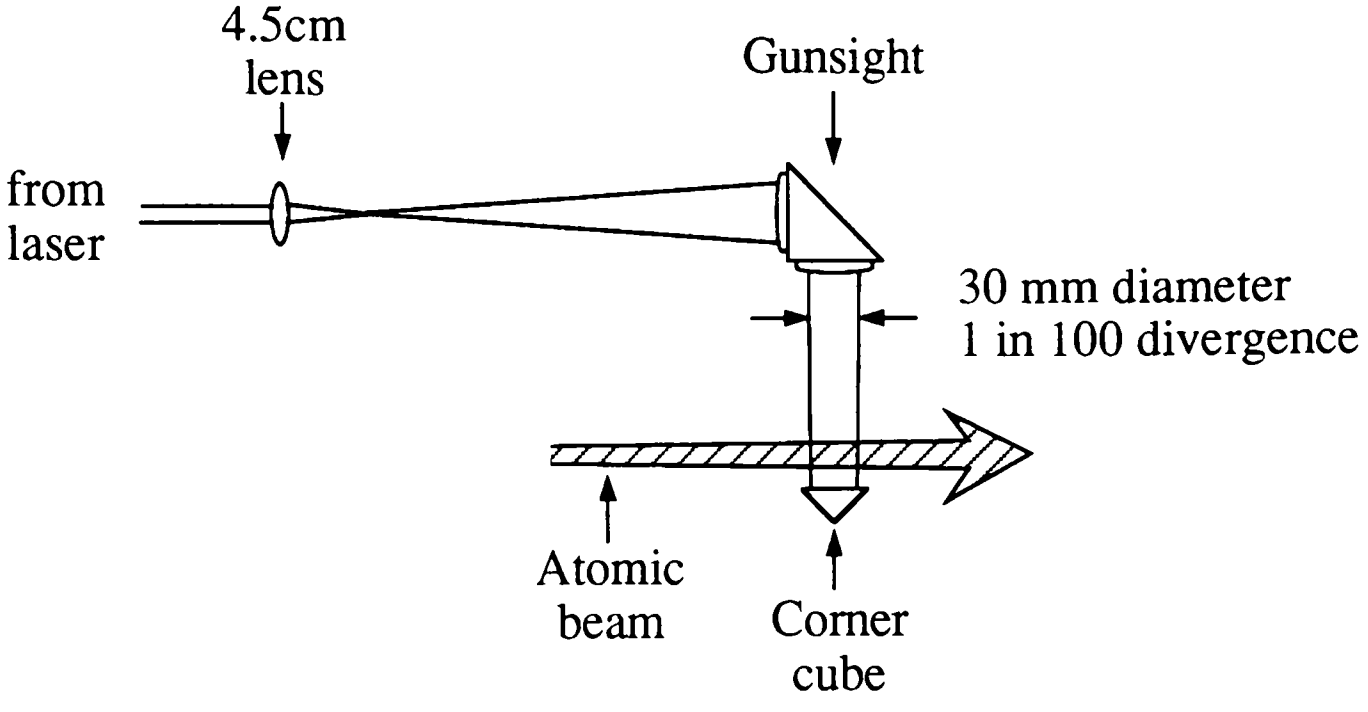


Figure 6.4: The use of the gunsight to give the 486 nm beam the correct divergence.

6.5 The light path to the metastable beam

The 486 nm beam entered the vacuum chamber through a window in the top flange of box 2 (§5.2, Fig. 5.2). As explained above, we required that the laser beam should have a diameter of 3 cm and a divergence of 1 in 100 (Fig. 6.4). In addition, it had to be possible to adjust the tilt of the beam as it entered the chamber, in order to make it as nearly as possible perpendicular to the metastable beam. The necessary adjustments were made possible by using the device shown in Plate II to steer the beam into the chamber. It was part of a tank gunsight, and consisted of a 45° prism with lenses cemented onto the input and output faces, giving it a focal length of 33 cm. It was supported over the window in a mount with three feet (one of which was threaded to provide tilt adjustment).

The total length of the beam path from the laser to the Balmer-β interaction region was 4.6 metres. The beam was directed across the room to the table with the vacuum chamber using mirrors and was enclosed in a beam pipe for safety. For most of its path, the light beam was a few inches above the surfaces of the optical tables. The last few feet were on a platform level with the top of the vacuum can to which the beam had been raised by a periscope. On the platform were a 4.5 cm focal length lens on a translation stage and the final mirror which directed the light across to the gunsight. The laser beam had expanded to a diameter of about 1 cm by the time it reached the platform. The short focal length lens focussed the beam to a small spot, from which it expanded, reaching a diameter of approximately 3 cm at the gunsight. A separation of 38.5 mm between the 4.5 cm lens and gunsight gave the laser beam entering the vacuum can the required 1 in 100 divergence.

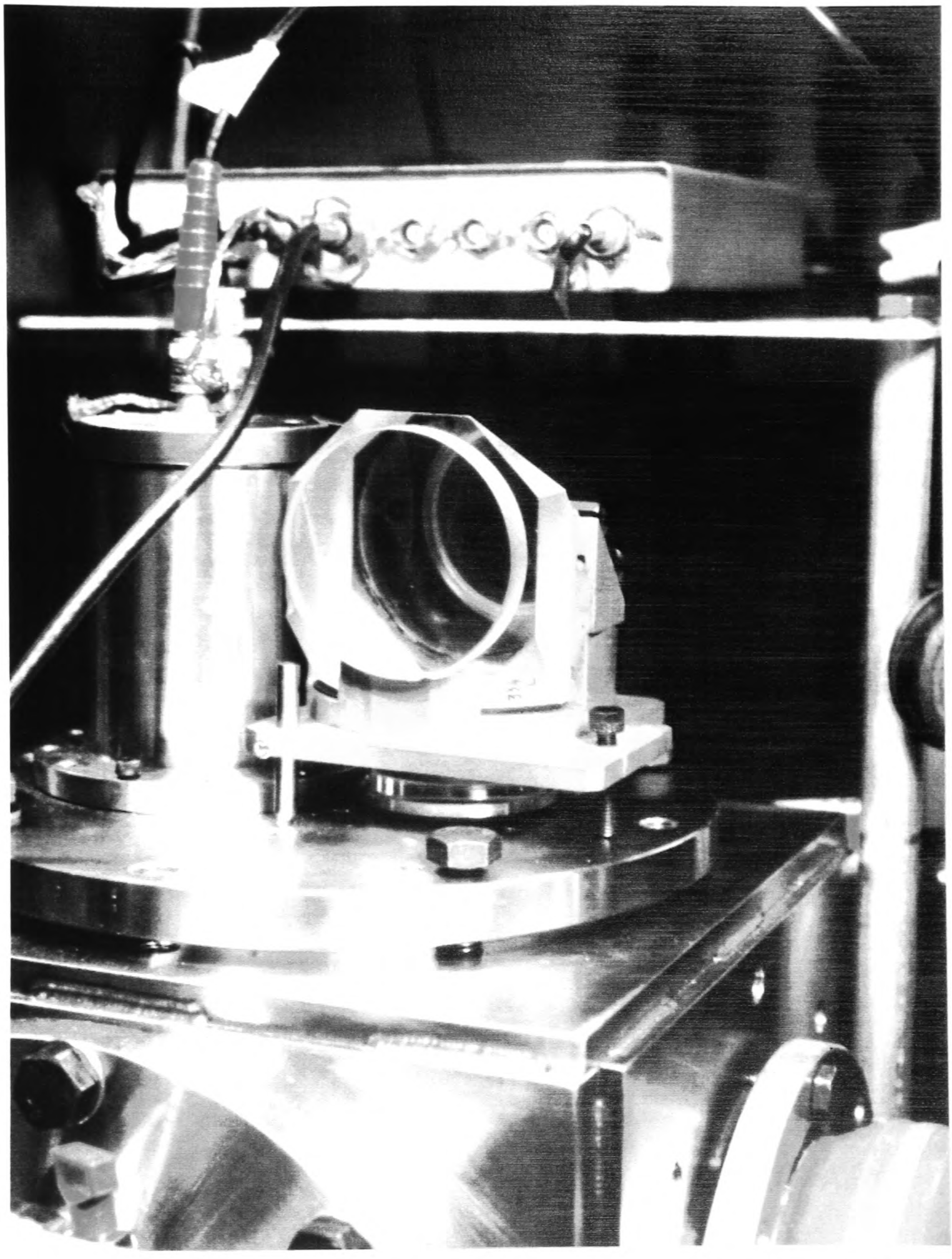


Plate II: The gunsight (in its tiltable mount) in position over the window in the top flange of box 2.

It is obviously difficult to ensure that the laser beam is exactly perpendicular to the metastable beam. If there is some small angle between them, the resonance will be shifted in frequency by some unknown amount. If however, the laser beam is retroreflected back for a second pass through the atomic beam, the backward going beam will also excite the resonance, but this time shifted in the opposite direction by the same amount. The true centre of the resonance can therefore be found. If the laser beam is severely misaligned, this technique will yield two separate resonances, each with the residual Doppler width appropriate to the collimation. If it is only slightly out, the two resonances will overlap and produce apparently one, wider, signal. This latter was in fact the situation in our experiment (see §7.2.2).

A corner cube retroreflector (diameter 38.5 mm, depth 28.5 mm) was positioned approximately 5 mm below the metastable beam to send the laser beam back along its path as described above. The corner cube had been supplied from the manufacturers with a single layer MgF_2 anti-reflection coating on the entry/exit face, which reduced the reflection loss to around 2% on each pass. It was held above the 6" aperture of the turbopump in a mount (designed and constructed by Mr. G.R.K. Quelch) which enabled it to be accurately positioned directly under the input window but did not impair the pumping speed of the turbopump. A 6" base ring rested on top of the turbopump aperture (which was a few millimetres smaller than the hole in the base of the steel box) and was held in place by nylon locking screws. Three posts were attached to the base ring. The cylindrical mount holding the corner cube was attached to the posts by slotted bars. The corner cube holder could be adjusted to the required position and then locked in place by tightening the screws holding the slotted bars to the posts.

The angle of the metastable beam relative to the horizontal axis of the vacuum system was defined by the relative positions of the hydrogen nozzle, UV beam and quench wires. Measurements on these indicated that the beam in fact sloped slightly uphill, at an angle of roughly 2° to the axis of the system. This angle was altered if, for example, the hydrogen nozzle had been translated to improve the 1S–2S signal.

6.6 The wavemeter readings for the Balmer-β excitation

The frequency separations δ between $2S_{1/2}$-$4P_{1/2}$ and $2S_{1/2}$-$4P_{3/2}$ and one quarter of $1S_{1/2}$-$2S_{1/2}$ were calculated in Chapter 2. These values were used to determine the wavemeter readings at which we expected the transitions to be found, given that the 1S–2S transition was found at a reading of 616515.33 GHz (§5.7). The results are shown in Table 6.2.

Table 6.2: Wavemeter readings for the two components of 2S–4P.

Transition	δ (GHz)	Wavemeter reading(GHz)
$2S_{1/2}$-$4P_{1/2}$	4.697	616520.03
$2S_{1/2}$-$4P_{3/2}$	6.069	616521.40

6.7 The 1 metre reference cavity

The frequency difference δ between the fundamental output of the 1S–2S laser and that of the Balmer-β laser was measured using a stabilised reference cavity. It would have been preferable to have used heterodyning techniques to measure the frequency difference between the two lasers directly. Unfortunately, the heterodyne equipment available at the time of the work had a roll-off frequency of 4.5 GHz. We were trying to measure intervals of approximately 4.7 GHz or 6.1 GHz (Chapter 2) so we were forced to use the alternative method described here. As will be seen in Chapter 7, the use of a cavity rather than heterodyning was not the limitation on the final precision of the experiment. The experimental procedure for determining δ is described in §6.8.

The reference cavity had a quartz spacer, the length of which was measured to be 99.979(2) cm. The input mirror was plane and the output mirror had a radius of curvature of 1.673 m. The finesse was approximately 30. A 0.18 mm thick Brewster-angled glass plate had been inserted into this cavity so that it could be used if necessary for the Hänsch-Couillaud locking scheme (§5.8), and since this was not of very high optical quality, it had the effect of degrading the finesse somewhat, even for the polarisation nominally unaffected. The free spectral range of the cavity (allowing for the curvature of the output mirror) would have been 149.922(3) MHz but for the presence of the Brewster plate which reduced it to 149.903(3) MHz. The separation of the higher order transverse modes can be calculated using equation 4.9 to be 0.281 times the free spectral range.

The layout of the optical table with the reference cavity was designed to enable the 486 nm beams from both lasers to be simultaneously aligned with the cavity and wavemeter (Fig. 6.5). One or other was blocked at appropriate stages of the experiment (see below). The total distance from the output of the Balmer-β laser's fibre to the 1 m cavity was 1.5 m. The light emerged from the fibre with a beam diameter of 650 μm. A 1.5 dioptre lens combination (focal length 667 mm) placed 755 mm from the cavity input mirror gave satisfactory mode matching of this beam into the TEM_{00} cavity mode. However, the output of the 1S–2S laser's fibre was 2 m from the reference cavity and the mode matching with the same lens in the same position was less good.

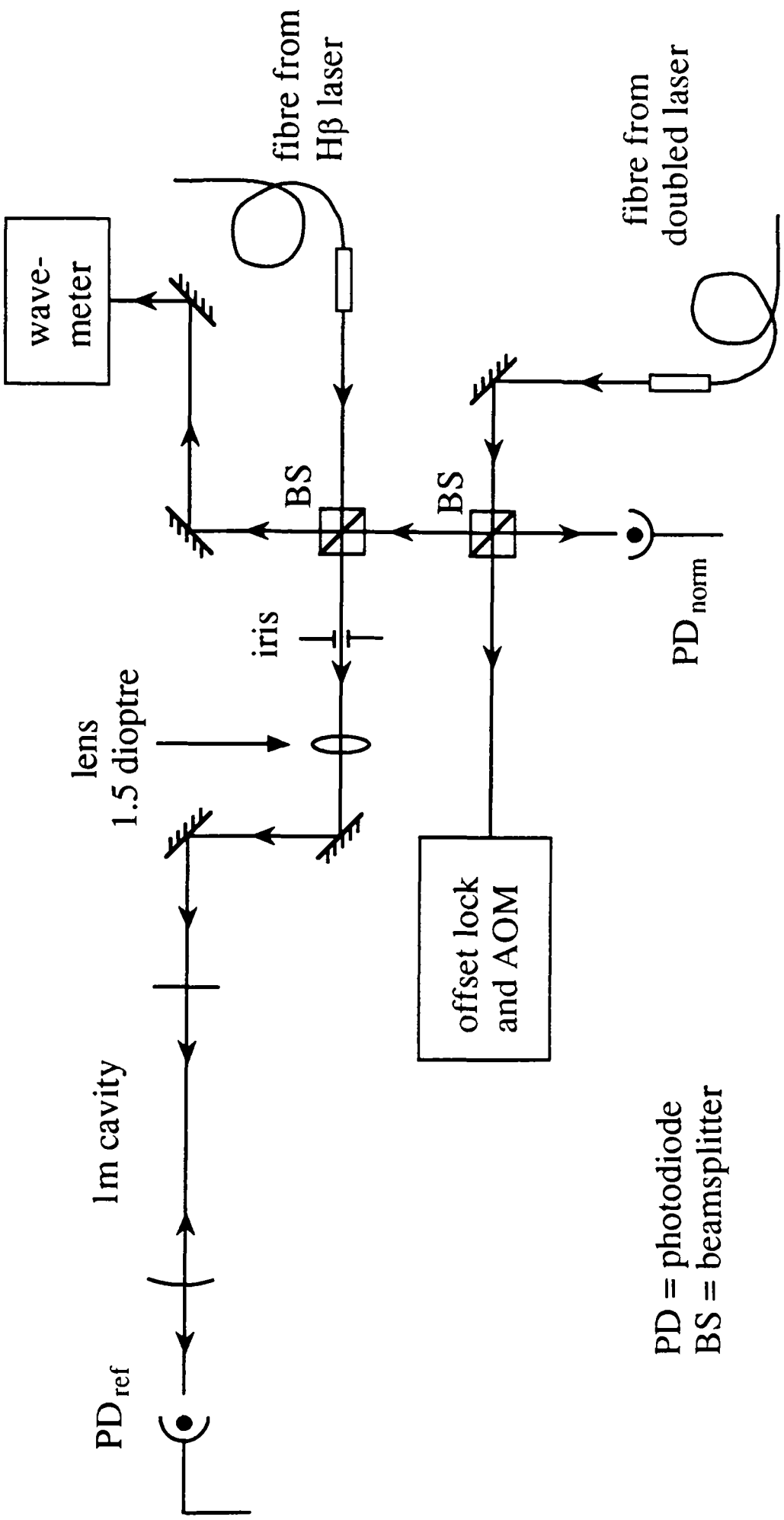


Figure 6.5: The optical layout for the reference cavity and wavemeter.

6.8 Determination of the frequency difference δ

The sequence of events during an experimental run was as follows.

1. The position of the 1S–2S signal relative to a peak of the 25 cm cavity was found as described in §5.9. This was carried out with the Balmer-β laser blocked from the vacuum can, wavemeter and 1 m cavity.

2. The frequency of the doubled laser was set to the centre of the 1S–2S resonance by adjusting the AOM frequency and looking for the maximum metastable count rate. This procedure generated a steady flux of metastables.

3. The 486 nm beam from the doubled laser was then blocked from the wavemeter and 1 m cavity (but *not* from the 25 cm cavity, to which it was locked). The Balmer-β laser was unblocked and tuned to the correct frequency using the wavemeter. This laser was scanned simultaneously over the 2S–4P component and several peaks of the 1 m cavity. The 2S–4P resonance appeared as a depletion in the metastable count rate.

4. The Balmer-β laser was blocked. The doubled laser was scanned with the AOM over the 1S–2S resonance as described in §5.9.

5. The doubled laser was unblocked from the 1 m cavity and the AOM frequency adjusted to bring the laser onto resonance with the nearest peak of that cavity. The laser was scanned with the AOM over this peak. This action determined the frequency separation between $1/4\nu$(1S–2S) and the nearest 1 m cavity mode.

The accuracy of the wavemeter was sufficient to allow us to determine the number of reference cavity modes which lay between 1S–2S and 2S–4P. The frequency difference δ is given by

$$\delta = N \times (\, 149.903(3)\,\mathrm{MHz}) + b - a \tag{6.21}$$

where a and b are the intervals shown in Fig. 6.6. Details of the data analysis are given in Chapter 7.

6.9 The control program

The control and data gathering program was written by Mr. G.H. Woodman. An outline of its function is given here. Further details are given in [50].

The program controlled the Marconi signal generator which drove the AOM, the photon counter and the scanning of the Balmer-β laser. It monitored, through a series of ADCs, the outputs from a number of photodiodes;

- the UV photodiode at the output of the enhancement cavity for the UV power and to check for the cavity jumping off lock (§4.7),

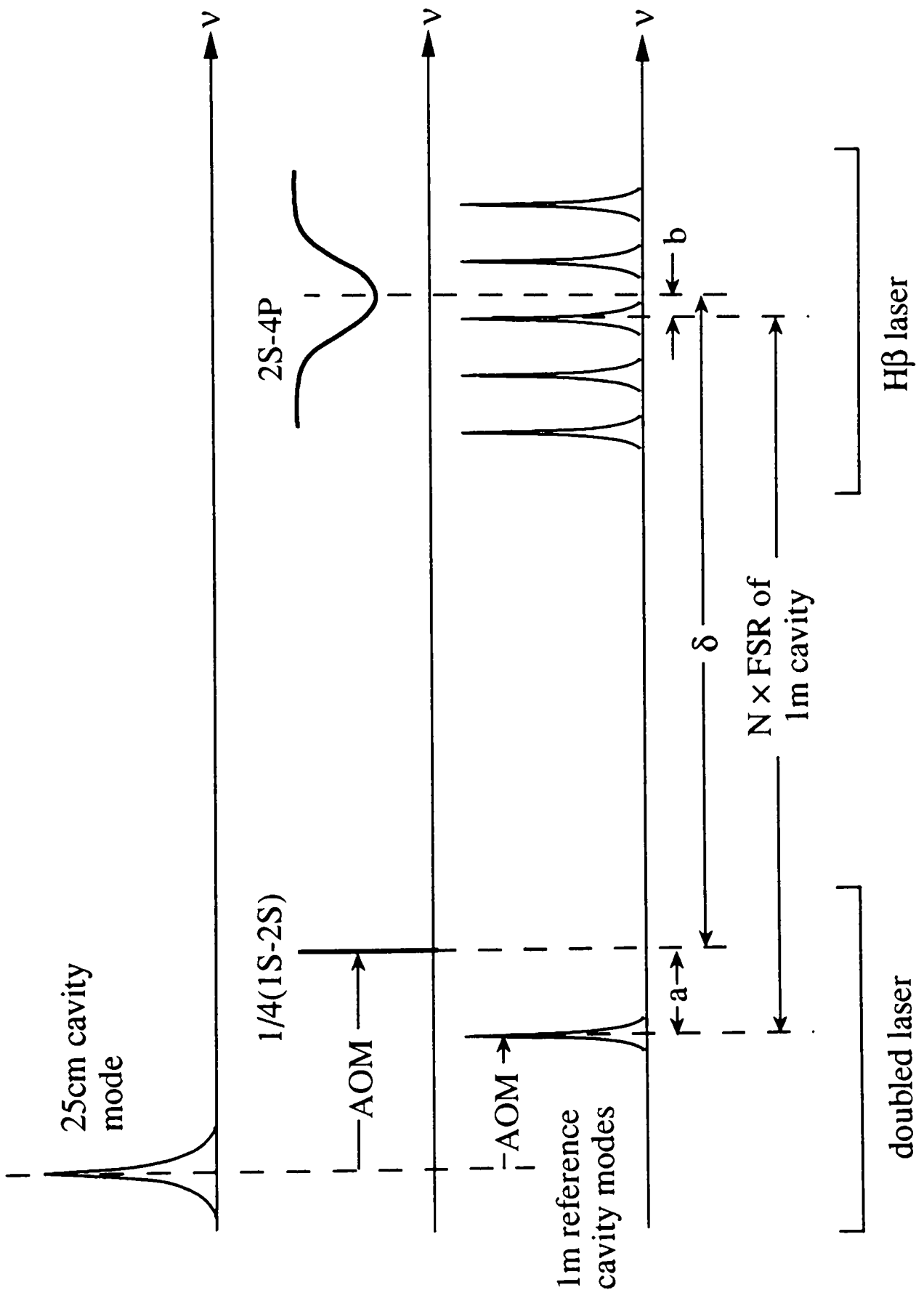


Figure 6.6: The experimental determination of δ.

- the photodiode at the output of the 1 m reference cavity (PD_{ref} in Fig. 6.5),
- the reference fringe normalisation photodiode at the input to the 1 m cavity (PD_{norm} in Fig. 6.5),
- the quench power normalisation photodiode (PD_{qch} in Fig. 6.3),
- an extra photodiode inserted in the Hänsch-Couillaud locking system which checked for the laser dropping off lock.

The outputs of the photodiodes were integrated in averaging filters. The program also recorded the time at the start of each scan—this information was later used to determine the drift rates of the two cavities (see next chapter).

The first option in the program allowed the experimenter to unlock the 1S–2S laser from the 25 cm cavity and take control of the Marconi in order to locate the 1S–2S signal and the nearest reference fringe as described in §5.9 and §6.8. The laser was then locked to the 25 cm cavity and a number of options were available.

"Scan quench" scanned the Balmer-β laser over a given frequency range (chosen by the experimenter and usually around 600 MHz) centred on the 2S–4P resonance, while monitoring the reference fringes and quench power and checking for dropouts. The frequency step between data points was also chosen. The Balmer-β laser was scanned by applying a voltage ramp (via a DAC) to the "external scan" input to the control box.

The time taken to record a single data point (and therefore the total time taken for the scan) was determined by the chosen bin time for the photon counting, which had to be long enough to give an adequate number of metastable counts in each bin. If, for example, the bin time were 0.5 s and the scan width 600 MHz with a frequency step of 2 MHz, there would be 300 data points and a complete scan would take 150 s. During each point, the program would take a reading from each photodiode and then interrogate the photon counter. If the photon counter was not ready with a reading, the program would wait until it had completed its count and then record the final reading. The frequency was then stepped ready for the next point.

The shutter in the quenching beam (§6.5) changed state after a number of data points had been recorded. This number was determined by the chosen "scan range per chop". For example, if the scan range per chop was 20 MHz and the frequency step between points was 2 MHz, the shutter would change state every 10 points. The program paused for 30 ms to allow the shutter to move before proceeding to the next point. The chopping provided information on the background metastable flux. The data were written to an output file *filename*.qch.

"Scan 1S2S" swept the doubled laser over the 1S–2S signal using the AOM and Marconi. The experimenter could choose the width of the scan window, the frequency step between data points and the bin time for the photon counting as above. First, the Marconi was set to the start frequency for the scan over the 1S–2S signal (this was determined from the previously found centre frequency and the chosen scan

width). During the recording of each point, the program would perform a slightly different loop to that described above— it would sample the UV photodiode and then interrogate the photon counter. If the count was not complete, the program would go back and read the photodide again. Once the counting period was finished, the final result was recorded and the UV photodiode readings averaged. Once again, the time for a complete scan was determined by the bin time. A typical scan over 7 MHz with a frequency step of 0.1 MHz and a bin time of 1 s would have 70 points and take 70 s. The output data file was *filename*.sig.

"Scan reference fringe" swept the doubled laser (again using the AOM) over the nearest reference cavity fringe to the 1S–2S signal. The scan window and frequency step were chosen as for the 1S–2S scan. However, the timing was different. This was the only one of the three types of scan which did not involve photon counting, so there was no limitation on its speed. In fact, it was preferable to make this scan as fast as possible, so that the position of the reference fringe would be determined with respect to the 1S–2S transition before the fringe had drifted by an appreciable amount. For this reason, the photodiodes were sampled once at each data point. As above, the start frequency was determined by the chosen scan window and the known centre frequency. The output data file was *filename*.ref.

A complete data set comprised one of each type of scan, all taken within a few minutes of each other.

6.10 Summary

The apparatus described above is shown in Plate III. The photograph shows the two stainless steel boxes which comprised the vacuum chamber. The hydrogen delivery tube and XYZ manipulator can be seen in the foreground. The cryopump is in place on top of box 1. The UV enhancement cavity was supported inside the sidearms of box 1. Also visible in the photograph are the gunsight on top of box 2 and the platform next to box 2 which held the optics used to direct the 486 nm light to the metastable beam. The top of the photomultiplier housing can be seen beyond the gunsight. We were able to obtain a depletion in the metastable count rate of approximately 40% when the Balmer-β laser was tuned to $2S_{1/2}$-$4P_{1/2}$. This is the weaker component of the two. The width of the resonance was 150 MHz; 100 MHz came from the residual Doppler broadening and the remaining width arose from the fact that the laser beam was not exactly perpendicular to the metastable beam (§6.5).

Unfortunately, before any further improvements could be made to the observed signals, a plasma tube failure in the krypton ion laser pumping the doubled dye laser brought the work to a premature end. We had by this stage obtained three complete data sets—the analysis of these and the result for the 1S Lamb shift are presented in the next chapter.

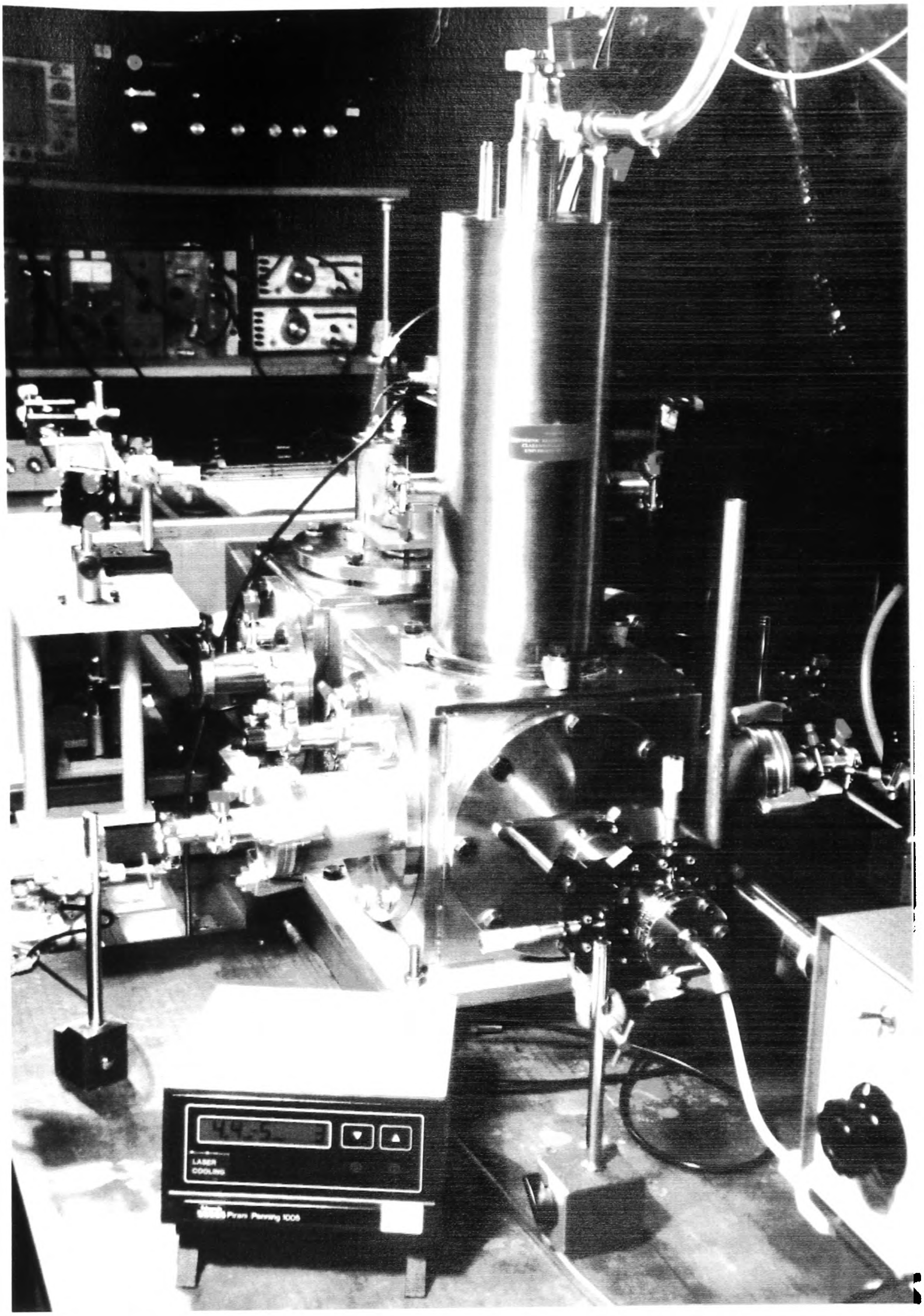


Plate III: An overview of the experimental apparatus.

Chapter 7

Results and analysis

7.1 Introduction

In this chapter, the results of the experiment will be presented. The analysis of the results leading to an experimentally determined value for the 1S Lamb shift will be described.

A complete data set comprised three different types of file, which were described in §6.9. They were:

filename.**qch** These files contained the information on the scan over the 2S–4P transition with the Balmer-β laser (referred to below as "quench data"), plus the reference fringes which were recorded simultaneously.

filename.**sig** These contained the 1S–2S signal in terms of counts s^{-1}, obtained by scanning the doubled laser over the resonance with the AOM.

filename.**ref** These files contained the AOM scan of the doubled laser over the reference fringe nearest to the 1S–2S signal.

As mentioned at the end of the previous chapter, we were only able to obtain three complete data sets which were suitable for a 1S Lamb shift measurement. All of these were based on $2S_{1/2}$–$4P_{1/2}$ as the comparison transition. They were titled *july2f1*, *july2g1* and *july2h1* and will be referred to below as the "f", "g" and "h" data. Another data set *july2e1*—the "e" data—was not suitable for a measurement because the scan over the 2S–4P resonance had shown two obviously separated peaks owing to misalignment of the Balmer-β laser beam (see §6.5). The resonance excited by the input beam was displaced from that excited after reflection from the corner cube. The alignment had been adjusted before recording the other data sets. The "e" data had been recorded approximately half an hour before the other data. Although, this data set was not suitable for use in the determination of the 1S Lamb shift, it did contain useful information on the shape and width of the 2S–4P resonance (§7.2.2) and was also used in the calculation of the reference cavity drift rate (§7.4).

In order to obtain a value for the 1S Lamb shift from the data, it was necessary to find an experimental value of the quantity δ introduced in §1.3 and calculated from theory in §2.5. We recall that, for the purposes of this experiment, δ is the interval between one quarter of the frequency of the $F = 1 \rightarrow F' = 1$ component of 1S–2S and the frequency of the centre of gravity of the 2S–4P resonance, taking into account the fact that only the $F = 1$ state of the lower level was populated. The comparison transition was $2S_{1/2}$–$4P_{1/2}$ for all the data presented here. The relevant theoretical value of δ is therefore that given in Table 2.6. It will be seen below that the observed width of this transition under the conditions of this experiment was of order 100 MHz. The hyperfine structure of $4P_{1/2}$ is 7 MHz which was thus completely unresolved.

The experimental method for obtaining a measurement of δ was described in §6.8 and illustrated in Fig. 6.6. It was shown that, experimentally,

$$\delta = N \times (149.681(3)\ \text{MHz}) + b - a \tag{7.1}$$

where N is an integer, 149.681(3) MHz is the free spectral range of the reference cavity, a is the frequency separation (at 486 nm) of the 1S–2S transition and the nearest reference cavity peak and b is the separation of the centre of gravity of the $2S_{1/2}$–$4P_{1/2}$ transition and the nearest reference cavity peak.

In the analysis which follows, b was obtained from the ".qch" data files (§7.2) and a from the ".sig" and ".ref" files (§7.3). Figs. 7.1 and 7.2 summarise the functions and outputs of the various programs involved. A correction for the drift of the reference cavity was made (§7.4) before equation 7.1 was used to obtain a value for δ, from which the 1S Lamb shift was extracted. All the fitting programs were based on the Levenberg-Marquardt method described in Chapter 14 of "Numerical Recipes" [57].

7.2 2S–4P and reference fringes

This section covers the analysis of the data files *filename*.qch. Four such data files were available for analysis, namely *july2e1*.qch to *july2h1*.qch. As explained above, the "e" data was not used in the calculation of the 1S Lamb shift, but was useful in that it enabled us to determine the true width of the resonance as described below.

The format of the raw data files *filename*.qch is illustrated for the case of *july2f1*.qch in Table 7.1. The ".qch" data files had 300 data points and contained the information on the 2S–4P transition in the form of metastable counts per bin. The shutter described in §6.4 had changed state every 10 points; the first 10 points were taken with the shutter in the beam. The files also contained information on the 1 m cavity fringes (in the channel labelled "Ref. cavity transmission"), recorded simultaneously with the quench signal. The channel "UV power" contained the output from the UV photodiode after the UV enhancement cavity. The quantities "MinRef" and "MinUV" were the minimum photodiode signals for zero transmission of light through these cavities and gave an indication of the zero offset of the averaging filter mentioned in §6.9. In addition, these readings were used by the data gathering program to detect occasions

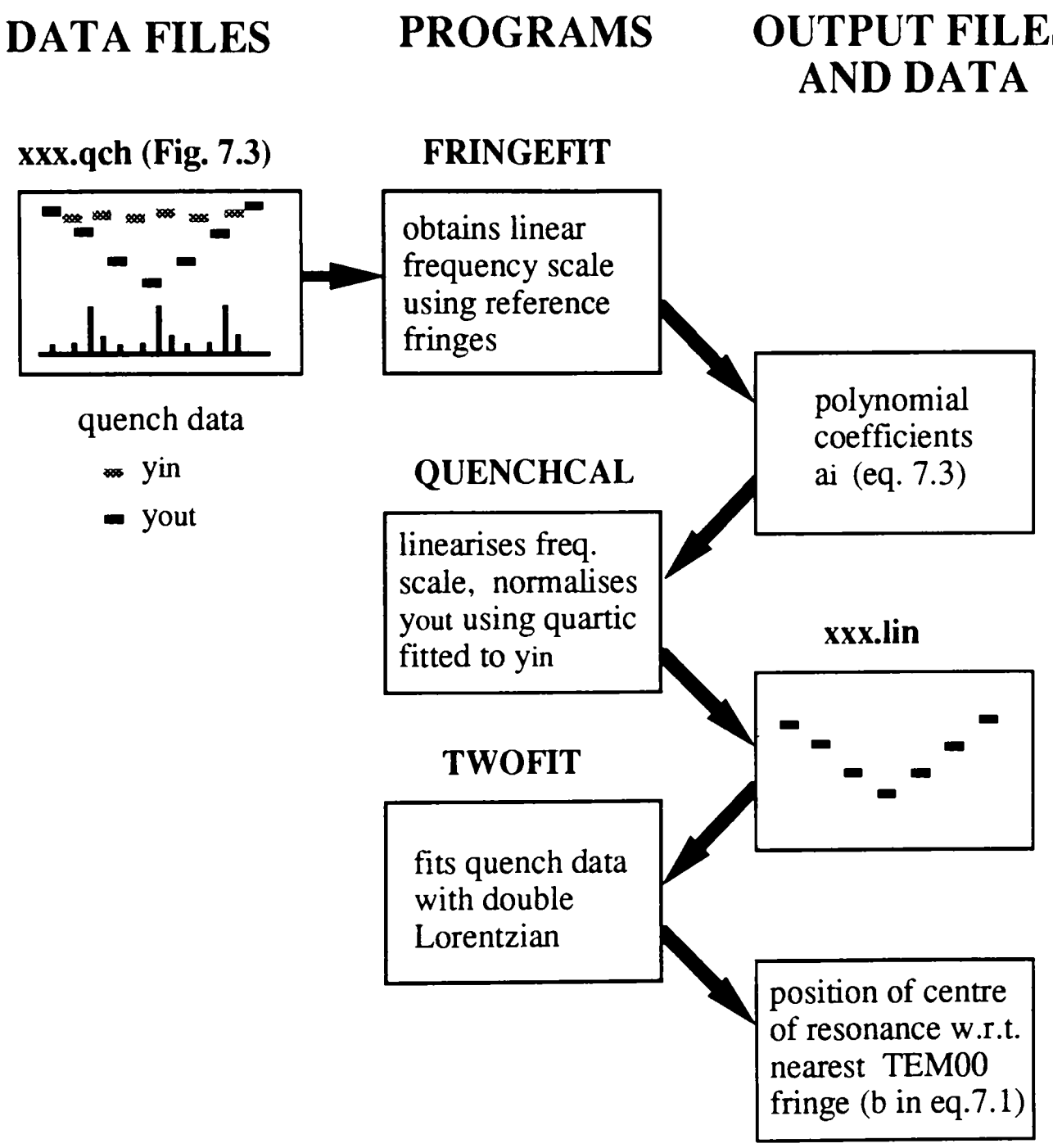


Figure 7.1: Summary of the analysis of the quench data.

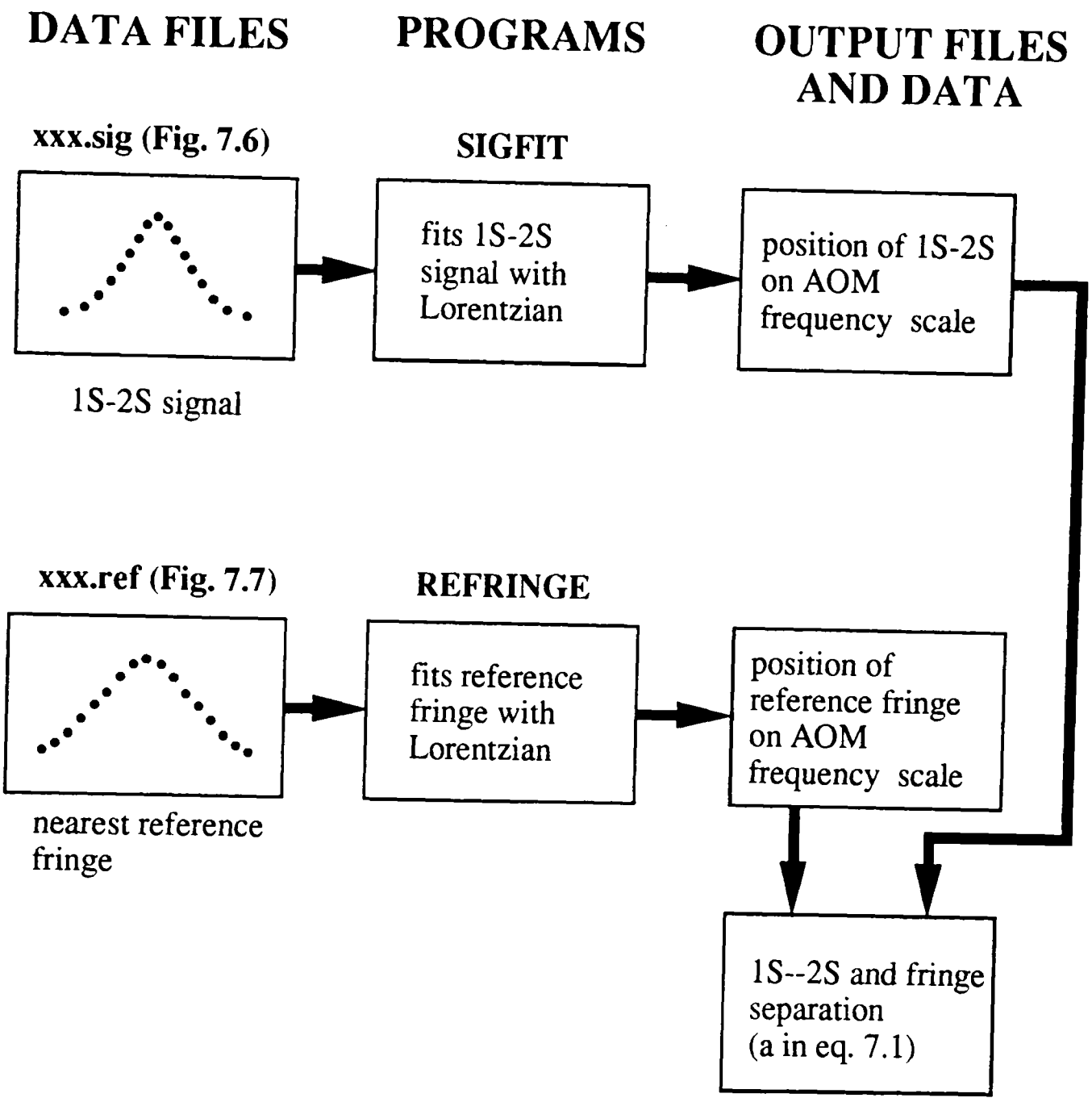


Figure 7.2: Summary of the analysis of the 1S–2S signal and reference fringe data.

Table 7.1: The format of the raw data file *july2f1*.qch.

Start time	19:32:58
No. of points	300
Scan range (MHz)	600
Frequency bin width (MHz)	2
Integration time (ms)	500
Scan range per chop (MHz)	20
MinRef	-901
MinQuench	-894
MinNorm	0
MinUV	-895

Frequency (MHz)	Counts per bin	Ref. cavity transmission	Quench power	Normalisation power	UV power
2	162	-800	-894	-899	-738
4	160	-871	-894	-899	-729
etc.					

when the lasers dropped off lock during a scan. "Normalisation power" and "Quench power" were the outputs from photodiodes monitoring the input power to the reference cavity and the power going to the metastable beam respectively. "MinQuench" and "MinNorm" were background readings from these photodiodes. Unfortunately, the normalisation power photodiode was not working during the experimental runs being considered here. It was therefore not possible to normalise the reference fringes against drifts in the Balmer-β laser power. The quench power readings were not used for this purpose because that photodiode had been positioned before the input to the fibre which transported the light from the Balmer-β laser to the second optical table. There may have been fluctuations in the intensity emerging from the fibre (caused by beam movements at the input) which would not have been detected by the quench power photodiode. In any case, normalisation of the fringes would have made very little difference to the results because of their extreme narrowness.

One of the raw data files is shown in Fig. 7.3. The doubled laser had been tuned to the top of the 1S–2S resonance as described in §6.8 giving a roughly constant metastable count rate at the detection region (upper data). The Balmer-β laser was then scanned across the $2S_{1/2}$-$4P_{1/2}$ resonance, producing a clear dip in the metastable signal. The beam was being chopped every 20 MHz, so the background metastable intensity is known. Fig. 7.3 also shows the reference cavity fringes.

There were two stages to the analysis of these files. First, the reference cavity fringes were used to linearise the frequency scale. This was necessary because the dye laser's internal scan facility was not quite linear. Next, the 2S–4P resonance was converted to this linear frequency scale and normalised against fluctuations in the metastable beam intensity. The linearised, normalised data were then fitted to a suitable function in order to find the position of the centre of the resonance. The precision of the data did not justify a rigorous analysis so no attempt was made to calculate the true lineshape of the resonance. In any case, the fact that the resonance was symmetrical meant that the position of the centre was relatively insensitive to the particular choice of lineshape function. Initially, the data were fitted to a Lorentzian, but, as will be seen below, a better fit was obtained using two displaced Lorentzians. The frequency interval b between the centre of the resonance and the nearest reference fringe was then determined.

7.2.1 Linearisation of the frequency scale

The length of the quartz reference cavity spacer had been measured to be 99.979(2) cm at room temperature (§6.7). The cavity had been stabilised at 40°C—about 10°C higher than room temperature. The expansion coefficient of quartz is approximately $0.4 \times 10^{-6}/°C$ so at the stabilisation temperature the length would have changed by about 4×10^{-6} m, corresponding to a change in the free spectral range of < 1 kHz. The uncertainty in the measured length of the spacer (2 parts in 10^{-5} m) contributes the same fractional uncertainty in the free spectral range (ie. a few kHz). However, as will be seen later, the uncertainty in the final result for δ (and hence the 1S Lamb

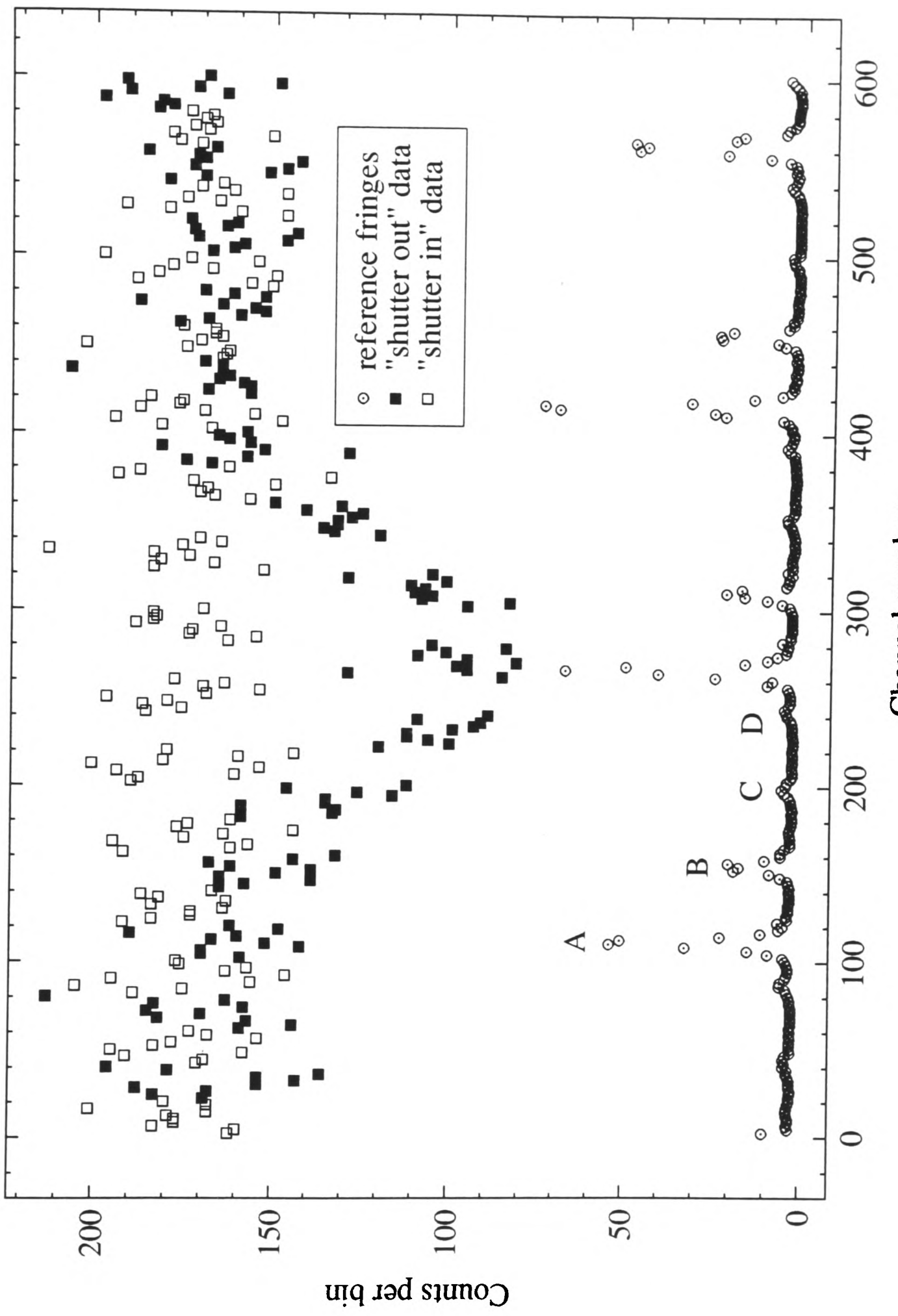


Figure 7.3: The raw quench data from the file *july2f1*.qch. Upper data: metastable counts at the detection region (successive groups of 20 points are with the shutter in and out of the Balmer-β laser beam). Lower data: transmission (in arbitrary units) through the reference cavity during the laser scan.

shift) was 3 orders of magnitude larger than this.

Because of the imperfect mode-matching mentioned in §6.7, there were in fact four peaks per order—the TEM_{00} and three higher order, lower intensity modes. These are labelled A,B,C and D in Fig. 7.3.

The first attempt at linearisation involved fitting individual Lorentzians to each of the peaks, allowing the height, full width at half maximum (FWHM), and position of centre to float. The positions of the centres were thereby found in terms of the channel number (ie. apparent frequency). The frequency separations of the peaks were calculated using the standard results for optical resonators given in §4.3. A quartic was then fitted to the data to give true frequency as a function of channel number. This quartic could be used to linearise the 2S–4P data.

The second version of this procedure involved fitting a series of Lorentzians to all the peaks taken together using the program FRINGEFIT. This program read in from the ".qch" data file: x_i (channel number) and y_i (photodiode response). The function which was fitted was

$$y_i = \sum_{n=1}^{N_F} \frac{P_n}{(q/2)^2 + (z_i - S_n)^2} + \mathcal{B} \tag{7.2}$$

in which only z_i was floated in the fitting process. N_F is the number of fringes in the data file (usually 14). P_n and q are the height and width of each fringe. Reasonable values of these quantities were obtained from the earlier fitting described above. However, P_n was the same for each type of fringe and q was the same for all fringes. Since this corresponds to the real situation it is clearly preferable to the earlier method. The positions of the fringes—in terms of *true* frequency—are S_n and were calculated using equations 4.8 and 4.9. The values of P_n and S_n used in the program FRINGEFIT are given in Table 7.2. The position of the first fringe in each data set (of the "C" type) was arbitrarily set to 100 MHz. The background $\mathcal{B}$ was set to 20 (same units as P_n) and q was 4.2 MHz. The unknown z_i represented true frequency, and was taken to be a cubic function of channel number x_i:

$$z_i = a_1 + a_2 x_i + a_3 {x_i}^2 + a_4 {x_i}^3. \tag{7.3}$$

The coefficients a_i were floated.

To summarise, fitting all the fringes together using FRINGEFIT was considered to be a more satisfactory method of linearisation than dealing with the individual fringes separately. The latter method allowed different widths and heights to be assigned to the fringes and therefore lost information. On the other hand, FRINGEFIT forced all the fringes to have the same width and fringes of the same type to have the same height. Fig. 7.5 shows the fitted reference fringes. The best fit values of the coefficients a_i for each data set were used to put the quench data belonging to that data set on to a linear frequency scale.

Table 7.2: The fringe heights P_n (arbitrary units) and positions S_n (MHz) used in the linearisation program FRINGEFIT.

Fringe	P_n(arb.units)	S_n(MHz)
A	800	165.59
B	200	207.76
C	20	100.00
D	20	142.17

7.2.2 Fitting the 2S–4P data

The first step was to normalise and linearise the data using the program QUENCHCAL. This program took as its input the raw data in the ".qch" files. The metastable counts were first divided by the square of the UV power. Next, the data were put onto the linear frequency scale defined by the a_i from FRINGEFIT. The quench data were then divided into two sets: that obtained with the shutter in the laser beam (x_{in}, y_{in}) and that obtained with the shutter out of the beam (x_{out}, y_{out}), where in each case x represents linearised frequency and y represents metastable counts per second (Fig 7.1).

The "shutter in" data gave the background metastable intensity. After linearisation, the "shutter in" data as a function of true frequency were fitted to a quartic. The "shutter out" data were then divided by this function to normalise out drifts in the metastable flux. The "shutter in" data were also useful in estimating the uncertainties in the 2S–4P data points. The evaluation of the uncertainties on the fitted parameters in the Levenberg-Marquardt program requires a statistical uncertainty to be input on the data points. This could be deduced from the fit itself, assuming that the residuals were entirely statistical. However, it was considered better to use the fit of the "shutter in" data to a quartic as an indicator of the statistical uncertainty in the data points.

The program QUENCHCAL produced output files of the form *j2f1*.lin, which contained the linearised, normalised "shutter out" data (ie. the quench signal itself) plus the estimated uncertainty on each point as calculated above.

The next step was to fit the quench data in order to find the centre of the 2S–4P resonance. Initially, the data were fitted to a single Lorentzian, allowing the position of the centre, FWHM, height and background to float. However, this approach was clearly unsuitable for the "e" data, which contained two separated resonances. Instead, the "e" data were fitted to two displaced Lorentzians with the same back-

Table 7.3: The results of fitting the quench data *j2f1*.lin with two displaced Lorentzians using the program TWOFIT.

b_1	Height (normalised to 1)	-0.318
b_2	Centre of 1st Lorentzian (MHz)	282.59
b_3	FWHM (MHz)	105.34
b_4	Background (normalised to 1)	1.026
b_5	Centre of 2nd Lorentzian (MHz)	347.44
	χ^2	1.175
	Displacement of Lorentzians (MHz)	64.85
	Centre of resonance (MHz)	315.02

ground, FWHM and height. These quantities, plus the position of each Lorentzian, were floated in the fit. This approach yielded a FWHM for each Lorentzian of approximately 100 MHz. In contrast, fitting a single Lorentzian to one of the other data sets (which apparently showed a single resonance) had given a width closer to 150 MHz. This was evidence that the "f", "g" and "h" data also contained two displaced resonances. For this reason, all the quench data were ultimately fitted to two Lorentzians using the program TWOFIT. Figs. 7.4 and 7.5 show the results of this fitting. In each case, the upper curve is the fitted 2S–4P resonance, which has been normalised to 1 by dividing by the background metastable flux. The points and error bars shown in the plot have been derived from the normalised "shutter out" data, by taking the mean and standard deviation of each group of 10 points. The solid line is the fitted lineshape, made up of the two Lorentzians shown as dotted lines. The reference fringes (fitted using FRINGEFIT) are also shown.

The data were also fitted to two displaced Gaussians in a similar manner, but this method gave slightly poorer statistics. Table 7.3 contains the best fit values of the floated parameters b_i and χ^2 for the case of the "f" data. For comparison, Table 7.4 gives the equivalent results obtained by fitting the same data to a single Lorentzian using the program LORFIT. Note the difference in the FWHM and height.

The uncertainties on the b_i were derived from the diagonal elements of the covariance matrix $\mathbf{C}$ returned by TWOFIT, ie.

$$\sigma^2(b_j) = C_{jj}. \tag{7.4}$$

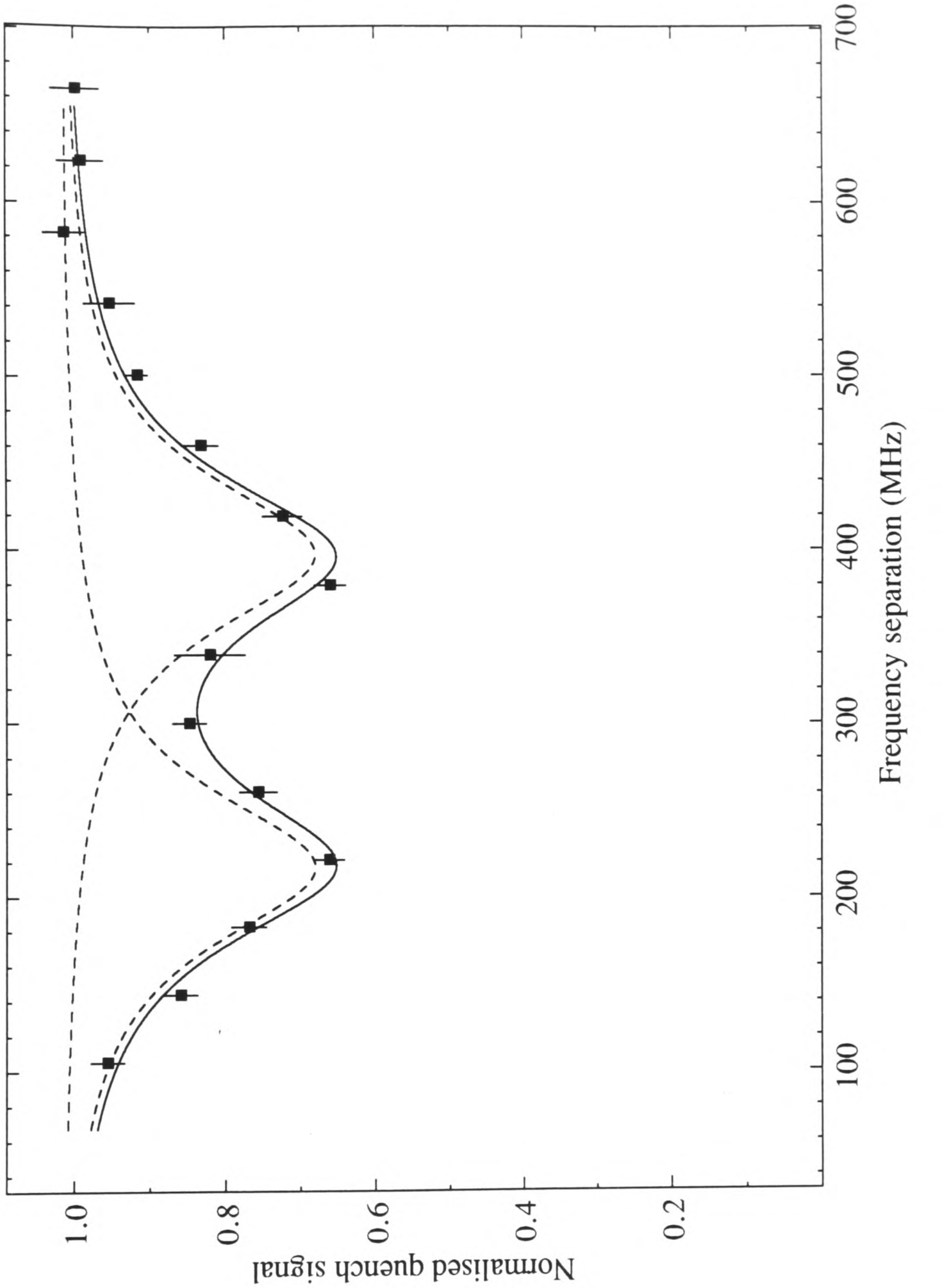


Figure 7.4: The "e" quench data, fitted using TWOFIT. The dotted lines are the two Lorentzians which make up the fitted lineshape (solid line).

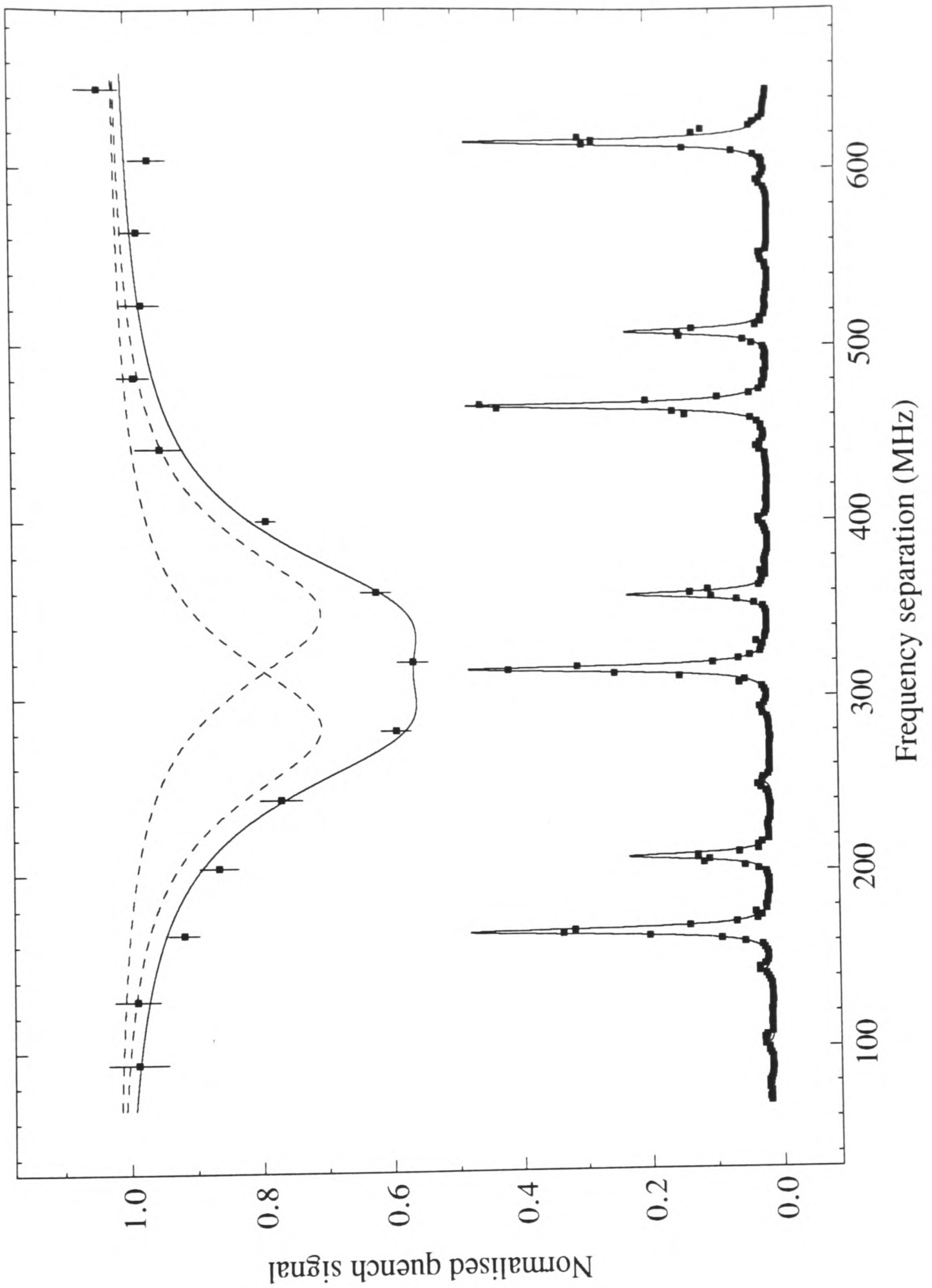


Figure 7.5: The "f" quench data, fitted using TWOFIT. The dotted lines are the two Lorentzians which make up the fitted lineshape (solid line). The reference fringes have been fitted using FRINGEFIT.

Table 7.4: The results of fitting the quench data *j2f1*.lin with a single Lorentzian.

b_1	Height (normalised to 1)	-0.523
b_2	Centre of resonance (MHz)	314.67
b_3	FWHM (MHz)	158.37
b_4	Background (normalised to 1)	1.051
	χ^2	1.212

Specifically, the uncertainty in the position of the centre of the 2S–4P resonance (the average of the positions of the two separated Lorentzians) came out to be of order 3 MHz in each case.

It can be seen from Fig. 7.5 that the centre of the 2S–4P resonance is very close to the second TEM_{00} (or "A") fringe. The frequency difference ν(2S–4P) – ν(fringe) between the two is the quantity b required for the calculation of the frequency interval δ. The position of this fringe was at (165.59 + 149.93) MHz = 315.52 MHz for all the data sets (see Table 7.2). Table 7.5 gives the values of b obtained directly from the output of TWOFIT. Note that the values of b obtained in this way show evidence of a systematic drift, which will be dealt with in §7.4. The uncorrected values shown in Table 7.5 are therefore not yet suitable for a calculation of δ. The figures in brackets are the uncertainties in b derived from the covariance matrix as described above.

Table 7.5: The values of b obtained from the output of TWOFIT together with fringe positions as defined for FRINGEFIT–as yet with no correction for cavity drift.

	Centre of 2S–4P (MHz)	b (MHz)
j2f1.lin	315.02	-0.50(3.2)
j2g1.lin	317.09	1.57(3.2)
j2h1.lin	317.80	2.28(3.7)

Table 7.6: The format of the raw data file *july2f1*.sig.

Start time	19:36:18
No. of points	70
Scan range (MHz)	7
Frequency bin width (MHz)	0.1
Integration time (s)	1
MinUV	-895

AOM frequency (MHz)	Counts per bin	UV power
260.8	165	56
260.9	119	65
etc.		

7.3 1S–2S and reference fringe

The analysis in this case is somewhat simpler than that described in the previous section because of the fact that the 1S–2S signal and its associated reference fringe were both scanned using the AOM (§5.8) and were therefore already on a linear frequency scale. It was merely necessary to multiply all frequencies here by 2 to take account of the double pass of the laser beam through the AOM. We note that the frequencies which appeared in the raw data files (".sig" for the 1S–2S signal and ".ref" for the reference fringe) were those fed to the AOM from the Marconi, ie. *half* the true frequency shift of the beam. Note that the direction of the AOM scan was *upwards* in frequency from the 25 cm cavity mode ie. in the direction shown in Fig. 6.6. The format of the ".sig" and ".ref"' data files are illustrated in Tables 7.6 and 7.7.

The 1S–2S signal and reference fringe were fitted in essentially the same way, using a program which allowed fitting of a Lorentzian to a chosen range of the data. The parameters which were floated were the height, FWHM, position of centre and background. The readings from the UV photodiode were unfortunately faulty in the ".sig" files, so normalisation of the signals was not possible. However, this was

Table 7.7: The format of the raw data file *july2f1*.ref.

Start time	19:39:32
No. of points	200
Scan range (MHz)	10
Frequency bin width (MHz)	0.05
MinRef	-901
MinNorm	-995

AOM frequency (MHz)	Ref. cavity transmission	Normalisation power
208.00	-862	-899
208.05	-865	-900
etc.		

Table 7.8: The results of fitting the 1S–2S data in *july2f1*.sig with a Lorentzian using the program SIGFIT. The position and FWHM are in terms of AOM frequency (half true frequency). The bin time was 1 second in this instance.

1	Height (counts per bin)	290.91
2	Position of centre (MHz)	264.17
3	FWHM (MHz)	2.56
4	Background (counts per bin)	47.42

not in practice a significant source of error, since the signal had a width of about 5 MHz in the blue, compared to the 100 MHz width of the 2S–4P resonance. In any case, the UV power level had been constant on the timescale of a second during the experimental runs.

The uncertainties in the individual data points were determined in a similar manner to that described in §7.2.2. The deviations turned out to be approximately 20 on each point. The diagonal elements of the covariance matrix gave the uncertainties on the best fit values of the floated parameters as before. Specifically, the uncertainty on the position of the centre of the resonance came out to be 0.03 MHz. However, in this case the statistical uncertainty was certainly an underestimate, since it was found that changing the range of points over which the data were fitted could alter the value of this parameter by up to 0.1 MHz. For this reason, the uncertainty on the position of the 1S–2S is quoted here as 0.2 MHz (in terms of true frequency). This is still very small compared to the error on b from the quench data.

A typical 1S–2S signal, fitted as described above using the program SIGFIT, is shown in Fig. 7.6. The best fit parameters are given in Table 7.8 in which all frequencies are "AOM frequencies" ie. half the true frequencies. The FWHM of the 1S–2S resonance is $2 \times 2.56 = 5.12$ MHz at the laser frequency in the blue. To get the width at the atomic frequency, this must be multiplied by two factors of 2, once to account for the frequency doubling to 243 nm and once because of the two-photon process. The width at the atomic frequency is therefore 20.48 MHz.

The fitting of the ".ref" data proceeded in much the same way. Unfortunately, however, imperfect mode matching of the 486 nm laser beam into the 1 m cavity had resulted in smaller peaks on either side of the TEM_{00} mode. For this reason, only about 50 points over the peak were fitted. The program used to fit the reference fringe data was called REFRINGE. An example of a fitted reference fringe is shown in Fig. 7.7. The uncertainty in the fringe position introduced by the presence of the higher order modes was not taken into account. It is clear from Fig. 7.7 that this

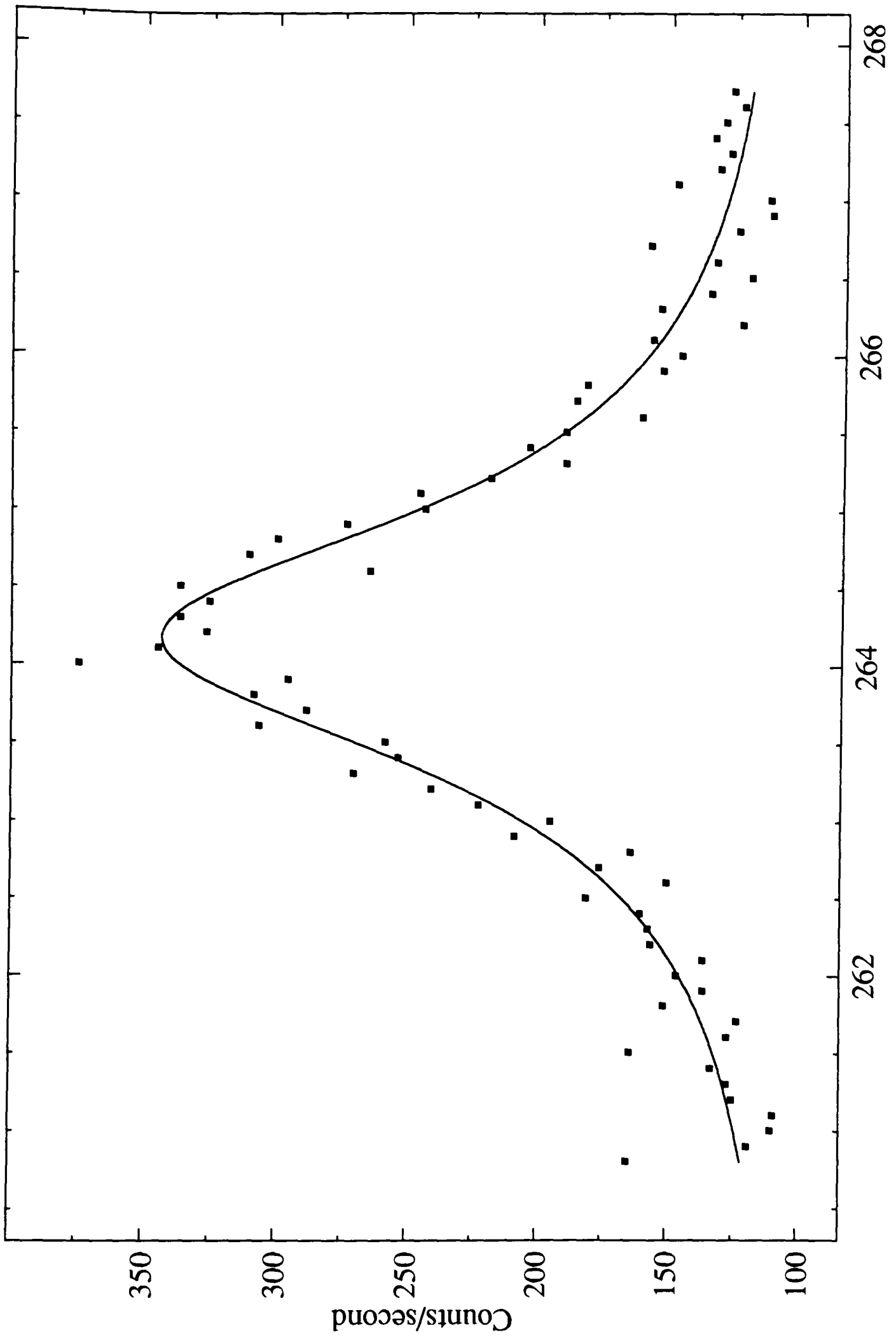


Figure 7.6: The 1S–2S signal data *july2f1*.sig, fitted using SIGFIT as described in the text.

Table 7.9: Results of fitting the 1S–2S and reference fringe data. AOM frequency is half the true frequency. The results have not been corrected for cavity drift.

	AOM frequency (MHz)			True frequency (MHz)
Data file	Fringe position	1S–2S position	$a/2$	a
f	213.16	264.17	51.01	102.02 (0.2)
g	212.68	264.42	51.74	103.48 (0.2)
h	212.26	264.26	52.00	104.00 (0.2)

would have been a fraction of a MHz, ie. of the same order as the uncertainty in the 1S–2S position and therefore very small compared to the uncertainty in b.

The frequency separation between the centre of the 1S–2S signal and the reference fringe (ν(1S–2S) – ν(fringe)) is the quantity a required for the calculation of δ above. Table 7.9 contains the values of a derived from each of the four data sets. The uncertainty on each a was 0.2 MHz. Again, there is as yet no correction for cavity drift.

7.4 Cavity drift

It was pointed out above that the results presented in Tables 7.5 and 7.9 show evidence of reference cavity drift. This point will now be considered in more detail. The four data sets considered here were taken on the same day within the space of about an hour. The "e" data were first, followed by "f", "g" and "h" in that order. Within each data set, the sequence was ".qch", ".sig", ".ref". All the data files contained a recording of the time at which they had been taken.

The positions of the 1S–2S signal and its associated reference fringe were both measured with respect to the 25 cm cavity mode to which the doubled laser had been locked. Table 7.9 shows that the measured position of 1S–2S hardly changed at all over the period of the experimental run and there is no sign of a systematic drift. This implies that the 25 cm cavity was stable to better than 1 MHz per hour. On the other hand, the position of the reference fringe did change during this time. The implication is that the 1 m reference cavity fringes were drifting down in frequency. This conclusion is borne out by inspection of Table 7.5, which shows that b was drifting upwards with time and therefore the reference fringe to which the 2S–4P signal is being referred was drifting downwards. Given that the 25 cm cavity was stable to the precision we are concerned with, it was possible to use the results for

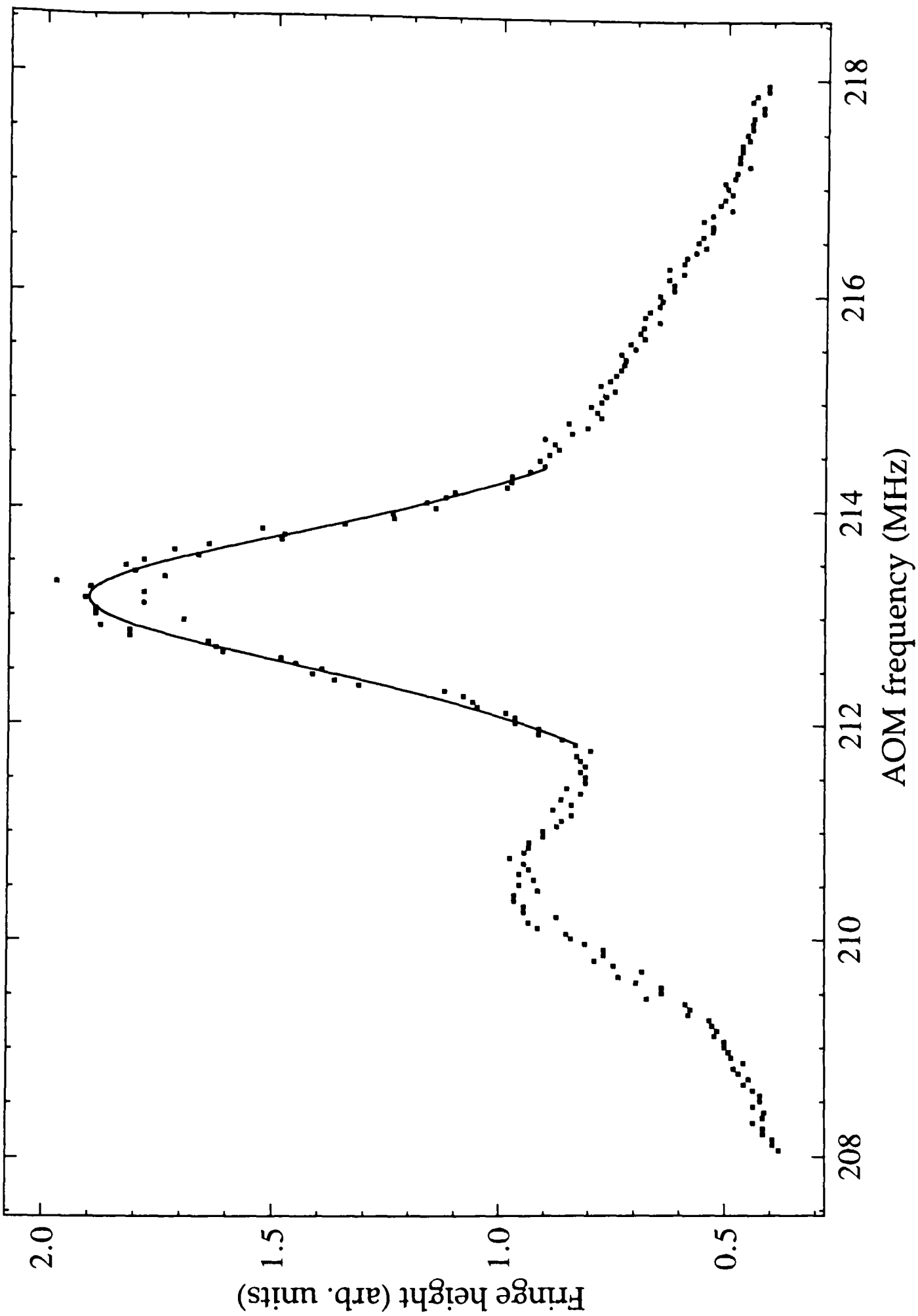


Figure 7.7: The reference fringe data *july2f1*.ref, fitted using the program REFRINGE as described in the text.

Table 7.10: The reference fringe positions measured at time t, the fringe positions corrected to time $t = 0$ and the corresponding corrected value of a. All frequencies are "true" frequencies, not AOM frequencies.

Data set	t (minutes)	Measured fringe position (MHz)	Corrected fringe position (MHz)	Corrected a (MHz)
f	35.72	426.4	430.54	97.9
g	44.10	425.4	430.52	98.5
h	51.30	424.6	430.55	98.1

Table 7.11: The values of b obtained directly from the quench data, the times at which the data were recorded and the values of b corrected to time $t = 0$.

Data	time (minutes)	b (MHz)	Corrected b (MHz)
f	29.15	-0.50	-3.88
g	38.18	1.57	-2.86
h	45.93	2.28	-3.05

the 1S–2S reference fringe to find the drift rate of the 1 m cavity and correct the values of b and a accordingly. To do this, it was assumed that the measured fringe position varied linearly with time. A straight line fit showed that the reference fringes were drifting according to $(430.5 - 0.116t)$ MHz, where t is in minutes and $t = 0$ was the time at which the first scan, namely *july2e1*.qch, was taken. This corresponds to a drift rate of 7 MHz per hour.

Table 7.10 shows the time at which ".ref" data had been taken, along with the measured fringe position and the same fringe position corrected to time $t = 0$. The value of a corrected to $t = 0$ is also given. When the correction was applied to the 2S–4P data, the corrected values of b shown in Table 7.11 were obtained. Again, the results have been corrected to time $t = 0$. Note that b was always negative, implying that the 2S–4P resonance was lower in frequency than the associated reference fringe—not as shown in Fig. 6.6.

Table 7.12: The calculation of δ from the data.

Data	b (MHz)	a (MHz)	δ (MHz)
f	-3.88	97.88	4695.2 (3.2)
g	-2.86	98.36	4695.6 (3.2)
h	-3.05	98.05	4695.9 (3.7)
		Mean δ (MHz)	4695.5 (1.9)

7.5 The frequency interval δ

It now remains to calculate the frequency difference δ from these corrected values for a and b. As stated in the introduction to this chapter, there are an integer number N reference cavity free spectral ranges between the fringes associated with the 1S–2S signal and the 2S–4P transition (see equation 7.1). The wavemeter readings at which the two transitions were found were sufficiently accurate to enable N to be determined unambiguously. The wavemeter readings indicated that $\delta = 4700 \pm 40$ MHz. Inserting this value into equation 7.1 along with $a \approx 100$ MHz and $b \approx -3$ MHz gives the result $N = 32$.

It is now possible to calculate a value for δ from our data. This is summarised in Table 7.12. The first two columns show the corrected a and b from the previous section. The third column is the δ calculated as above. The figure in brackets is the uncertainty (in MHz) in δ derived from the uncertainty in b. The table also gives the weighted mean of the δ's and the associated uncertainty.

7.6 Calculation of the 1S Lamb shift

The final value $\delta = 4695.5(1.9)$ MHz can now be used to obtain an experimental value for the 1S Lamb shift (Δ_{exp}). Given that the theoretical value for δ (δ_{th}) is 4696.9 MHz (Table 2.6) and for the 1S Lamb shift (Δ_{th}) is 8173.0 MHz (Table 2.2), we may write

$$\delta_{th} - \Delta_{th} = 4696.9 - \frac{1}{4} \times 8173.0 = 2653.7 \text{ MHz}. \tag{7.5}$$

We have measured δ to be 4695.5(1.9) MHz. The value of Δ_{exp} derived from our measurements is therefore

$$\begin{aligned}\Delta_{exp} &= 4 \times [\delta - (\delta_{th} - \Delta_{th})] \\ &= 4 \times [4695.5(1.9) - 2653.7] \text{ MHz} \\ &= 8167(8) \text{ MHz.} \end{aligned} \tag{7.6}$$

The error quoted above is purely statistical and would have been considerably smaller had more data been available for analysis.

7.7 Systematic effects

Possible systematic shifts of the 1S–2S and 2S–4P frequencies will now be considered.

7.7.1 Second order Doppler shift

If a source emitting radiation at frequency ν_0 is moving at a velocity v away from an observer, that observer will measure the frequency of the radiation as ν where

$$\nu = \nu_0 \left[\frac{1 - v/c}{1 + v/c}\right]^{-1/2}. \tag{7.7}$$

Expanding this expression to second order in v/c gives

$$\nu - \nu_0 = \nu_0 \left[-\frac{v}{c} + \frac{v^2}{2c^2} + \cdots\right]. \tag{7.8}$$

The first term on the right hand side of the above is the first order Doppler shift which is cancelled by the counter-propagating laser beams in this experiment. The second order Doppler shift $\nu_0 v^2/2c^2$ is not. The laser frequency must be lowered by this amount to bring it into resonance with the moving atom. In this work, the second order Doppler shift of the 1S–2S transition was $\sim$ 70 kHz at the atomic frequency (121.5 nm). This was beyond the precision of the experiment. The second order Doppler shift of the 2S–4P transition was one quarter of this—also negligible.

7.7.2 The Zeeman effect

Shifts arising from stray magnetic fields can be estimated using the standard results for the weak field Zeeman effect (see, for example, [35]). "Weak field" means that any Zeeman shift is much less than the hyperfine splitting. In this case, the shift ΔE_Z of a level $|J\ I\ F\ M_F>$ in a weak magnetic field B is

$$\Delta E_Z = g_F \mu_B B M_F \tag{7.9}$$

where μ_B is the Bohr magneton and g_F is given by

$$g_F \approx g_J \left[\frac{F(F+1) + J(J+1) - I(I+1)}{2F(F+1)}\right] \tag{7.10}$$

and

$$g_J = \frac{3J(J+1) + S(S+1) - L(L+1)}{2J(J+1)}. \tag{7.11}$$

Using these expressions, it is found that the $1S_{1/2}$ and $2S_{1/2}$ levels both have $g_F = 1$ and therefore both suffer a level shift $\Delta E_Z = \mu_B B M_F$. Since the two-photon selection rule for M_F is $\Delta M_F = 0$ (§3.4), there is no shift in the 1S–2S frequency due to static magnetic fields.

The treatment of the $2S_{1/2}$-$4P_{1/2}$ transition is not quite so simple, because the selection rule $\Delta M_F = 0$ does not hold for all the hyperfine components. However, it is possible to estimate the size of the Zeeman shift of the transition. The only magnetic field which should be considered is the earth's field which has a magnitude of approximately 0.4 Gauss. The metastable beam in this experiment was enclosed within the stainless steel vacuum chamber with 1/2" thick walls. The presence of windows in the chamber would have reduced the degree of shielding somewhat. However, the magnetic field inside the chamber would have been substantially reduced (by at least an order of magnitude) compared to the value outside. A worst case Zeeman shift, being of order 1.4 MHz/Gauss (see above), would therefore be about 60 kHz and entirely negligible in this experiment.

7.7.3 The DC Stark effect

An upper limit on the magnitude of any static electric field present in the apparatus may be obtained from the observation that a sizeable fraction of the metastable atoms produced in the interaction region survive to the detection region 40 cm away. The magnitude of the electric field must therefore be less than that required to reduce the $2S_{1/2}$ lifetime to around the time required for an atom in the beam to traverse this distance ie. $\sim 2 \times 10^{-4}$ s (see §5.5). Equation 3.31 gives an upper limit of 0.13 Vcm^{-1} for the field in the beam chamber.

The quadratic Stark shift of the transition frequencies arising from this electric field $\mathcal{E}$ can now be estimated. The $1S_{1/2}$ level is perturbed very weakly by the electric field because of the lack of nearby levels of opposite parity. However the $2S_{1/2}$ level lies only 1058 MHz above the $2P_{1/2}$. The quadratic Stark shift ΔE_{QS} of the $2S_{1/2}$ level may be estimated by considering only the contribution from $2P_{1/2}$. Second order perturbation theory gives

$$\Delta E_{QS} = \sum_{F'} \frac{\left| < 2S_{1/2}, F, M_F | ez\mathcal{E} | 2P_{1/2}, F', M_F > \right|^2}{E(2S_{1/2}, F) - E(2P_{1/2}, F')}, \tag{7.12}$$

where E is the energy of each level. This expression can be expanded to give $\Delta E_{QS} = 4.7\mathcal{E}^2$ kHz/$(\mathrm{Vcm}^{-1})^2$ (using the result $\left| < 2S_{1/2} | z | 2P_{1/2} > \right|^2 = 9a_0^2$ from [25]). With a field of 0.13 Vcm^{-1}, the shift of the $2S_{1/2}$ level is 0.08 kHz—clearly negligible in this experiment.

A rough estimate of the shift of the $4P_{1/2}$ level may be obtained by scaling up the above result. Consider first only the effect of the 4S level. In this case, the energy denominator will be approximately 8 times smaller than that in equation 7.12 and the squared matrix element is approximately 20 times larger [25]. The contribution from 4D will be of a similar magnitude. These two contributions will dominate the calculation. The shift of the $4P_{1/2}$ level will therefore be roughly $1500\mathcal{E}^2$ kHz/(Vcm^{-1})^2, ie. $\sim$ 25 kHz in this experiment. This is also completely negligible in comparison with the precision achieved on the 2S–4P transition.

7.7.4 The AC Stark effect

There is a possibility of a shift of the 1S–2S frequency caused by the 243 nm alternating electric field. Chu has calculated [58] that the total transition frequency shift in a laser beam of wavelength 243 nm and intensity $\mathcal{I}$ is $1.67\mathcal{I}$ Hz/(Wcm^{-2}). In this experiment, the total intensity in the interaction region was approximately 320 Wcm^{-2} ($\sim$ 50 mW in each beam, waist size 100 μm). The AC Stark shift of the 1S–2S transition was therefore approximately 530 Hz. This can clearly be neglected.

The intensity of the 486 nm laser beam in the Balmer-β interaction region was extremely small. The power in the beam was around 200 mW and the spot size was $\pi \times 1.5^2 \approx 7$ cm^2, giving an intensity in the forward going beam of only 0.03 Wcm^{-2}. There is no possibility of any appreciable AC Stark shift on the Balmer-β transition.

7.7.5 The retro-reflected 486 nm beam

Two potentially serious systematic shifts were only recognised during the final stages of the writing of this thesis. They arose from the corner-cube method of avoiding misalignment errors of the Balmer-β laser beam with respect to the metastable beam (§6.5). Firstly, reflection losses at each pass through the entry/exit face of the corner cube meant that the retro-reflected beam was down by about 4% in power compared to the forward-going beam. Of itself, this would mean that the resonance due to the reflected beam would be smaller than the other one. This is however compensated to some extent by the other effect, which arises from the fact that the laser beam had a convergence of 1 in 100 (full angle). The corner cube was 28.5 mm deep and was positioned 5 mm below the metastable beam. The retro-reflected beam therefore travelled an extra $2 \times (5 + 28.5) = 67$ mm to reach the metastable beam and in that distance, the radius of the laser spot decreased by approximately 2%. This would have the effect of increasing the intensity in the illuminated region of the metastable beam if it were not for the reflection loss mentioned above.

Now, the number of transitions per second is proportional to the linear dimensions of the illuminated region (see Fig. 6.2) and to the light power. The depths of the two displaced resonances differ therefore by about 2%. During the analysis, it was assumed that they were the same. Given that the separation was 60 MHz, this could have introduced a sizeable error in the determination of the position of the true centre

of 2S–4P. If it had been possible to repeat the experiment in the light of the data analysis, the alignment of the laser beam could have been improved to decrease the separation and make the effect of these systematics less serious.

It can be shown that a difference of 2% in the heights of the two resonances shifts the position of the centre of gravity by approximately 0.5% of their separation. It is not possible to correct the value of δ by this amount. To do so would require knowledge of which of the resonances had been produced by the backward-going beam, something which depends on the angle between the laser beam and the metastable beam. Therefore, a systematic error of 2 MHz (obtained by multiplying the above systematic error in δ by 4) is added to the statistical error of 8 MHz on the 1S Lamb shift, giving the final result of 8167(10) MHz.

This result for the 1S Lamb shift is an order of magnitude less precise than the previous Oxford measurement of 8172.6(7) MHz. However, this was the first determination of the 1S Lamb shift without the use of an external frequency standard. The implications of the work will be considered further in the next chapter.

Chapter 8

Conclusions

8.1 Summary of this work

This thesis has described the first excitation of the hydrogen 1S–2S transition in an atomic beam [54] and the first continuous wave direct comparison of the frequencies of two hydrogen transitions [55]. The work has resulted in a measurement of the 1S Lamb shift which is essentially independent of frequency standards. The result (8167(10) MHz) is in agreement with theory (8173.0 MHz); although the precision was poorer than the previous best measurement [1] and the measurement of Hänsch [24](carried out following the work described here and based on a comparison of 1S–2S and 2S–4S), the experiment did achieve the objective of demonstrating the feasibility of the method. A useful byproduct of the experiment was the generation of an optically excited metastable hydrogen beam. The advantages and potential uses of such a beam will be discussed below, together with some of the possible future developments in the field.

8.2 The optically excited metastable beam

The main reason for developing the beam excitation of the 1S–2S transition was to do away with the uncertainties associated with collisional processes. In particular, pressure shifts and broadening—factors which had to be accounted for in the earlier "cell mode" work [21] —were negligible. The optically excited metastable beam generated by this process was used for the Balmer-β excitation.

This method of metastable production may be compared to the more common method of electron bombardment. The latter can be performed in two ways—either with an electron beam which is transverse to the atomic beam (for example the experiments of Lamb [6]) or along the atomic beam (as in the more recent work of Shiner [59]. Longitudinal excitation gives a bright, collimated metastable beam, but because the atoms are dissociated by the same hot filament which serves as the thermionic electron source, the average speed of the metastables is high. Transverse

electron bombardment introduces a recoil of the atoms which spreads the beam and reduces the flux for a particular collimation. Optical excitation gives a metastable flux comparable with transverse electron bombardment, but without the recoil. Optical excitation is therefore particularly suitable for producing a metastable beam from cold atoms. It would be relatively simple in our apparatus to cool the hydrogen nozzle with liquid nitrogen. This measure would reduce the mean atomic speed in the metastable beam, thereby improving the beam density and lengthening the transit time. Both of these changes would tend to improve the observed 1S–2S signal. In fact, this depends on the inverse square of the atomic speed, so halving the temperature of the beam would result in a four-fold increase in peak signal as well as giving a narrower resonance.

8.3 Future prospects for the 1S Lamb shift

The precision of the experiment described in this thesis was limited primarily by the small amount of data available. However, if this had not been the case, the 100 MHz width of the 2S–4P resonance would have been the limiting factor. A metastable beam collimation of 500 rather than 100 would be required to match the 13 MHz natural width of 2S–4P. This would be possible if the size of the 1S–2S signal were increased by cooling the beam as described above and by using a differential pumping scheme to lower the background pressure in the beam chamber.

However, a better option would be to move towards a comparison with 2S–4S. As pointed out earlier (§1.5), the natural width of 2S–4S is only 700 kHz and it is amenable to excitation by two-photon Doppler-free spectroscopy at 972 nm. In fact, subsequent to the work described in this thesis, Hänsch and co-workers have employed this technique to obtain a measurement of the 1S Lamb shift with an uncertainty of 110 kHz [24].

Some interesting alternatives to a comparison of 1S–2S and 2S–4S have been proposed by the Paris group [60]. They note that the frequencies of any pair of hydrogen transitions 1S–nS and 2S–2nS are almost in the ratio 4:1. They propose comparing the frequencies of 1S–4S and 2S–8S because the 1S–4S transition has a natural width of 700 kHz and 2S–8S has a width of 144 kHz. This appears to throw away the advantage of the very narrow 1S–2S transition, but this is not the limiting factor in a comparison therefore such an experiment could still produce a competitive measurement of the 1S Lamb shift. Unfortunately, two-photon spectroscopy of 1S–4S requires radiation at 195 nm, which cannot be obtained using currently available frequency doubling materials. For this reason, attention is being turned first to 1S–3S (requiring radiation at 205 nm) and 2S–6S. However, the generation of 205 nm is far from simple, and this work is consequently in very early stages of development.

For the present, therefore, 1S–2S offers the best prospect for measurements of the 1S Lamb shift. The precision is approaching the point at which it will be comparable to that of the $2S_{1/2}$–$2P_{1/2}$ Lamb shift. It has been pointed out that the uncertainty

in the proton charge radius (mentioned in §2.3) puts a limit on the usefulness of 1S Lamb shift measurements as a test of bound state QED. The uncertainty in the theoretical result arising from this factor is 55 kHz (Table 2.3), which is a sizeable (but not the largest) contribution to the theoretical uncertainty. Experimental results are not yet at this level of precision. Similar measurements on other hydrogenic systems which do not suffer from the problem of the proton size (eg. the purely leptonic muonium [61]) are well behind the hydrogen work in precision because of the considerable experimental difficulties associated with them. In any case, Pipkin [62] has pointed out that combining results from hydrogen and deuterium gives much greater potential accuracy, since the ratio of the proton and deuteron charge radii is known much more accurately than each quantity individually.

A number of hydrogenic systems are currently being studied with a view to testing bound state QED. Each of these has something to offer and presents a different experimental challenge. Muonium has already been mentioned. Positronium is also purely leptonic and is especially interesting because of having annihilation terms in the QED calculation [63]. Measurements of Lamb shifts in high-Z hydrogenic ions can test the Z-dependence of the QED corrections [64]. The work on hydrogen can be seen as complementary to the above, its main strengths being the high precision with which measurements can be made and the fact that technology developed for hydrogen can be applied to the other systems (eg. muonium).

Returning to the experiment described in this thesis, it is clear that the precision with which a measurement of the hydrogen 1S Lamb shift can be made is determined by the precision achievable on the comparison Balmer-β transition. Since the pioneering work done in Oxford during the 1980's on the generation of cw 243 nm radiation, and the work described here on the beam excitation of 1S–2S, this part of the experiment has become relatively straightforward. In the present experiment, we achieved a width of 20 MHz (in the atomic frame) on 1S–2S. It would be possible to decrease the linewidth further with the aid of stabilised lasers and a cooled metastable beam. However, the resolution achievable on the 1S–2S transition does not currently limit the ultimate precision. The emphasis has now been shifted from 1S–2S to the comparison transition. The Balmer-β excitation and frequency interval measurement are the areas on which future experiments must concentrate. This thesis has described the first of this new generation of experiments. The way is now open for further developments.

Bibliography

[1] M.G. Boshier, P.E.G. Baird, C.J. Foot, E.A. Hinds, M.D. Plimmer, D.N. Stacey, J.B. Swan, D.A. Tate, D.M. Warrington, and G.K. Woodgate. *Phys. Rev. A*, 40(11):6169, 1989.

[2] D.H. McIntyre, R.G. Beausoleil, C.J. Foot, E.A. Hildum, B. Couillaud, and T.W. Hänsch. *Phys. Rev. A*, 39(9):4591, 1989.

[3] C.E. Wieman and T.W. Hänsch. *Phys. Rev. A*, 22(1):192, 1980.

[4] G.W. Series. *The Spectrum of Atomic Hydrogen—Advances.* World Scientific, 1988.

[5] G.W. Series. The hydrogen atom (an historical account of studies of its spectrum). In G.F. Bassani, M. Inguscio, and T.W. Hänsch, editors, *The Hydrogen Atom*, page 2. Springer-Verlag, 1989.

[6] W.E. Lamb and R.C. Retherford. *Phys. Rev.*, 72:241, 1947.

[7] R.C. Williams. *Phys. Rev.*, 54:558, 1938.

[8] S. Pasternak. *Phys. Rev.*, 54:1113, 1938.

[9] H. Kuhn and G.W. Series. *Proc. Roy. Soc.*, A(202):127, 1950.

[10] P.J. Mohr. *Phys. Rev. Lett.*, 34:1050, 1975.

[11] G.W. Erickson. *J. Phys. Chem. Ref. Data*, 6(3):831, 1977.

[12] S.R. Lundeen and F.M. Pipkin. *Phys. Rev. Lett.*, 46:232, 1981.

[13] V.G. Pal'chikov, Yu.L. Sokolov, and V.P. Yakovlev. *Metrologia*, 21:99, 1985.

[14] B. Cagnac, G. Grynberg, and F. Biraben. *Jour. de Physique*, 34:84, 1973.

[15] E.V. Baklanov and V.P. Chebotaev. *Opt. Commun.*, 12:312, 1974.

[16] S.A. Lee, R. Wallenstein, and T.W. Hänsch. *Phys. Rev. Lett.*, 35(19):1262, 1975.

[17] J.R.M. Barr, J.M. Girkin, J.M. Tolchard, and A.I. Ferguson. *Phys. Rev. Lett.*, 56(6):580, 1986.

[18] E.A. Hildum, U. Boesl, D.H. McIntyre, R.G. Beausoleil, and T.W. Hänsch. *Phys. Rev. Lett.*, 56(6):576, 1986.

[19] R.G. Beausoleil, D.H. McIntyre, C.J. Foot, E.A. Hildum, B. Couillaud, and T.W. Hänsch. *Phys. Rev. A*, 35(11):4878, 1987.

[20] M.G. Boshier, P.E.G. Baird, C.J. Foot, E.A. Hinds, M.D. Plimmer, D.N. Stacey, J.B. Swan, D.A. Tate, D.M. Warrington, and G.K. Woodgate. *Nature*, 330(6147):463, 1987.

[21] M.G. Boshier. D.Phil thesis, University of Oxford, 1988.

[22] P. Zhao, W. Lichten, Z-X. Zhou, H.P. Layer, and J.C. Bergquist. *Phys. Rev. A*, 39(6):2888, 1989.

[23] G.P. Barwood, W.R.C. Rowley, P. Gill, J.L. Flowers, and B.W. Petley. *Phys. Rev. A*, 43(9):4783, 1991.

[24] M. Weitz, F. Schmidt-Kaler, and T.W. Hänsch. *Phys. Rev. Lett.*, 68(8):1120, 1992.

[25] H.A. Bethe and E.E. Salpeter. *Quantum Mechanics of One- and Two-electron Atoms.* Plenum, 1977.

[26] W.R Johnson and G. Soff. *Atomic Data and Nuclear Data Tables*, 33(3):406, 1985.

[27] J. Sapirstein. *Phys. Rev. Lett.*, 47:1723, 1981.

[28] P.J. Mohr. Quantum electrodynamics calculations. In G.W. Series, editor, *The Spectrum of Atomic Hydrogen—Advances*, chapter 2. World Scientific, 1988.

[29] J.C. Garreau, M. Allegrini, L. Julien, and F. Biraben. *Jour. de Physique*, 51(20):2293, 1990.

[30] *Metrologia*, 19:163, 1983

[31] E.R. Cohen and B.N. Taylor. *The 1986 adjustment of the fundamental constants.* Codata, Bulletin 63, 1986.

[32] R.S. Van Dyck, Jr., F.L. Moore, D.L. Farnham, and P.B. Schwinberg. *Bull. Am. Phys. Soc.*, 31:224, 1986.

[33] P. Sick, 1987. Private communication.

[34] G.G. Simon, Ch. Schmitt, F. Borkowski, and V.H. Walther. *Nucl. Phys. A*, 333:381, 1980.

[35] A. Corney. *Atomic and Laser Spectroscopy.* Oxford University Press, 1977.

[36] G. Grynberg and B. Cagnac. *Rep. Prog. Phys.*, 40:791, 1977.

[37] F. Biraben, M. Bassani, and B. Cagnac. *Jour. de Physique*, 40(5):445, 1979.

[38] F. Bassani, J.J. Forney, and A. Quattropani. *Phys. Rev. Lett.*, 39:1070, 1977.

[39] N.F. Ramsey. *Molecular Beams.* Oxford, 1956.

[40] F. Biraben, J.C. Garreau, L. Julien, and M. Allegrini. *Rev. Sci. Instrum.*, 61(5):1468, 1990.

[41] W.E. Lamb and R.C. Retherford. *Phys. Rev.*, 79:549, 1950.

[42] B.H. Bransden and C.J. Joachain. *Physics of Atoms and Molecules.* Longman, 1983.

[43] A. Yariv. *Quantum Electronics.* Wiley, 1968.

[44] H. Kogelnik and T. Li. *Applied Optics*, 5(10):1550, 1966.

[45] J. Slevin and W. Stirling. *Rev. Sci. Instrum.*, 52(11):1780, 1981.

[46] W.W. MacAlpine and R.O. Schildknecht. *Proc. IRE.*, 47:2099, 1959.

[47] H.C. Berg and D. Kleppner. *Rev. Sci. Instrum.*, 33:248, 1962.

[48] K.C. Harvey and C. Fehrenbach, Jr. *Rev. Sci. Instrum.*, 54(9):1117, 1983.

[49] J.T.M. Walraven and I.F. Silvera. *Rev. Sci. Instrum.*, 53(8):1167, 1982.

[50] G.H. Woodman. D.Phil thesis, University of Oxford, 1992.

[51] F.W. Kowalski, R.E. Teets, W. Demtröder, and A.L. Schawlow. *J. Opt. Soc. Am.*, 68:1611, 1978.

[52] P.E. Ciddor and R.M. Duffy. *J. Phys E.*, 16:1223, 1983.

[53] T.W. Hänsch and B. Couillaud. *Opt. Commun.*, 35(3):441, 1980.

[54] C.J. Foot, P. Hannaford, D.N. Stacey, C.D. Thompson, G.H. Woodman, P.E.G. Baird, J.B. Swan, and G.K. Woodgate. *J. Phys B.*, 23:L203, 1990.

[55] C.D. Thompson, G.H. Woodman, C.J. Foot, P. Hannaford, D.N. Stacey, and G.K. Woodgate. *J. Phys B.*, 25:L1, 1992.

[56] I.I. Sobel'man. *Introduction to the Theory of Atomic Spectra.* Pergamon Press, 1972.

[57] W.H. Press, B.P. Flannery, S.A. Teukolsky, and W.T. Vetterling. *Numerical Recipes.* Cambridge University Press, 1986.

[58] R.G. Beausoleil and T.W. Hänsch. *Phys. Rev. A*, 33:1661, 1986.

[59] D.C. Shiner. PhD thesis, University of Michigan, 1988.

[60] L. Julien and F. Biraben. Recent measurement of the Rydberg constant: results and prospects. In J.C. Zorn and R.R. Lewis, editors, *Atomic Physics 12*, page 381. American Institute of Physics, 1991.

[61] K. Jungmann, P.E.G. Baird, J.R.M. Barr, C. Bressler, P.F. Curley, R. Dixson, G.H. Eaton, A.I. Ferguson, H. Geerds, V.W. Hughes, J. Kenntner, S.N. Lea, F. Maas, M.A. Persaud, G. zu Putlitz, P.G.H. Sandars, W. Schwarz, W.T. Toner, M. Towrie, G. Woodman, L. Zhang, and Z. Zhang. *Z. fur Physik*, 21:241, 1991.

[62] F.M. Pipkin. Separated oscillatory field measurement of the Lamb shift in H, $n = 2$. In G.F. Bassani, M. Inguscio, and T.W. Hänsch, editors, *The Hydrogen Atom*, page 30. Springer-Verlag, 1989.

[63] J.S. Nico, D.W. Gidley, A. Rich, and P.W. Zitzewitz. The decay rate of orthopositronium. In J.C. Zorn and R.R. Lewis, editors, *Atomic Physics 12*, page 481. American Institute of Physics, 1991.

[64] J.D. Silver. The spectroscopy of hydrogen-like highly ionised atoms. In G.F. Bassani, M. Inguscio, and T.W. Hänsch, editors, *The Hydrogen Atom*, page 221. Springer-Verlag, 1989.

"We were only in anxiety and distress during the last two hours; and, previously, there had been a great deal of enjoyment."

Jane Austen